

Optimization of the
Magnet System of the Breit-Rabi Polarimeter
and Calibration of the
Target Gas Analyzer
of the HERMES Experiment at DESY

Diplomarbeit

von

Ines Brunn

angefertigt

an der Friedrich-Alexander-Universität

Erlangen-Nürnberg

Erlangen, 02. April 2001

Think of the target
as a washing machine.

Dr. M.-A. Funk

Zusammenfassung

Das HERMES-(*HERa MEasurement of Spin*)-Experiment am DESY (*Deutsches Elektronen-SYNchrotron*) untersucht die Spinstruktur der Nukleonen. Es ist ein tiefinelastisches Streuexperiment, bei dem polarisierte Leptonen an polarisierten Nukleonen gestreut werden. Longitudinal polarisierte Leptonen des HERA-(*Hadron-Elektron Ring-Anlage*)-Speicherringes werden in der Targetregion an polarisierten Wasserstoff- oder Deuteriumkernen gestreut.

Das Target des HERMES Experiments ist ein internes Speicherzellengastarget. Das dissoziierte und polarisierte Targetgas wird in eine Speicherzelle injiziert, welche der HERA Leptonenstrahl passiert. Durch die verlängerte Aufenthaltsdauer der Nukleonen im Wechselwirkungsbereich erhöht sich die Targetdichte. Dies führt jedoch zu Rekombinationsprozessen in der Speicherzelle. Mit dieser Speicherzellentechnik wird eine hohe Targetpolarisation für Wasserstoff und Deuterium erreicht.

Die Speicherzelle ist mit einem Probenrohr versehen, durch das ein Teil des Targetgases aus der Zelle entweichen und in den Analysierbereich gelangen kann. Der Analysierbereich besteht aus einem Breit-Rabi-Polarimeter und dem Targetgas-Analysator. Das Breit-Rabi-Polarimeter misst die relativen Besetzungszahlen der Hyperfeinstrukturzustände, woraus die Polarisation der Atome berechnet wird. Der Targetgas-Analysator dagegen misst die atomaren und molekularen Flüsse, woraus der Grad der Dissoziation bestimmt werden kann.

Ein Thema dieser Arbeit ist die Kalibration des Targetgas-Analysators bezüglich seiner unterschiedlichen Sensitivität beim Nachweis von Atomen im Vergleich zu Molekülen. Die gemittelte Kalibrationskonstante κ_{tot} wird für den Zeitraum gefunden, in dem HERMES mit polarisiertem Deuterium gelaufen ist. Außerdem wird das Magnetsystem des Breit-Rabi-Polarimeters mit Hilfe einer Monte-Carlo Simulation optimiert. Flugzeitmessungen mit dem alten und dem neuen Sechspol-Magnetsystem des Breit-Rabi-Polarimeters werden durchgeführt und die Resultate mit den Vorhersagen aus der Monte-Carlo Simulation verglichen.

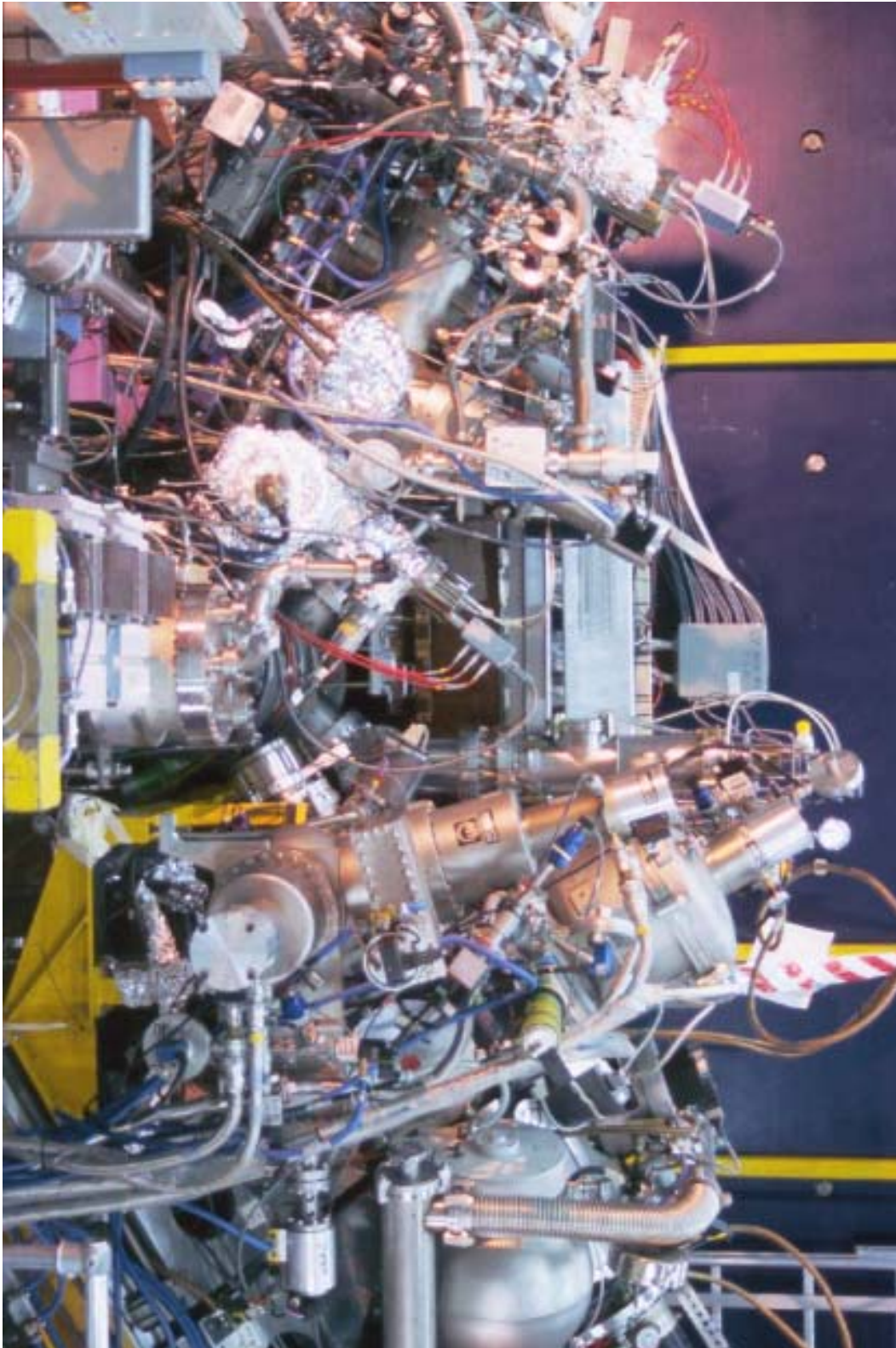


Figure 1:
Vertical picture of the HERMES target system viewed from the upstream direction of the HERA beamline. On the right side the atomic beam source vacuum system can be seen, on the left side the Breit-Rabi polarimeter vacuum system with the target gas analyzer.

Contents

| | | |
|----------|------------------------------------------------------|-----------|
| 1 | Introduction | 3 |
| 2 | Spin Separation and RF Transitions | 7 |
| 2.1 | Hyperfine Splitting in a Magnetic Field | 7 |
| 2.1.1 | The Hyperfine Structure of Hydrogen | 9 |
| 2.1.2 | The Hyperfine Structure of Deuterium | 11 |
| 2.2 | Stern-Gerlach Spin Separation | 12 |
| 2.3 | Adiabatic Radio Frequency Transitions | 14 |
| 3 | Experimental Setup of the Target | 17 |
| 3.1 | The Atomic Beam Source | 18 |
| 3.2 | The Storage Cell | 20 |
| 3.3 | The Target Gas Analyzer | 23 |
| 3.4 | The Breit-Rabi Polarimeter | 24 |
| 4 | Calibration of the TGA | 29 |
| 4.1 | Method | 29 |
| 4.2 | Temperature Scans | 31 |
| 4.2.1 | The Temperature Correction | 33 |
| 4.2.2 | Analyzing a Temperature Scan | 34 |
| 4.3 | HERA Beam Dumps | 36 |
| 4.4 | The Year 2000 | 38 |
| 4.5 | Results | 40 |
| 5 | Optimization of the BRP Magnet System | 43 |
| 5.1 | Permanent Sextupole Magnets | 43 |
| 5.1.1 | General Description | 43 |
| 5.1.2 | Atomic States in Sextupole Magnets | 44 |
| 5.1.3 | Short Sextupole Magnets and Optical Lenses | 45 |
| 5.2 | Monte Carlo Simulation | 47 |
| 5.2.1 | Description | 47 |
| 5.2.2 | Result for the Former Magnet System | 50 |

| | | |
|----------|--------------------------------------------------------|-----------|
| 5.2.3 | Simulations of Various Magnet Systems | 52 |
| 5.2.4 | Simulations with the New Magnet System | 54 |
| 5.3 | Time of Flight Measurements | 57 |
| 5.3.1 | Description | 57 |
| 5.3.2 | Results for the Former Magnet System | 57 |
| 5.3.3 | Results for the New Magnet System | 61 |
| 5.4 | Conclusion | 64 |
| 6 | Discussion and Outlook | 65 |
| A | Compilation of κ Calibrations | 67 |
| A.1 | Temperature Scans | 68 |
| A.2 | Beam Dumps | 83 |
| A.3 | Compilation of κ Calibration Results | 87 |
| B | The BRP Magnet System | 89 |
| | List of Figures | 95 |

Chapter 1

Introduction

The understanding of the spin structure of the nucleon remained a challenge since it was demonstrated using deep-inelastic lepton-nucleon scattering by e.g. EMC [E88], SMC [SM94, SM97] and the SLAC [SL93, SL95, SL97] experiments that only a fraction of the nucleon spin can be described as the sum of the the quark spins. Experiments providing data from inclusive scattering, where only the scattered lepton is detected, show that the contribution of the quark spins to the nucleon spin is at most 30%. Further knowledge can be gained by studying semi-inclusive processes where hadrons are detected in coincidence with the scattered lepton. The interpretation of the semi-inclusive data is more precise if the leading hadron is identified.

Nuclear polarized hydrogen and deuterium gas targets have become an important tool in the study of spin dependent processes in high-energy nuclear and particle physics. They offer a unique combination of a large nuclear polarization and high target purity.

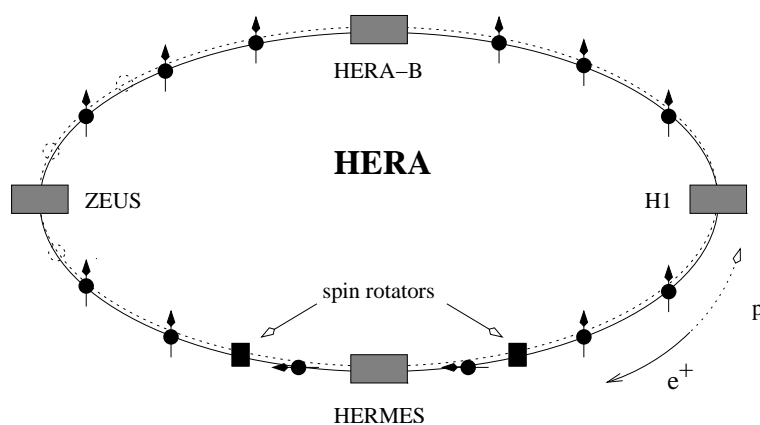


Figure 1.1:
The HERA collider with its four experiments at DESY. The spin rotators provide a longitudinally polarized positron beam for the HERMES experiment only.

An experiment making use of this technique is HERMES. The HERMES (*HERA Measurement of Spin*) experiment [He90, He93] is located in one of the four ex-

perimental areas of the HERA storage ring, a proton-electron collider at DESY in Hamburg (Fig. 1.1). Since 1995 HERA has been accelerating positrons instead of electrons most of the time due to their better beam stability. HERMES makes use of this positron beam by studying spin-dependent deep inelastic scattering off polarized target nucleons. The energy of the positrons of the HERA beam is 27.5 GeV with a maximum beam current of 50 mA. These positrons are transversally polarized due to the Sokolov-Ternov effect [So64] and a longitudinally polarized beam for the HERMES experiment is provided by a pair of spin rotators.

The HERMES detector is an open-geometry forward spectrometer [He98b]. The momentum of a particle can be obtained by a tracking system consisting of drift chambers in front and behind the spectrometer magnet and using a tree-search algorithm. The particle identification is provided by a lead-glass calorimeter, a pre-shower detector, a transition radiation detector and a ring imaging cherenkov (RICH) detector. A special feature of the HERMES experiment is the identification of protons, pions and kaons.

The HERMES target is an internal gas target [He93, He98b, Du95] (Fig. 3.1 in chapter 3). The main features of polarized internal targets for storage rings are their high polarization, no dilution by unpolarized nucleons, rapid polarization reversal and low thickness at high luminosity [He93].

Since 1996 either dissociated hydrogen or dissociated deuterium gas has been polarized by an atomic beam source before being injected into a storage cell which is surrounded by a superconducting magnet (Fig. 3.1 in chapter 3). This magnet provides a longitudinal holding field that defines the quantization axis for the spins, it decouples the electron and nuclear spin, it provides a high polarization of the mixed hyperfine states and reduces the depolarization effects by the HERA bunch field [Kol98]. The storage cell confines the gas atoms to the region of the circulating positron beam and therefore increases the target nucleon density by about two orders of magnitude compared to a free gas jet target. This results in an increase of the probability of a positron-nucleon interaction.

An advantage of an internal gas target (especially compared to solid state targets) is the purity of the target, since there is no dilution by other atoms. At the target of the HERMES experiment a fraction of the atoms can recombine to molecules during their confinement in the target storage cell. Recombination processes are minimized by coating the cell surface with a substance called Drifilm and also cooling the cell to 65-100 K. Adsorbed water layers formed on the cold cell surface also suppress the effect of spin relaxation during wall collisions, resulting in a high target polarization P^T of up to 0.9 for hydrogen and deuterium gas.

The polarization is defined as:

$$P = \frac{N_+ - N_-}{N_+ + N_-} , \quad (1.1)$$

where N_+ (N_-) is the number of nuclei with spin parallel (antiparallel) to an external magnetic field. The target polarization (P^T) of the HERMES experiment is obtained by measurements of the relative occupation numbers of the different hyperfine states by a Breit-Rabi polarimeter. The HERMES target polarization has contributions from polarized atoms (P_a) and polarized molecules (P_m), since two polarized atoms can recombine to a molecule. These contributions to P^T have to be weighted by the degree of dissociation:

$$\alpha = \frac{N_a}{N_a + 2N_m} , \quad (1.2)$$

which is the number of atoms N_a in the atomic state divided by the total number of available atoms. Separating the fraction of molecules coming from recombination inside the cell ($1 - \alpha_r$) and the fraction of molecules already injected by the atomic beam source ($1 - \alpha_0$) the averaged target polarization P^T is given by:

$$P^T = \alpha_0 [\alpha_r P_a + (1 - \alpha_r) P_m] . \quad (1.3)$$

Defining $\frac{P_m}{P_a} = \beta$, the target polarization can be written as:

$$P^T = \alpha_0 [\alpha_r + (1 - \alpha_r)\beta] P_a . \quad (1.4)$$

The quantities α_0 , α_r and P_a are calculated using the measurements of a target gas analyzer and a Breit-Rabi polarimeter. A fraction of the target gas can leave the target storage cell through a small tube called sample tube and can enter either the target gas analyzer, which measures the nucleon flow rates of atoms and molecules or the Breit-Rabi polarimeter measuring the relative occupation numbers of the different hyperfine states of the atoms. The fraction of atoms in the gas sample surviving recombination which is measured by the target gas analyzer is named α_r^{TGA} . The polarization of the gas sample measured with the Breit-Rabi polarimeter is named P^{BRP} . The values α_r^{TGA} and P^{BRP} of the sampled gas are not exactly the same as the α_r and P_a in the storage cell, since the sampled gas atoms have on average undergone more wall collisions than atoms in the cell. So α_r^{TGA} and P^{BRP} are related to the properties of the gas inside the storage cell by the sampling corrections [Hen98, Ba00] c_α :

$$\alpha_r = c_\alpha \alpha_r^{TGA} , \quad (1.5)$$

and c_p :

$$P_a = c_p P^{BRP} . \quad (1.6)$$

For the measurement of the degree of dissociation $\alpha^{TGA} = \alpha_r^{TGA} \cdot \alpha_0^{TGA}$ the target gas analyzer has to be calibrated. This is done by determining the relative sensitivity

of the target gas analyzer to detect atoms or molecules and then separating α_r^{TGA} from α_0^{TGA} . The detection sensitivity κ for the HERMES deuterium running period (1998-2000) is determined in chapter 4 of this thesis.

Since only a small fraction of the target gas is continuously sampled ($\approx 5\%$) via the sample tube, this sample beam has to be detected efficiently. Particles from this beam have to pass radio frequency transition units and a magnet system before being detected in the Breit-Rabi polarimeter. In chapter 5 it will become obvious that the magnet system had to be redesigned for higher transmission.

Chapter 2 deals with the theory of hyperfine splitting for hydrogen and deuterium atoms, Stern-Gerlach spin separation and hyperfine transitions, chapter 3 presents the experimental setup of the HERMES experiment at DESY in Hamburg, Germany.

Chapter 2

Spin Separation and RF Transitions

2.1 Hyperfine Splitting in a Magnetic Field

Several components of the HERMES target make use of the hyperfine splitting of hydrogen and deuterium. The sextupole systems in the atomic beam source and in the Breit-Rabi polarimeter, for example, use the hyperfine state dependent forces inside the magnets for the selection of spin states.

The total angular momentum \vec{F} of an atom is the sum of the nucleus spin \vec{I} , the electron spin \vec{S} and the orbital angular momentum of the electron. In hydrogen and deuterium atoms in the ground state ($1s$) the spin of the nucleus couples directly with the magnetic moment of the electron. The relative energy difference of the states with different total angular momentum $\vec{F} = \vec{I} + \vec{S}$ is called hyperfine structure splitting energy [Ma94]

$$E_{HFS} = \Delta E_{F+1} - \Delta E_F = A \cdot (F + 1) , \quad (2.1)$$

where ΔE_{F+1} and ΔE_F are the energy shifts resulting from the hyperfine interaction, F the quantum number of \vec{F} in respect to the quantization axis and A is an interval factor depending on the specific considered isotop.

The application of an external magnetic field B cancels the degeneration of the states with $F \neq 0$ because of the interaction of the magnetic moment of the electron and the magnetic moment of the nucleus with the external field. Two different regions are distinguishable:

- ① weak external field $B \ll B_c$ (Zeeman region)
- ② strong external field $B \gg B_c$ (Paschen-Back region)

depending on the critical magnetic field B_c

$$B_c = \frac{E_{HFS}}{(g_S - g_I)\mu_B} . \quad (2.2)$$

In this formula μ_B is the Bohr magneton, $g_S = 2.00232$ is the g-factor of the electron and g_I is the g-factor of the nucleus in relation to μ_B (g_I can also be defined in relation to the nuclear magneton μ_K with $\frac{\mu_B}{\mu_K} = 1836.14$). For hydrogen $g_I^H = -0.00304$ and for deuterium $g_I^D = -0.00047$. In case ① the electron and nucleus spin remain coupled and the effect of the external field can be treated as a small perturbation. In case ② the interactions of the external magnetic field with the electron and with the nucleus are much bigger than the hyperfine structure interaction, which now is treated as the perturbation. This results in the decoupling of the electron and the nucleus spin so that they both can precess individually around the external field.

In this chapter the magnetic field is aligned with the z-axis so that $B_z = |\vec{B}| = B$. The ratio of the external field and the critical field is defined as x :

$$x = \frac{B}{B_c} . \quad (2.3)$$

Another property referred to in the following sections is the Larmor frequency of the electron:

$$\omega_S = \frac{(g_S - g_I)\mu_B}{\hbar} B_Z . \quad (2.4)$$

The hyperfine states $|F, m_F\rangle$ are fully described by their quantum number F and the corresponding magnetic quantum number m_F . Considering hydrogen or deuterium atoms in the ground state, the spins of the nucleus and the electron can be either parallel or antiparallel in respect to the quantization axis, so that F can have the two values $I \pm \frac{1}{2}$. For this case ($F = I \pm \frac{1}{2}$) the splitting energy can be calculated with the Breit-Rabi formula [Bre31, Ma94]:

$$E(I \pm \frac{1}{2}, m_F) = -\frac{A}{4} + m_F g_I \mu_K B \pm \frac{1}{2} A (I \pm \frac{1}{2}) \sqrt{1 + m_F \frac{4}{2I+1} \cdot x + x^2} . \quad (2.5)$$

The second term in equation (2.5) describes the interaction of the proton spin with the external field. It is important for the exact calculation of bunch field depolarization resonances at the HERMES experiment. Disregarding this effect and neglecting this term due to the small size of the nuclear magneton μ_K for magnetic fields up to about 30 T and using the rewritten equation (2.1):

$$A = \frac{E_{HFS}}{I + \frac{1}{2}} , \quad (2.6)$$

the hyperfine splitting energies for hydrogen ($I = \frac{1}{2}$) and deuterium ($I = 1$) atoms are:

$$E^H(\frac{1}{2} \pm \frac{1}{2}, m_F) = E_{HFS}^H \cdot \left(-\frac{1}{4} \pm \frac{1}{2} \sqrt{1 + m_F 2x + x^2} \right) \quad (2.7)$$

$$E^D(1 \pm \frac{1}{2}, m_F) = E_{HFS}^D \cdot \left(-\frac{1}{6} \pm \frac{1}{2} \sqrt{1 + m_F \frac{4}{3} x + x^2} \right) . \quad (2.8)$$

2.1.1 The Hyperfine Structure of Hydrogen

Since both proton as well as electron are spin- $\frac{1}{2}$ particles, they can either couple to a total angular momentum $F = 0$ or $F = 1$. Without an external magnetic field the state with $F = 1$ is three times degenerated in respect to the magnetic quantum number m_F which can have values of -1, 0 and 1. All states belonging to the same value of F form a so called Zeeman multiplet.

For the four possible components of the ground state of the hydrogen atom, the energy eigenstates using equation (2.7) and the definition $x = \frac{B}{B_c^H}$ are:

| state | F | m_F | |
|-------|-----|-------|-----------------------------------------------------------------------------------|
| 1⟩ | 1 | 1 | $E_1^H = E_{HFS}^H \cdot \left(\frac{1}{4} + \frac{1}{2}x \right) ,$ |
| 2⟩ | 1 | 0 | $E_2^H = E_{HFS}^H \cdot \left(-\frac{1}{4} + \frac{1}{2}\sqrt{1+x^2} \right) ,$ |
| 3⟩ | 1 | -1 | $E_3^H = E_{HFS}^H \cdot \left(\frac{1}{4} - \frac{1}{2}x \right) ,$ |
| 4⟩ | 0 | 0 | $E_4^H = E_{HFS}^H \cdot \left(-\frac{1}{4} - \frac{1}{2}\sqrt{1+x^2} \right) .$ |

(2.9)

The energy E_i^H belongs to the eigenstate $|i\rangle$, where i starts at the highest energy ($i = 1$) and goes to the lowest ($i = 4$). The progression of these energy eigenvalues in dependency on an external magnetic field is shown in the Breit-Rabi diagram (Fig. 2.1). The energy axis is scaled by the hyperfine splitting energy of hydrogen

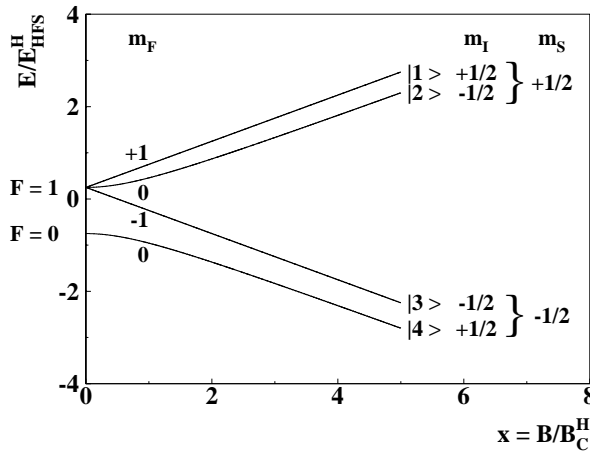


Figure 2.1:

Breit-Rabi diagram [Hae67]. Energy eigenvalues for the hyperfine splitting of a hydrogen atom in an external magnetic field. E_{HFS}^H is the hyperfine splitting energy for hydrogen and x is the ratio between the external and the critical magnetic field of hydrogen B_c^H .

$$E_{HFS}^H = A^H = 5.878 \cdot 10^{-6} \text{ eV} \quad (2.10)$$

and the magnetic field axis is scaled by the critical field for hydrogen

$$B_c^H = 50.7 \text{ mT} . \quad (2.11)$$

The energy difference between the states $|1\rangle$ and $|3\rangle$ in the critical field is equal to that of the hyperfine splitting energy. One of the most exactly measured values in

physics is the frequency that belongs to this transition energy [Dy92]:

$$\nu_{HFS}^H = \frac{A}{2\pi\hbar} = 1\,420\,405\,751.768(1) \text{ Hz.} \quad (2.12)$$

To receive a description independent of the external field the hyperfine states $|F, m_F\rangle$ can be expanded in the product base of the spinwave functions of the proton $|m_I\rangle = |\pm \frac{1}{2}\rangle$ and electron $|m_S\rangle = |\pm \frac{1}{2}\rangle$

$$|m_S, m_I\rangle = |\pm \frac{1}{2}, \pm \frac{1}{2}\rangle, \quad (2.13)$$

where m_S and m_I represent the magnetic quantum numbers of electron and nucleon spin, respectively. For greater clarity, the spin of the electron will be represented as an arrow while the nucleon spin will be represented by its value. In this base the four eigenstates [Co99] have the form:

$$\begin{aligned} |i\rangle &= |F, m_F\rangle = |m_S, m_I\rangle, \\ |1\rangle &= |1, +1\rangle = |\uparrow, +\frac{1}{2}\rangle, \\ |2\rangle &= |1, 0\rangle = \cos\theta \cdot |\uparrow, -\frac{1}{2}\rangle + \sin\theta \cdot |\downarrow, +\frac{1}{2}\rangle, \\ |3\rangle &= |1, -1\rangle = |\downarrow, -\frac{1}{2}\rangle, \\ |4\rangle &= |0, 0\rangle = \cos\theta \cdot |\downarrow, +\frac{1}{2}\rangle - \sin\theta \cdot |\uparrow, -\frac{1}{2}\rangle, \end{aligned} \quad (2.14)$$

with the mixing angle θ , as defined by the following equation:

$$\tan 2\theta = \frac{E_{HFS}^H}{\hbar\omega_S} = \frac{B_c}{B} = \frac{1}{x}. \quad (2.15)$$

Through trigonometric transformations of equation (2.15) the following relationship may be derived:

$$\cos 2\theta = \frac{x}{\sqrt{1+x^2}}. \quad (2.16)$$

The states $|1\rangle$ and $|3\rangle$ are independent of the external magnetic field and are called *pure states*. The states $|2\rangle$ and $|4\rangle$ are mixtures of the states $|\uparrow, -\frac{1}{2}\rangle$ and $|\downarrow, +\frac{1}{2}\rangle$. In the region of a weak external field (Zeeman region) - $x \ll 1$ - the interaction of the electron with the field can be treated as a perturbation. In this case the equations (2.14) simplify to:

$$\begin{aligned} |1\rangle &= |\uparrow, +\frac{1}{2}\rangle, \\ |2\rangle &= \frac{1}{\sqrt{2}} \cdot (|\uparrow, -\frac{1}{2}\rangle + |\downarrow, +\frac{1}{2}\rangle), \\ |3\rangle &= |\downarrow, -\frac{1}{2}\rangle, \\ |4\rangle &= \frac{1}{\sqrt{2}} \cdot (|\downarrow, +\frac{1}{2}\rangle - |\uparrow, -\frac{1}{2}\rangle). \end{aligned} \quad (2.17)$$

2.1.2 The Hyperfine Structure of Deuterium

The nuclear spin of the deuteron is $I = 1$. It can either couple with the spin of the electron to a total angular momentum of $F = \frac{3}{2}$ or $F = \frac{1}{2}$. Without an external magnetic field the state $F = \frac{3}{2}$ is fourfold degenerated in respect to the magnetic quantum number m_F while the state $F = \frac{1}{2}$ is only twofold degenerated, resulting in a total of six possible hyperfine states for the deuterium atom.

In numbering the states according to their energy, as it was done with the hydrogen atom, the energy eigenvalues of the six individual states using equation (2.8) are:

| state | F | m_F | |
|-------------|---------------|----------------|----------------------------------------------------------------------------------------------------|
| $ 1\rangle$ | $\frac{3}{2}$ | $\frac{3}{2}$ | $E_1^D = E_{HFS}^D \cdot \left(\frac{1}{3} + \frac{1}{2}x \right) ,$ |
| $ 2\rangle$ | $\frac{3}{2}$ | $\frac{1}{2}$ | $E_2^D = E_{HFS}^D \cdot \left(-\frac{1}{6} + \frac{1}{2}\sqrt{1 + \frac{2}{3}x + x^2} \right) ,$ |
| $ 3\rangle$ | $\frac{3}{2}$ | $-\frac{1}{2}$ | $E_3^D = E_{HFS}^D \cdot \left(-\frac{1}{6} + \frac{1}{2}\sqrt{1 - \frac{2}{3}x + x^2} \right) ,$ |
| $ 4\rangle$ | $\frac{3}{2}$ | $-\frac{3}{2}$ | $E_4^D = E_{HFS}^D \cdot \left(\frac{1}{3} - \frac{1}{2}x \right) ,$ |
| $ 5\rangle$ | $\frac{1}{2}$ | $-\frac{1}{2}$ | $E_5^D = E_{HFS}^D \cdot \left(-\frac{1}{6} - \frac{1}{2}\sqrt{1 - \frac{2}{3}x + x^2} \right) ,$ |
| $ 6\rangle$ | $\frac{1}{2}$ | $\frac{1}{2}$ | $E_6^D = E_{HFS}^D \cdot \left(-\frac{1}{6} - \frac{1}{2}\sqrt{1 + \frac{2}{3}x + x^2} \right) ,$ |

(2.18)

where $x = \frac{B}{B_c^D}$.

These energy eigenvalues are shown in a Breit-Rabi diagram (Fig. 2.2). Analogous

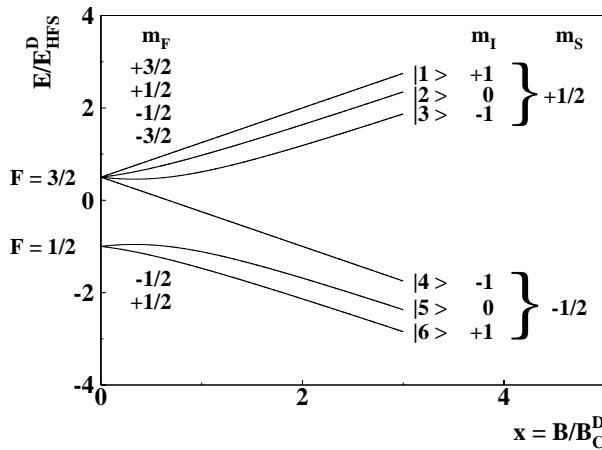


Figure 2.2:

Breit-Rabi diagram [Hae67]. Energy eigenvalues for the hyperfine splitting of a deuterium atom in an external magnetic field. E_{HFS}^D is the hyperfine splitting energy for deuterium and x is the ratio between the external and the critical magnetic field of deuterium B_c^D .

to hydrogen, the energy axis is scaled by the hyperfine splitting energy of deuterium

$$E_{HFS}^D = 1.5 \cdot A^D = 1.354 \cdot 10^{-6} \text{ eV} \quad (2.19)$$

and the magnetic field axis by the critical field of deuterium

$$B_c^D = 11.7 \text{ mT} . \quad (2.20)$$

Here the energy difference between the states $|1\rangle$ and $|4\rangle$ in the critical field is equal to that of the hyperfine splitting energy. The hyperfine transition frequency is 317.28 MHz.

As for hydrogen the states $|F, m_F\rangle$ can be expanded in the product base (2.13) of the spinwave functions of the deuteron and electron $|m_S, m_I\rangle$ resulting in [Co99]:

$$\begin{aligned}
|1\rangle &= |\uparrow, +1\rangle, \\
|2\rangle &= \cos\theta_+ \cdot |\uparrow, 0\rangle + \sin\theta_+ \cdot |\downarrow, +1\rangle, \\
|3\rangle &= \cos\theta_- \cdot |\uparrow, -1\rangle + \sin\theta_- \cdot |\downarrow, 0\rangle, \\
|4\rangle &= |\downarrow, -1\rangle, \\
|5\rangle &= \cos\theta_- \cdot |\downarrow, 0\rangle - \sin\theta_- \cdot |\uparrow, -1\rangle, \\
|6\rangle &= \cos\theta_+ \cdot |\downarrow, +1\rangle - \sin\theta_+ \cdot |\uparrow, 0\rangle.
\end{aligned} \tag{2.21}$$

with the two mixing angles θ_{\pm} defined by:

$$\tan 2\theta_{\pm} = \frac{\sqrt{8}}{3x \pm 1}. \tag{2.22}$$

2.2 Stern-Gerlach Spin Separation

The experiment of Stern-Gerlach [SG21] showed that a beam of silver atoms is separated into two parts by an inhomogeneous magnetic field.

For all atoms where the angular orbital momentum of the electron is zero (spin quantum number $S = \frac{1}{2}$) an inhomogenic magnetic field separates those atoms with the electron spin parallel ($m_S = +\frac{1}{2}$) to the external field from those with the electron spin antiparallel ($m_S = -\frac{1}{2}$), because the magnetic field interacts predominantly with the magnetic dipole moment of the electron μ_S [Hae67]. This results in a force along the gradient of the magnetic field, splitting the atomic beam into two parts.

The field strength of a sextupole magnet (chapter 5) is a function of the radius

$$B(r) = B_{pt} \cdot \left(\frac{r}{r_{pt}}\right)^2, \tag{2.23}$$

where B_{pt} is the pole tip field and r_{pt} is the radius of the pole tip. This inhomogenic magnetic field separates e.g. a beam of hydrogen or deuterium atoms. A hydrogen or deuterium atom is subject to a force in radial direction (unit vector $\vec{e}_r = \frac{\vec{r}}{|\vec{r}|}$):

$$\vec{F} = -\vec{\nabla} E = -\frac{\partial E}{\partial r} \cdot \vec{e}_r = -\frac{\partial E}{\partial B} \cdot \frac{\partial B}{\partial r} \cdot \vec{e}_r = -\frac{\partial E}{\partial B} \cdot 2 \frac{B_{pt}}{r_{pt}^2} \cdot r \vec{e}_r, \tag{2.24}$$

where E is the energy eigenvalue of the hyperfine state. The effective magnetic moment μ_{eff} is defined as:

$$\mu_{eff} = \frac{\partial E}{\partial B} , \quad (2.25)$$

which is the slope of the curves in the Breit-Rabi diagram 2.1 for hydrogen and 2.2 for deuterium. The Breit-Rabi diagrams show that the hyperfine states with $m_S = +\frac{1}{2}$ have a positive slope and are therefore forced to the axis of the magnet. The hyperfine states with $m_S = -\frac{1}{2}$ have a negative slope and are forced away from the axis of the magnet.

The effective magnetic moment μ_{eff} can be calculated for the different hyperfine states of hydrogen and deuterium from the equations of the energy eigenvalues. Using the equations (2.9) for hydrogen, the effective magnetic moment μ_i^H for the hyperfine state $|i\rangle$ of a hydrogen atom is:

$$\begin{aligned} \mu_1^H &= \frac{\partial E_1^H}{\partial B} = \frac{E_{HFS}^H}{2 B_c^H} , \\ \mu_2^H &= \frac{\partial E_2^H}{\partial B} = \frac{E_{HFS}^H}{2 B_c^H} \cdot \frac{x}{\sqrt{1+x^2}} , \\ \mu_3^H &= \frac{\partial E_3^H}{\partial B} = -\frac{E_{HFS}^H}{2 B_c^H} , \\ \mu_4^H &= \frac{\partial E_4^H}{\partial B} = -\frac{E_{HFS}^H}{2 B_c^H} \cdot \frac{x}{\sqrt{1+x^2}} . \end{aligned} \quad (2.26)$$

With the approximation of $(g_S - g_I) \approx 2$ equation (2.2) simplifies to:

$$E_{HFS}^H = 2 \mu_B B_c^H . \quad (2.27)$$

The equations (2.26) can then be rewritten with the help of equation (2.27) and equation (2.23):

$$\begin{aligned} \mu_1^H &= \mu_B , \\ \mu_2^H &= \mu_B \cdot \frac{r^2}{\sqrt{\left(\frac{B_c^H}{B_{pt}}\right)^2 \cdot r_{pt}^4 + r^4}} , \\ \mu_3^H &= -\mu_B , \\ \mu_4^H &= -\mu_B \cdot \frac{r^2}{\sqrt{\left(\frac{B_c^H}{B_{pt}}\right)^2 \cdot r_{pt}^4 + r^4}} , \end{aligned} \quad (2.28)$$

showing the dependency of the effective magnetic moments on the radial position of the atom and the properties of the sextupole magnet for the mixed states.

The effective magnetic moment μ_{eff} of the different hyperfine states of a deuterium atom can be calculated analogous. With the approximation of $(g_S - g_I) \approx 2$ equation (2.2) simplifies to:

$$E_{HFS}^D = 2 \mu_B B_c^D , \quad (2.29)$$

so that the equations (2.18) can be rewritten with the help of equation (2.23):

$$\begin{aligned}
\mu_1^D &= \frac{\partial E_1^D}{\partial B} = \mu_B , \\
\mu_2^D &= \frac{\partial E_2^D}{\partial B} = \mu_B \cdot \frac{r^2 + \frac{1}{3} \frac{B_c^D}{B_{pt}} \cdot r_{pt}^2}{\sqrt{\left(\frac{B_c^D}{B_{pt}}\right)^2 \cdot r_{pt}^4 + \frac{2}{3} \frac{B_c^D}{B_{pt}} \cdot r_{pt}^2 \cdot r^2 + r^4}} , \\
\mu_3^D &= \frac{\partial E_3^D}{\partial B} = \mu_B \cdot \frac{r^2 - \frac{1}{3} \frac{B_c^D}{B_{pt}} \cdot r_{pt}^2}{\sqrt{\left(\frac{B_c^D}{B_{pt}}\right)^2 \cdot r_{pt}^4 - \frac{2}{3} \frac{B_c^D}{B_{pt}} \cdot r_{pt}^2 \cdot r^2 + r^4}} , \\
\mu_4^D &= \frac{\partial E_4^D}{\partial B} = -\mu_B , \\
\mu_5^D &= \frac{\partial E_5^D}{\partial B} = -\mu_B \cdot \frac{r^2 - \frac{1}{3} \frac{B_c^D}{B_{pt}} \cdot r_{pt}^2}{\sqrt{\left(\frac{B_c^D}{B_{pt}}\right)^2 \cdot r_{pt}^4 - \frac{2}{3} \frac{B_c^D}{B_{pt}} \cdot r_{pt}^2 \cdot r^2 + r^4}} , \\
\mu_6^D &= \frac{\partial E_6^D}{\partial B} = -\mu_B \cdot \frac{r^2 + \frac{1}{3} \frac{B_c^D}{B_{pt}} \cdot r_{pt}^2}{\sqrt{\left(\frac{B_c^D}{B_{pt}}\right)^2 \cdot r_{pt}^4 + \frac{2}{3} \frac{B_c^D}{B_{pt}} \cdot r_{pt}^2 \cdot r^2 + r^4}} . \tag{2.30}
\end{aligned}$$

2.3 Adiabatic Radio Frequency Transitions

The HERMES experiment uses radio frequency transition units e.g. to transfer the electron spin from the electron to the nucleus of hydrogen or deuterium atoms. Also depolarization of the atoms during wall collisions and resonant depolarization induced by the bunch field of the HERA positron beam are caused by the exchange of the occupation numbers of different hyperfine states.

A radio frequency transition has a defined frequency ν_{ij} , related to the energy difference $E_i - E_j$ of the transition $i - j$:

$$\nu_{ij} = \frac{|E_i - E_j|}{h} . \tag{2.31}$$

A certain transition can be induced by a radio frequency transition unit. Transition units using the exact resonance need a well defined velocity of the atoms for an efficient transition of the relative occupation numbers. This is not given for an atomic beam with a thermal velocity distribution. For this case so-called *adiabatic radio frequency transitions* have been developed [Ab58], where a gradient magnetic field along the axis of the atomic beam guarantees that the atom passes the resonance condition exactly once. The atoms entering such a transition unit experience a high frequent electromagnetic field (rf) while travelling through a weak static magnetic field that is overlayed by a gradient magnetic field which causes an exchange of occupation numbers of hyperfine states. It is called adiabatic if the relation

$$\frac{\partial B_x}{z} \ll \frac{g_S \mu_B}{\bar{v}} \cdot B_{rf}^2 \tag{2.32}$$

between the field strength of the gradient field B_x and the amplitude of the rf field B_{rf} for atoms with a mean velocity \bar{v} is fulfilled [Ab58]. A detailed description of adiabatic transitions can be found e.g. in [Ga92, Br95, Ba00]. Three different types of adiabatic radio frequency transitions (RFT) can be distinguished:

- Weak field transition (WFT): Hyperfine states of one Zeeman multiplet are exchanged according to $\Delta F = 0$ and $m_F \leftrightarrow -m_F$. The exchange is realized by multiple transitions in the Zeeman region ($x \ll 1$) where the energy splitting between neighbouring hyperfine states of a Zeeman multiplet is equidistant.
- Strong field transition (SFT): Hyperfine states of different Zeeman multiplets are exchanged if the difference in their quantum numbers is $\Delta F = \pm 1$ and $\Delta m_F = 0, \pm 1$. The transitions belonging to $\Delta m_F = 0$ are called σ transitions (the static magnet field is orientated parallel to the rf field), those with $\Delta m_F = \pm 1$ are called π transitions (the static magnet field is perpendicular to the rf field) [Ga92]. They are historically called SFTs because in the first realisation they required the strongest magnetic field.
- Medium field transition (MFT): Hyperfine states of one Zeeman multiplet are exchanged if the difference in their quantum numbers is $\Delta F = 0$ and $\Delta m_F = \pm 1, 2, 3, \dots$. The exchange of populations is realized in higher magnetic fields ($0.1 < x < 0.2$) than WFTs in order to perturb the equidistance of the energy splitting of the hyperfine states of a Zeeman multiplet.

Adiabatic radio frequency transitions exchange the population of hyperfine states with an efficiency of nearly 100% .

Chapter 3

Experimental Setup of the Target

A schematic view of the polarized hydrogen and deuterium target of the HERMES experiment is shown in figure 3.1. The target consists of an atomic beam source

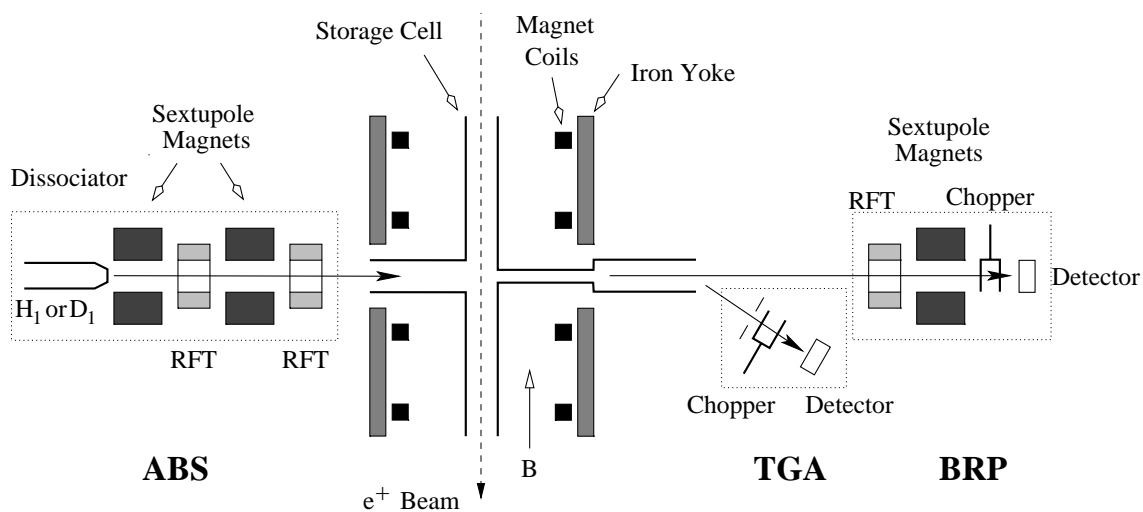


Figure 3.1:

Scheme of the HERMES target system viewed from above. The hydrogen (or also deuterium) atoms are dissociated and polarized by the atomic beam source (ABS), then fed into the storage cell which is surrounded by a magnet. A sample of this gas enters the target gas analyzer (TGA) and Breit-Rabi polarimeter (BRP) where its properties are measured.

(ABS), which injects a spin polarized beam of hydrogen or deuterium atoms into a storage cell, a Breit-Rabi polarimeter (BRP) and a target gas analyzer (TGA). In this chapter a more detailed description of these components of the target is given.

3.1 The Atomic Beam Source

The atomic beam source (ABS) is based on the principle of Stern-Gerlach separation [Hae67] of an atomic hydrogen or deuterium beam [St94b, St95, St94a]. It consists of a dissociator, a skimmer and collimator for beam formation, a sextupole magnet system and adiabatic radio frequency transition units. A schematic picture of the ABS setup is shown in figure 3.2.

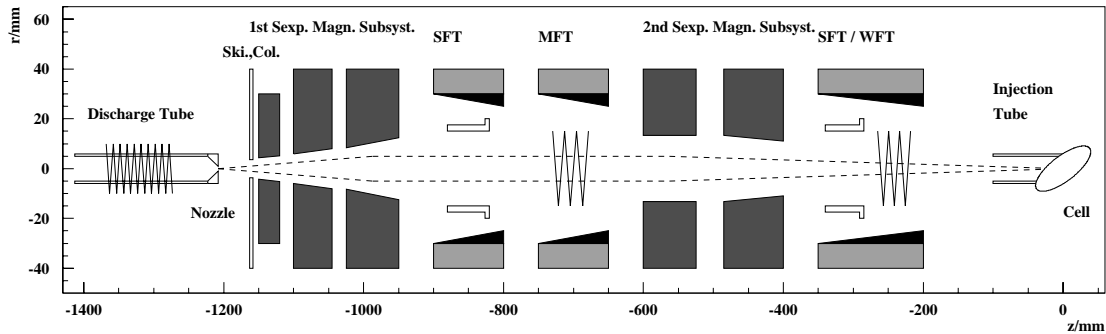


Figure 3.2:

Scheme of the HERMES atomic beam source. The molecular hydrogen or deuterium gas enters from the left and is dissociated in the discharge tube. Adiabatic gas expansion after the nozzle creates a peaked atomic beam. Skimmer and collimator are limiting its spread to the acceptance of the first sextupole magnet. Between the two parts of the magnet system radio frequency transition units (SFT, MFT) (for hydrogen only the MFT) are installed, as well as after the magnet system (SFT/WFT).

Hydrogen or deuterium molecules are dissociated into atoms by the dissociator. For hydrogen (and for the first part of the deuterium running period¹) a dissociator operating at 13.56 GHz (rf dissociator) was employed. In the year 2000 a dissociator based on a modified waveguide surfatron field applicator was installed [Koc99a, Koc99b, Koc99c], dissociating the deuterium molecules by a microwave (MW) plasma discharge in the glass tube of the dissociator. The MW dissociator operates at a frequency of 2.45 GHz with a deuterium throughput of about 92 sccm and has an admixture of oxygen of 0.15 sccm. The discharge tube ends in an aluminum nozzle that is cooled to 100 ± 1 K to minimize recombination processes. The oxygen improves the output intensity and due to the cooling, ice starts building up on the nozzle which has the advantage of prohibiting recombination. After two to three days of continuous running this ice has to be removed since it increases the pressure at the nozzle and decreases the throughput. Therefore the cooling of the nozzle is turned off so that the ice evaporates and is pumped away. This is called

¹Since July 1998 HERMES has been running with deuterium gas instead of hydrogen.

nozzle regeneration.

The ABS has a powerful differential pumping system consisting of several turbomolecular and cryogenic (cryo) pumps in the four ABS chambers (dissociator -, skimmer -, 1st and 2nd sextupole chamber) with a total pumping speed of about 15000 ls^{-1} . The pressure in the last chamber, which is connected to the target vacuum chamber via a small injection tube, is in the same order of magnitude as the target chamber pressure of about 10^{-7} mbar.

An expansion of the atoms from the dissociator into the vacuum occurs after the cold nozzle, creating a forward peaked beam. A conical skimmer and collimator limit the spread of this beam to the acceptance of the first sextupole magnet.

The ABS magnet system consists of a total of five segmented permanent sextupole magnets with high pole tip fields of about 1.45 T. Each magnet focuses atoms in the electron spin state $m_S = +\frac{1}{2}$ and defocuses atoms with $m_S = -\frac{1}{2}$ out of the atomic beam, according to the Stern-Gerlach spin separation (ch. 2.2). This magnet system is separated in two parts. The first three magnets focus the atoms either on parallel trajectories or trajectories that cross the axis of the magnet once before they reach the last two magnets which focus these atoms into the injection tube, through which they are fed into the storage cell.

Between the two parts of the magnet system and after the last magnet (in the so-called appendix chamber) adiabatic radio frequency transition (RFT) units are installed. The system of RFTs and sextupole magnets are used to transfer the polarization of the electron spin to the nuclear spin or to select certain states for systematic studies.

The transition units are placed in a window-frame static magnet with coils to produce a homogeneous field. The rf coils are located within the range of the gradient field coils which produce a linearly either in- or decreasing static field. For the SFTs in the HERMES experiment the rf field is produced by a 2 rod resonant line which is embedded in a cavity [Ga92]. These units have been built as $\frac{\lambda}{4}$ resonators. The ABS uses a MFT for hydrogen and deuterium and a SFT only for deuterium between the two parts of the magnet system. The transition unit in the appendix chamber can only either be used as a SFT or as a WFT at a time since there is only one static and gradient field that has to be set for either transition.

The polarized atomic beam from the ABS is ballistically injected via the injection tube into the storage cell, where the atoms are exposed to the HERA positron beam (Fig. 3.3).

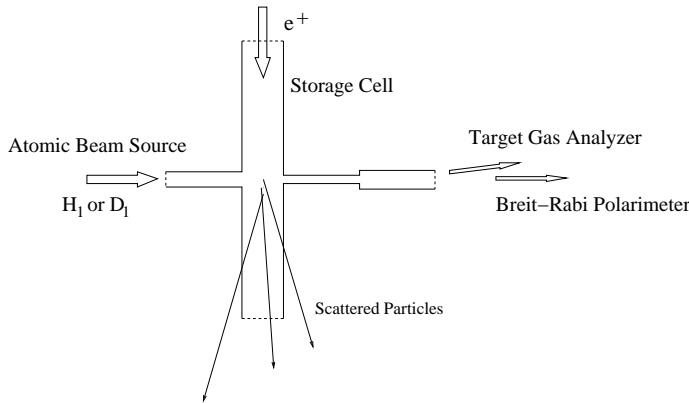


Figure 3.3:

View of the target cell from above showing the injection tube on the left side and the sample and extension tube on the right side. The positron beam of the HERA storage ring passes through the cell.

3.2 The Storage Cell

The HERMES storage cell [Stw95b] is an open-ended 400 mm long tube made out of pure thin aluminum with a thickness of only 75 μm . The target cell has an elliptical cross section of 21 mm \times 8.9 mm. These dimensions are optimized for high target density without interfering the HERA positron beam². Physically the cell is 147 mm longer in the downstream direction as shown in figure 3.4. This extension ensures

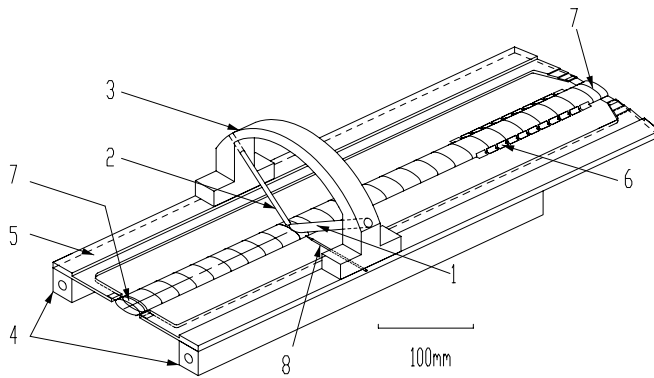


Figure 3.4:

The HERMES target cell [Stw95a] viewed from the upstream direction: 1) Injection tube; 2) Sample tube (extension tube not shown); 3) Tube support arch; 4) Cryogenic cooling and support rails; 5) Support plates; 6) Cell extension with pumping apertures; 7) Cell end support collar; 8) Unpolarized gas feed capillary.

that all scattered particles inside the spectrometer detector acceptance pass through the same thickness of material [Stw95b].

The storage cell is coated with a substance called Drifilm [Stn95] in order to minimize spin relaxation and atomic recombination processes by wall collisions. It has similar properties to a teflon coating but is more resistant to synchrotron radiation.

The atoms in the cell diffuse randomly, their velocity distributed according to a

²A bigger cell was installed until November 1999 having the dimensions: 29 mm \times 9.8 mm; the smallest cell that was ever installed (January 1999) was 19 mm \times 8.0 mm.

Maxwell distribution. To increase the target density the cell is cooled with gaseous helium flowing through the support rails to about 95 K for hydrogen and around 65 K for deuterium. Due to the oxygen admixture in the hydrogen or deuterium beam water is formed which can be adsorbed by the cold cell wall. These water molecules occupy sites that could have been occupied by a hydrogen or deuterium atom. This reduces the probability of recombination and spin relaxation since these processes mainly happen while the atoms are sticking to the wall. When the cell is cooled down to lower temperatures than 95 K for hydrogen or 65 K for deuterium the probability of these processes increases again due to the exponential increase of the sticking time on the cell wall.

The storage cell is mounted in the target vacuum chamber by the support rails only on the upstream end of the cell since the cell undergoes thermal extension. The target vacuum chamber is surrounded by the longitudinal target magnet, which is a superconducting magnet designed to operate up to 350 mT. Four short coils generate a highly homogeneous longitudinal holding field and an iron flux return yoke minimizes the stray field at the position of the ABS and the target gas analyzer. This magnetic holding field provides the quantization axis for the spins of the polarized atoms in the storage cell, decouples the spin of the electron from the spin of the nucleon and reduces relaxation processes of the nuclear spins.

It is possible to inject unpolarized gas, i.e. H_2 , D_2 , He , N_2 , Ne or Kr from the unpolarised gas feed system (UGFS) through a small capillary right into the center of the cell (Fig. 3.5). In addition to normal unpolarized running, at the end of HERA fills high density unpolarized measurements were done with about 100 times the ABS output density.

The atoms injected by the ABS diffuse in the storage cell, changing their direction and velocity (Maxwell distributed) randomly at each wall bounce, generating a triangular shaped density distribution along the beam axis. The escaping gas is removed from the storage ring by high speed vacuum pumps. The residual gas in this system produces a small source of unpolarized molecules in the storage cell. It can be assumed that the atoms are physisorbed [Kol98, Ba00] at the wall for a short time before they desorb back into the gas phase according to a $\cos\theta$ distribution. After a few wallbounces the atoms have thermalized with the storage cell wall.

The properties of the target gas in the cell are continuously monitored by a target gas analyzer and a Breit-Rabi polarimeter. The sample tube that leads to these detectors is tilted in respect to the axis of the injection tube, i.e. there is no straight connection between ABS and the detectors, to make sure that the sampled atoms have thermalized with the storage cell wall. A Monte Carlo simulation³ showed that

³This Monte Carlo simulation was done for the large cell. The values expected for the medium sized cell are higher.

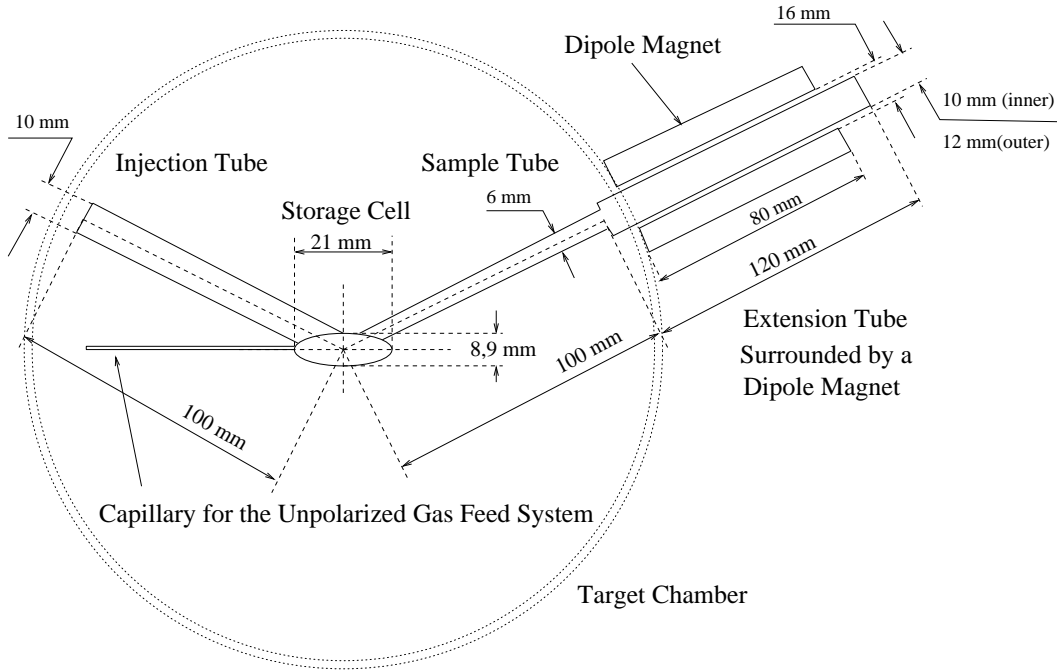


Figure 3.5:

Detailed view of the target cell from the downstream direction showing the sizes of the injection, sample and extension tube as well as the capillary of the unpolarized gas feed system (UGFS). Only the extension tube is mounted outside the target chamber and is surrounded by a dipole magnet to ensure an extension of the target magnet field to reduce relaxation processes. The dimensions of the cell refer to the “medium sized” cell.

on average a particle detected by the Breit-Rabi polarimeter has undergone about 423 wallbounces and a particle detected by the target gas analyzer has undergone about 667 wallbounces [Hen98].

The sample tube is extended by the so-called extension tube outside the target chamber (Fig. 3.5) which is surrounded by a dipole magnet to ensure a strong holding field as provided in the target chamber by the target magnet. After installation of a cell the extension tube has to be screwed onto the sample tube from outside the target chamber, having an unknown thermal contact. Due to the close mounting of the dipole magnet around the extension tube the heat radiation causes a temperature gradient in the extension tube since the end screwed to the sample tube has about the same temperature as the sample tube. The sample tube is at the same temperature as the cell since they are both mounted on the cooling frame. At 300 K the system is in a state of thermal equilibrium and the temperature of the cell and the extension tube are the same. With a cold cell the extension tube temperature is between the temperature of the cell and the temperature of the dipole magnet (ch. 4). The temperature at the end of the extension tube is monitored by a thermo

couple.

3.3 The Target Gas Analyzer

The average target polarization P^T , as it is seen by the positron beam, includes the polarization of molecules (eq. (1.4)). Molecules from recombination of atoms, unpolarized molecules due to ballistic flow of undissociated gas injected by the ABS and a fraction of the target chamber gas which is present in the cell, give a contribution to the target density. These contributions need to be measured to avoid systematic uncertainties in the determination of the target polarization. A target gas analyzer (TGA) was developed for the HERMES target and is used to monitor the relative density of atomic and molecular hydrogen or deuterium in the cell [Ba96, Kol98].

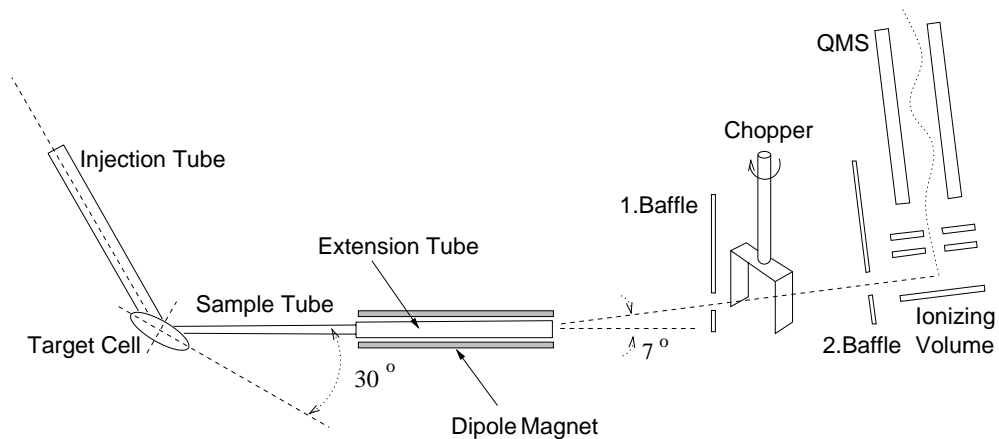


Figure 3.6:

Scheme of the target gas analyzer. The beam leaving the extension tube is chopped and analyzed in a quadrupole mass spectrometer (QMS). The first baffle rejects gas flow from sources other than the sample tube. The second baffle collimates the beam so that no particle from the beam hits the walls of the ionizing volume.

The TGA, consisting of a chopper, baffles and a quadrupole mass spectrometer (Fig. 3.6), is mounted at an angle of 7° off axis of the extension tube not to interfere with the Breit-Rabi polarimeter. A chopper in between the baffles is needed to subtract the count rate caused by the background gas. The TGA chamber is part of the vacuum system of the Breit-Rabi polarimeter.

The atoms and molecules are detected by ionization in a quadrupole mass spectrometer with a crossed-beam ionizer geometry (Fig. 3.7). On the left of figure 3.7 the ionizing volume is shown. The ionizing electrons emitted by the filament are accelerated by applying a differential potential between anode and cathode of about

70 eV. The atoms and molecules that enter the ionizing volume perpendicular to the quadrupole rods are ionized by these electrons and then formed to an ion beam by the extractor. Particles with certain atomic masses (e.g. mass one and two for hydrogen and mass two and four for deuterium) pass through the alternating electric field of the quadrupole rods and are then focused into the channeltron by the deflectors. The channeltron is installed at 90 degrees in respect to the quadrupole rods in order to reject neutral particles.

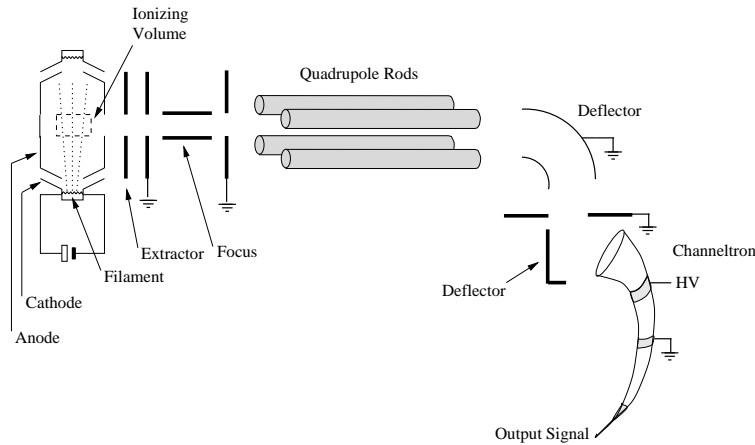


Figure 3.7:
Setup of the quadrupole mass spectrometer (QMS) including an ionizing volume, ion-optics and a channeltron detector for single ion detection.

To deduce the degree of dissociation in the cell from the TGA measurements the relative detection sensitivity of atomic and molecular masses of the TGA needs to be obtained as well as the temperature dependence of the measured signals (chapter 4).

3.4 The Breit-Rabi Polarimeter

The electron and nuclear polarization of a thermal atomic hydrogen or deuterium beam can be determined by measuring the relative occupation numbers of its hyperfine states. The HERMES experiment uses a Breit-Rabi polarimeter [Ga92, He93, Kol95, Br97, Br95] for this purpose.

The Breit-Rabi polarimeter (BRP) is located along the axis of the extension tube. It consists of adiabatic radio frequency transitions, a system of sextupole magnets, a chopper and a quadrupole mass spectrometer (QMS) (Fig. 3.8). The particles diffusing from the cell pass the adiabatic radio frequency transition (RFT) units in the first BRP chamber, where their hyperfine state populations can be interchanged.

As in the ABS the sextupole magnet system deflects atoms in hyperfine states where the electron spin is $m_S = -\frac{1}{2}$. Due to the small magnetic force close to the axis a beam blocker is installed to suppress the transmission of particles having the wrong electron spin projection ($m_S = -\frac{1}{2}$). The beam blocker is a circular metal plate

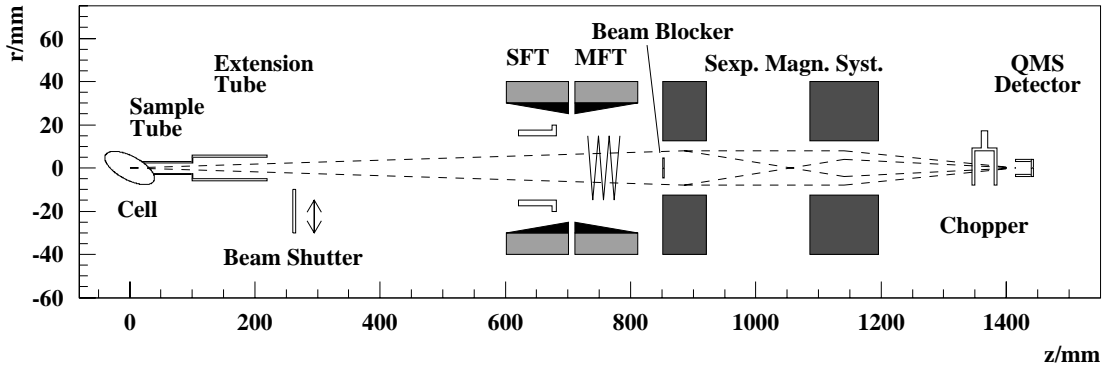


Figure 3.8:

Scheme of the Breit-Rabi polarimeter (BRP). The particles which leave through the sample tube enter the HFT units followed by the sextupole system which selects certain states that are detected in the QMS detector.

with a diameter of 9 mm centered on the axis of the first sextupole magnet having a pole tip diameter of 25 mm. The hyperfine states with electron spin projection $m_S = +\frac{1}{2}$ are focused into the detector which consists of a chopper, a QMS and a channeltron for single ion detection, similar to the detector of the TGA.

The vacuum system of the BRP is a differential pumping system (Fig. 3.9) which consists of the sextupole chamber and the detector chamber with a total pumping speed of 6000 ls^{-1} (Fig. 3.9). The chamber pressures during operation are listed in table 3.1. The TGA chamber is part of the BRP vacuum system and is located between the target chamber and the sextupole chamber. A water beam which can

| chamber | pumps | pressure |
|-----------|------------------------|---------------------------|
| TGA | Ti-Sublim. | $4 \cdot 10^{-9}$ mbar |
| Sextupole | $2 \times$ Cryo | $2 \cdot 10^{-9}$ mbar |
| Detector | Ti-Sublim., Ion Getter | $2.5 \cdot 10^{-10}$ mbar |

Table 3.1:

BRP and TGA chamber pressure readouts during normal operation.

appear as an artifact of the differential pumping system can contribute to the measurement of the the BRP detector by means of dissociative ionization. In order to subtract this kind of background a beam shutter is installed after the extension tube.

The BRP and the TGA are mounted together on rails on top of a frame so that they can be moved away from the HERA beam axis e.g for the exchange of a storage cell. After the installation of a cell the alignment of the BRP in respect to the extension tube can be optically checked with a telescope. The telescope can be mounted at a window on the axis of the sextupole magnet at the end of the BRP. The position

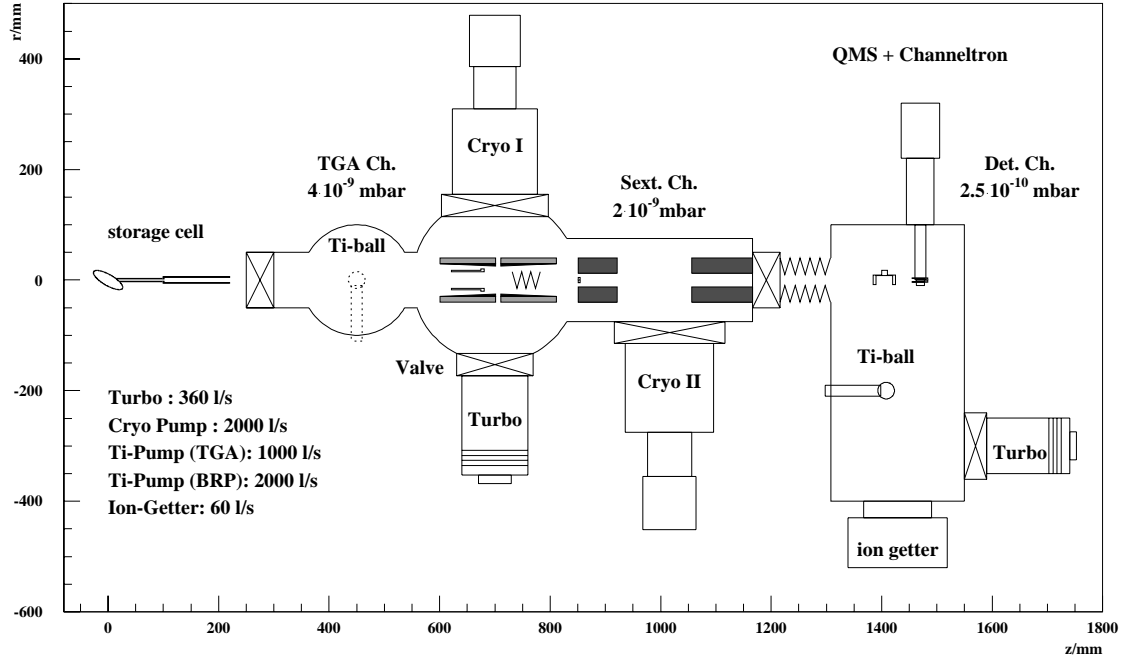


Figure 3.9:

The Breit-Rabi polarimeter vacuum system viewed from the downstream direction. The adiabatic hyperfine transitions and the sextupole system are located in the sextupole chamber (middle), the QMS and the channeltron of the BRP are located in the detector chamber (right). Two turbo molecular pumps are used to pump down from atmospheric pressure.

of the BRP can be examined with the help of the beam blocker in front of the first sextupole magnet and an alignment cross mounted in front of the second sextupole magnet.

The two RFT units of the BRP, i.e. SFT and MFT, can run on different transitions, which requires a change in the setting of static and gradient fields. Due to the close mounting of the transition units there is cross talk between the magnetic fields of the SFT and MFT. The difference in the magnetic field for the different MFT transition settings is small enough to have no influence on the SFT, whereas the big difference in the magnetic field values of the SFT transitions shows a definite effect on the MFT. Also the target gas analyzer is influenced by the different settings of the transitions of the BRP. In long measurements this fluctuation in the TGA count rates is averaged out because the transitions are switched randomly.

A measurement of the polarization is carried out as a sequence of measurements with different hyperfine transitions switched on, which change the signals measured in the detector dependent on the initial occupation of the hyperfine states. Transitions available in the BRP are the medium and strong field transitions MFT 1-3, MFT 2-3, SFT 1-4, and SFT 2-4 for hydrogen and MFT 1-4, MFT 2-4, MFT 3-4, SFT 1-6,

SFT 2-6, SFT 2-5/3-6, and SFT 3-5 for deuterium.

The target system for the two HERMES polarized target gases is shown in figure 3.10. Details of the RFT units are written below the symbols of the transition units for hydrogen gas and above the symbols for deuterium gas. The first transition unit (SFT) between the magnets in the atomic beam source has not been used for hydrogen.

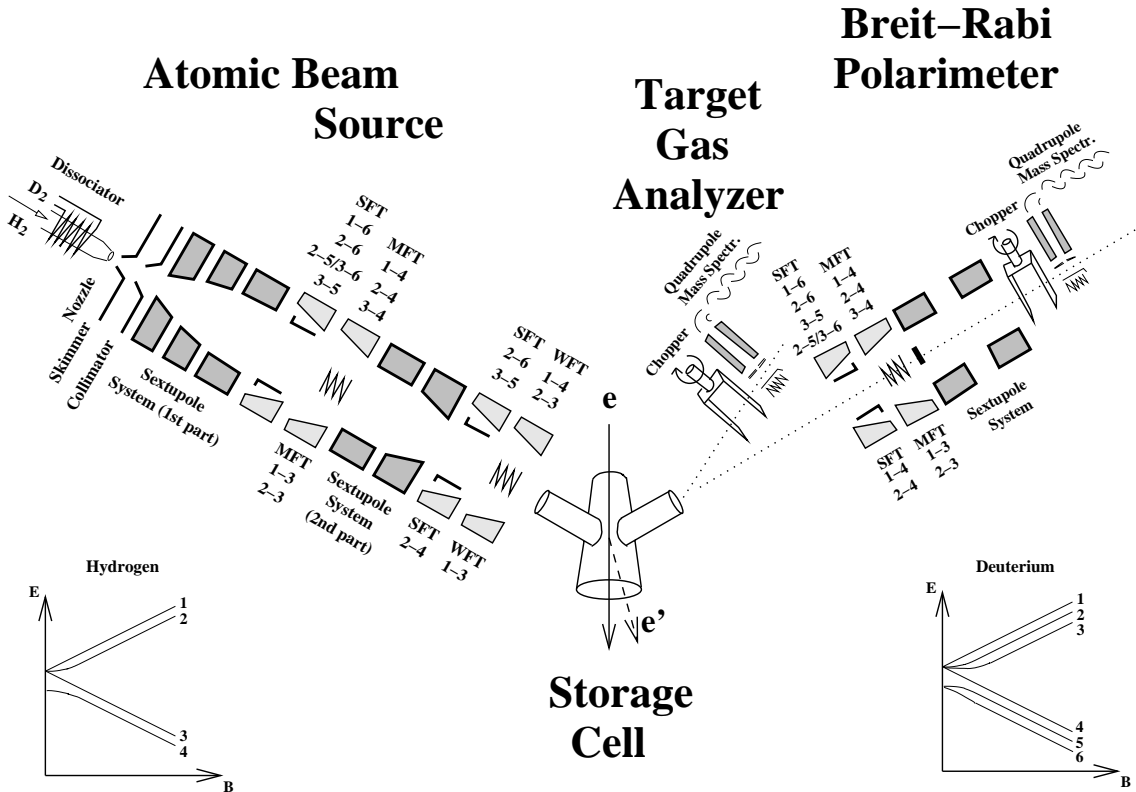


Figure 3.10: Detailed scheme: of the target system from the downstream direction. In the lower corners sketches of the hyperfine splitting of hydrogen and deuterium are drawn to show which states are exchanged in the RFT units (STF, MFT, WFT) of the atomic beam source and Breit-Rabi polarimeter. The numbers below the symbols of the transition units refer to hydrogen, the numbers above the symbols refer to deuterium.

Chapter 4

Calibration of the TGA

The target gas analyzer (TGA) measures the nucleon flow rates for atoms and molecules leaving the target cell via the sample tube. The TGA has to be calibrated for its different sensitivity of detecting atoms compared to molecules.

In this chapter the calibration method is explained and the results for the deuterium running period of the HERMES experiment are presented. The calibration for the hydrogen running period can be found in [Kol98, Ba00].

4.1 Method

The degree of dissociation α^{TGA} measured by the TGA is defined using the nucleon flow rates into the TGA:

$$\alpha^{TGA} = \frac{\phi_a^{TGA}}{\phi_a^{TGA} + \phi_m^{TGA}} , \quad (4.1)$$

where ϕ_a^{TGA} is the flow rate of nucleons coming from atoms and ϕ_m^{TGA} is the flow rate of nucleons coming from molecules. These nuclear flow rates are related to the atomic and molecular flow rates (Φ_a^{TGA} and Φ_m^{TGA} , respectively) according to:

$$\begin{aligned} \phi_a^{TGA} &= \Phi_a^{TGA} , \\ \phi_m^{TGA} &= 2 \cdot \Phi_m^{TGA} . \end{aligned} \quad (4.2)$$

The value α^{TGA} gives information on the degree of dissociation of the thermalized beam which left the target cell via the sample tube. The total number of nucleons being sampled by the TGA is proportional to the number of nucleons present in the cell which is proportional to the number of nucleons injected into the cell by the ABS. Therefore the total nucleon flow rate into the TGA Φ_{tot}^{TGA} is proportional to

the total nucleon flow rate injected into the cell Φ_{tot}^{ABS}

$$\Phi_{tot}^{TGA} = \Phi_a^{TGA} + 2 \cdot \Phi_m^{TGA} = C \cdot \Phi_{tot}^{ABS} . \quad (4.3)$$

The channeltron of the TGA measures the count rates S_a^{TGA} and S_m^{TGA} for atoms and molecules, respectively. These count rates are proportional to the corresponding atomic and molecular flow rates into the TGA:

$$S_i^{TGA} \propto I_{emis} \frac{\varepsilon_i \sigma_i^{ion}}{\bar{v}_i} \Phi_i^{TGA} , \quad (4.4)$$

with $i = a, m$ for atoms and molecules, respectively. Here I_{emis} is the emission current of the ionizing volume of the TGA ion-optics, σ_i^{ion} is the ionization cross section and ε_i is the detection probability. The probability for ionization is proportional to the time the atoms or molecules need to pass the ionizing volume and is therefore invers proportional to the averaged velocity \bar{v}_i of the particles.

Equation (4.3) can now be rewritten with the help of equation (4.4) to:

$$\Phi_{total}^{TGA} \cdot \frac{\varepsilon_a \sigma_a^{ion}}{\bar{v}_a} = \frac{S_a^{TGA}}{I_{emis}} + 2 \cdot \frac{\bar{v}_m}{\bar{v}_a} \cdot \frac{\varepsilon_a \sigma_a^{ion}}{\varepsilon_m \sigma_m^{ion}} \cdot \frac{S_m^{TGA}}{I_{emis}} , \quad (4.5)$$

which results in an equation for the degree of dissociation using equation (4.1) of:

$$\alpha^{TGA} = \frac{\frac{S_a^{TGA}}{I_{emis}}}{\frac{S_a^{TGA}}{I_{emis}} + 2 \cdot \frac{\bar{v}_m}{\bar{v}_a} \cdot \frac{\varepsilon_a \sigma_a^{ion}}{\varepsilon_m \sigma_m^{ion}} \cdot \frac{S_m^{TGA}}{I_{emis}}} . \quad (4.6)$$

A relative calibration constant κ can be defined as:

$$\kappa = \frac{\varepsilon_a \sigma_a^{ion}}{\varepsilon_m \sigma_m^{ion}} , \quad (4.7)$$

which describes the relative detection sensitivity of atoms compared to molecules in the TGA.

Since the detected particles have thermalized with the extension tube, with their velocity distributed according to a Maxwellian distribution, their average velocity can be written as:

$$\bar{v} = \sqrt{\frac{8k_B T_{ext}}{\pi m}} , \quad (4.8)$$

where k_B is the Boltzman factor. Due to this (eq. (4.8)) and the fact that the mass of a molecule is twice as big as the mass of an atom for hydrogen as well as for deuterium ($\frac{\bar{v}_m}{\bar{v}_a} = \frac{1}{\sqrt{2}}$) equation (4.6) simplifies to:

$$\alpha^{TGA} = \frac{S_a^{TGA}}{S_a^{TGA} + \sqrt{2} \kappa \cdot S_m^{TGA}} . \quad (4.9)$$

Assuming a constant ABS flux in equation (4.3), no temperature dependence of the count rates and using the correlations found, an equation for the corrected TGA count rates can be given:

$$\frac{S_a^{TGA}}{I_{emis}} + \sqrt{2} \kappa \cdot \frac{S_m^{TGA}}{I_{emis}} = constant , \quad (4.10)$$

so that plotting $\frac{S_m^{TGA}}{I_{emis}}$ as a function of $\frac{S_a^{TGA}}{I_{emis}}$ for different degrees of dissociation results in a straight line (Fig. 4.1) with a slope of

$$\frac{\partial \left(\frac{S_m^{TGA}}{I_{emis}} \right)}{\partial \left(\frac{S_a^{TGA}}{I_{emis}} \right)} = - \frac{1}{\sqrt{2} \kappa} . \quad (4.11)$$

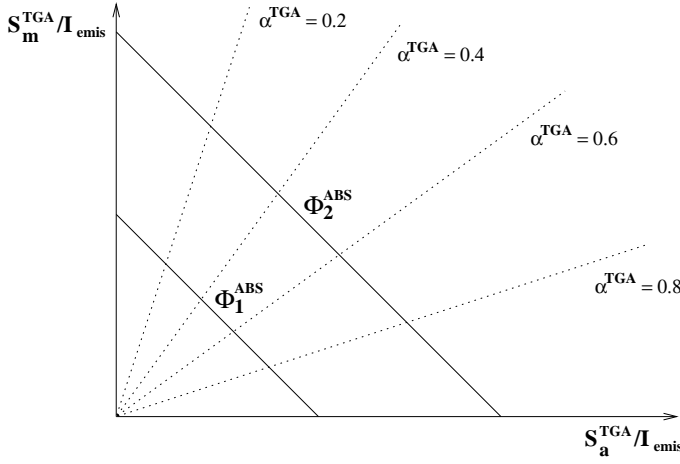


Figure 4.1:

The corrected molecular count rate as a function of the corrected atomic count rate of the TGA for different degrees of dissociation α^{TGA} at constant ABS flux $\Phi_1^{ABS} < \Phi_2^{ABS}$.

To obtain a plot similar to figure 4.1, the degree of dissociation has to be varied. This can be achieved by two different methods:

- variation of the temperature of the target cell (so-called temperature scan) since the recombination process is strongly temperature dependent (see section 4.2),
- monitoring the recovery of the cell after an accidental loss of a part of the HERA positron beam in the target region (so-called beam dump)(see section 4.3).

4.2 Temperature Scans

The variation of the cell temperature changes the degree of dissociation. A temperature scan is performed by changing the helium flow through the cooling rails of the

cell, then leaving the system untouched for about an hour to get a definite step with constant temperature. This is then done for various temperatures. Temperature scans are usually performed with the atomic beam source (ABS) alternating between four different two state injection modes and a three state injection mode in order to obtain better statistics. Since the count rates for the three state injection are about a factor of 1.5 higher than for two state injection, those two cases have to be analyzed separately resulting in two values for κ (κ_2 and κ_3 for two and three state injection mode, respectively) which can then be averaged.

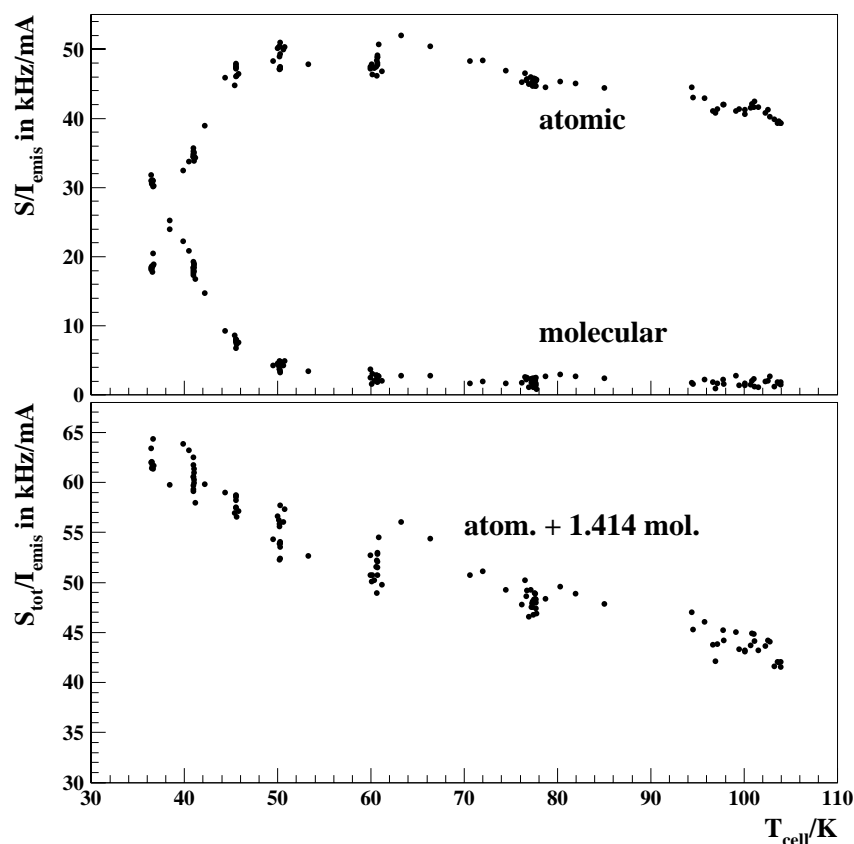


Figure 4.2:
Plot of the corrected atomic and molecular count rates over the cell temperature (upper plot) and the sum of the corrected atomic count rate and $\sqrt{2}$ times the corrected molecular count rate for a temperature scan performed on August 19th, 1999.

Data from a temperature scan on August 19th, 1999 is shown in figure 4.2. In the upper plot the corrected atomic and molecular count rates are plotted as a function of the temperature of the cell. It shows the decrease of the atomic count rate for low temperatures while the molecular count rate is increasing. The sum of the corrected atomic and molecular count rates plotted in the lower plot shows a deviation from a constant. This is partly due to the different sensitivity of the ion-optics for atoms and molecules, but is also a temperature effect. To distinguish between these two effects unpolarized data can be analyzed as described in the following section.

4.2.1 The Temperature Correction

An unpolarized temperature scan is performed by injecting unpolarized gas by the unpolarized gas feed system (UGFS) into the center of the storage cell via a capillary and varying the cell temperature as in the case of polarized gas. Using the UGFS only molecules are injected, so that a variation of the molecular count rate in the TGA is either due to a change in the injected flux of the UGFS or a temperature effect.

Data from an unpolarized temperature scan performed on April 27th 1999 is shown in figure 4.3. On the left side the molecular count rate divided by the emission

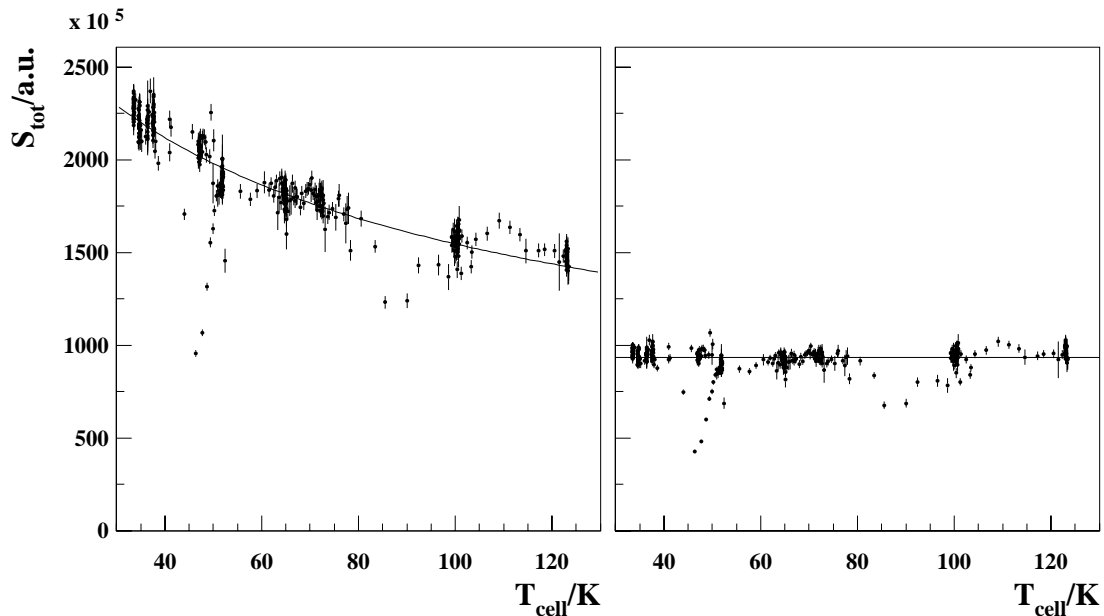


Figure 4.3:

Plot of the corrected (by the emission current and the pressure) molecular count rate over the cell temperature from an unpolarized temperature scan of April 27th, 1999 without (left plot) and with (right plot) a temperature correction.

current and the pressure in the target chamber is plotted over the cell temperature, showing a definite dependence on the temperature.

All particles detected by the TGA are thermalized by the extension tube since they cannot be detected without having at least one wall bounce on the extension tube. Therefore the temperature of the extension tube is the temperature determining the kinetic energy of the particle. Due to the unknown thermal contact between the extension tube and the sample tube and the heat radiation from the dipole magnet surrounding the extension tube the temperature of the cell is not equal to the temperature of the extension tube.

Therefore a temperature correction function of:

$$f(T_{ext}) = \sqrt{\frac{T_{ext}}{300}} \quad (4.12)$$

has to be applied. The data of the unpolarized temperature scan with this temperature correction function is now constant over the cell temperature (right side of figure 4.3).

4.2.2 Analyzing a Temperature Scan

The temperature correction function found for the unpolarized data can be applied to the data from the polarized temperature scans on August 19th, 1999 resulting in figure 4.4. The temperature corrected sum of the atomic and molecular count rate is

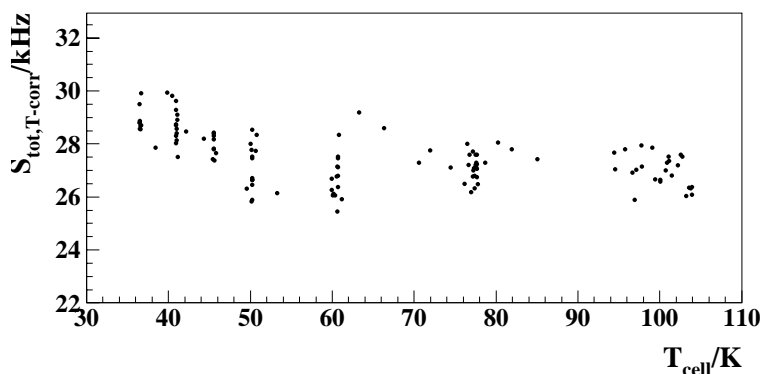


Figure 4.4:

Plot of the temperature corrected sum of the atomic count rate and $\sqrt{2}$ times the molecular count rates over the cell temperature for data from a temperature scan performed on August 19th, 1999.

now a constant over temperature for cell temperatures down to about 50 K. The small deviation seen for lower temperatures can be attributed to a higher sensitivity of the TGA to detect molecules compared to atoms. This relative detection sensitivity is called κ .

Data from a polarized temperature scan performed on August 19th, 1999 is shown in figure 4.5 with temperature steps ranging from 38 K to 92 K. As described the temperature of the extension tube is higher than the temperature of the cell. It can be seen in the lower plot that the degree of dissociation only changes for the lowest 5 or 6 temperature steps. For the calibration of the TGA, only this temperature range is used and the data is averaged over the periods of constant temperature.

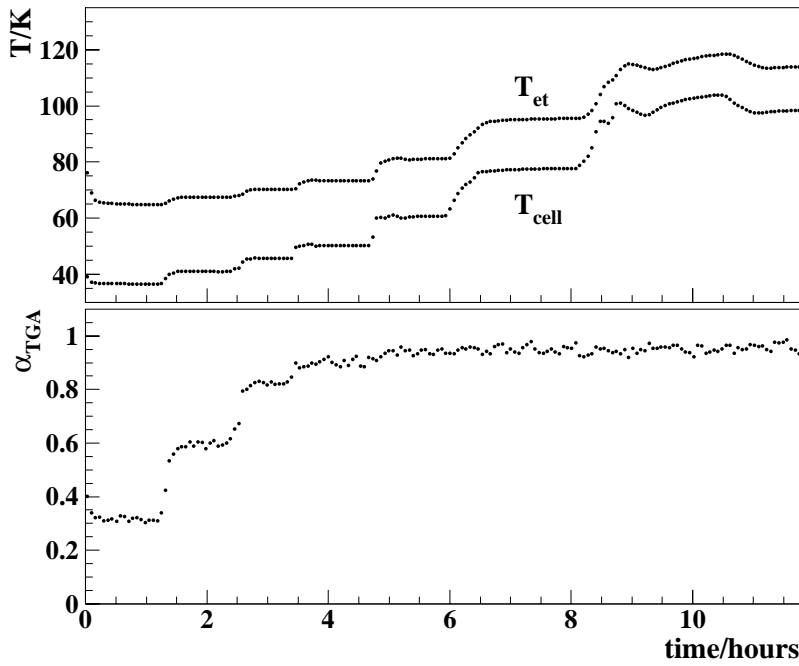


Figure 4.5:
 Temperature Scan
 on August 19th,
 1999: The tempera-
 ture steps seen in
 the upper plot result
 in steps in the degree
 of dissociation α^{TGA}
 (lower plot).

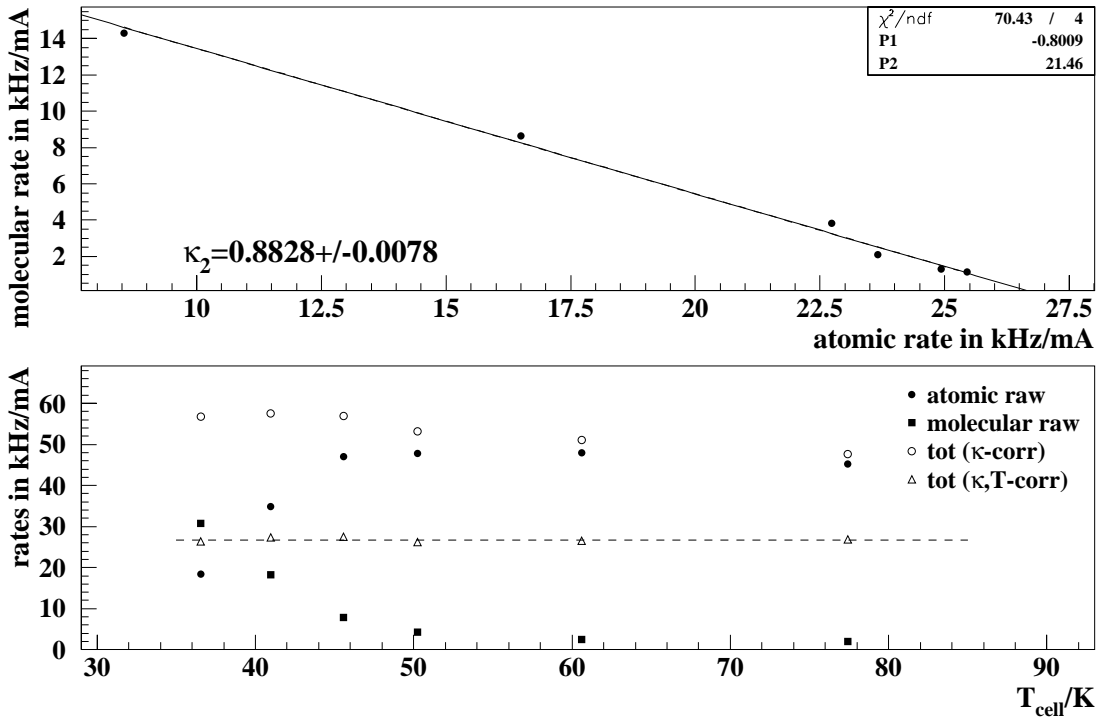


Figure 4.6:
 Plot of the corrected atomic and molecular count rates over the cell temperature (upper
 plot) with the fit and the resulting value for κ_2 for two state injection during the tem-
 perature scan on August 19th, 1999. The lower plot shows raw and corrected count rates.

A result of this analysis for two state injection is shown in figure 4.6. The slope of a linear function fitted to the data points in the upper plot of figure 4.6 is $m = -0.8009 \pm 0.0071$ resulting in a κ_2 of:

$$\kappa_2 = 0.8828 \pm 0.078 \quad . \quad (4.13)$$

The lower plot of figure 4.6 shows various corrected count rates. The averaged *raw* atomic and molecular count rates are background and emission current corrected (plotted as filled symbols). The total count rate using κ_2 but not being temperature corrected is plotted as open circles. The open triangles show the total count rate with the temperature correction (found in the unpolarized data) and the κ_2 value derived from the fit in the upper plot. These points are constant over temperature (dashed line), showing that a proper correction has been applied and the requirement of a constant ABS flux for the extraction of κ is fulfilled.

4.3 HERA Beam Dumps

A fraction of the HERA positron beam can accidentally get *lost* e.g. radiate a bunch of synchrotron photons into something in the beam tube. The loss of the positron beam in the vicinity of the target cell results in a damage of the adsorbed water layer coating the surface of the cell, resulting in an increased recombination probability. The subsequent adsorption of water on the target cell walls entails the recovery of the degree of dissociation in the time scale of a few hours. This happens at a constant temperature of the cell so that no temperature correction for the count rates is needed.

Since beam dumps occur unexpectedly, the ABS is usually either in one, two or three state injection mode. Therefore usually only one κ value is extracted from the data.

A plot from a beam dump that happened on August 7th, 1999 is shown in figure 4.7. The plot in the middle shows the current of the HERA positron beam. A sudden drop in the current (at about 1 hour) is due to a loss of a fraction of the beam. At the same time the degree of dissociation α^{TGA} has a sudden drop (upper plot). The recovery of α^{TGA} can be used to determine κ , as long as the cell temperature is constant (lower plot).

For a beam dump the count rates of the TGA only have to be corrected for the emission current. A plot of the corrected molecular count rate over the corrected atomic count rate is shown in figure 4.8. The straight line fitted to the data points has a slope of $m = -0.8343 \pm 0.0282$ resulting in a κ_2 of:

$$\kappa_2 = 0.8475 \pm 0.0286 \quad . \quad (4.14)$$

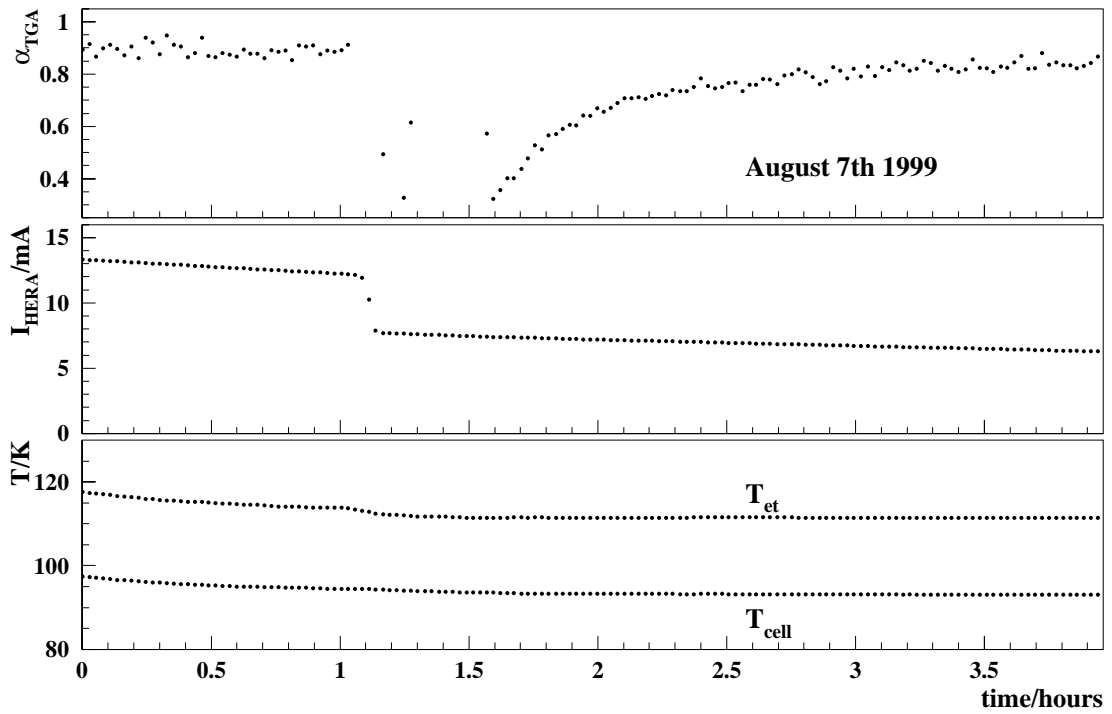


Figure 4.7:
 Characteristic plot of a beam dump: A sudden loss in the HERA beam current results in a drop of the degree of dissociation α^{TGA} . A beam dump can only be analyzed if the cell temperature is constant.

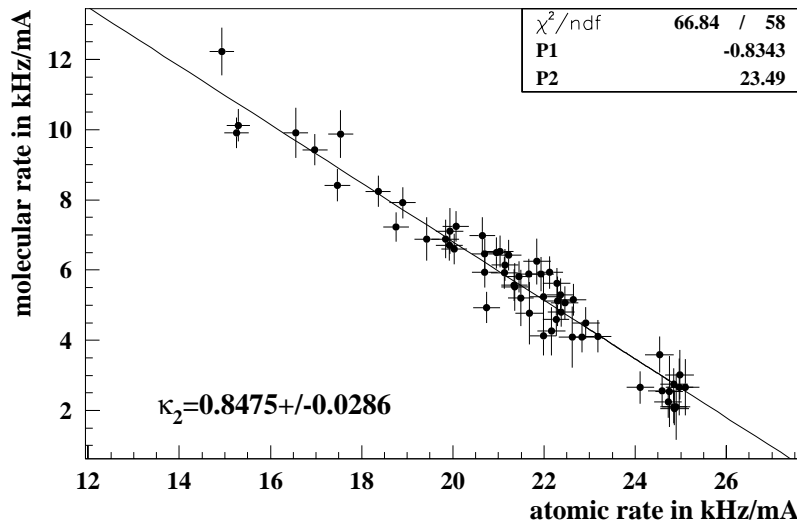


Figure 4.8:
 The corrected molecular count rate is plotted over the corrected atomic count rate and from a straight line fitted to the data κ_2 has been determined.

This value shows good agreement with the value obtained from the calibration method using a temperature scan.

4.4 The Year 2000

Recombination processes are minimized by a storage cell that has a thick Drifilm coating and in addition a layer of adsorbed water. A target cell (cell number 13) was installed in December 1999 and stayed inside the experiment until the big HERA shutdown¹ in September 2000. The vacuum system was not vented in the period December 1999 until September 2000 and the cell was mostly cooled to 65 K. In the same period the atomic beam source ran with the microwave dissociator, having a higher oxygen admixture than the rf dissociator. All this might have entailed the adsorption of more water on the cell surface than in the year before. All this and the fact that the Drifilm coating was extremely thick resulted in an extraordinary performance. Down to temperatures of about 49K (120-49K) the α^{TGA} never dropped lower than 0.96. The processes depolarization and recombination by wall collisions depend on the sticking time of the atoms on the wall and the sticking time depends exponentially on the temperature of the cell. In the year 2000 no temperature dependence of the degree of dissociation was seen. From this it can be derived that

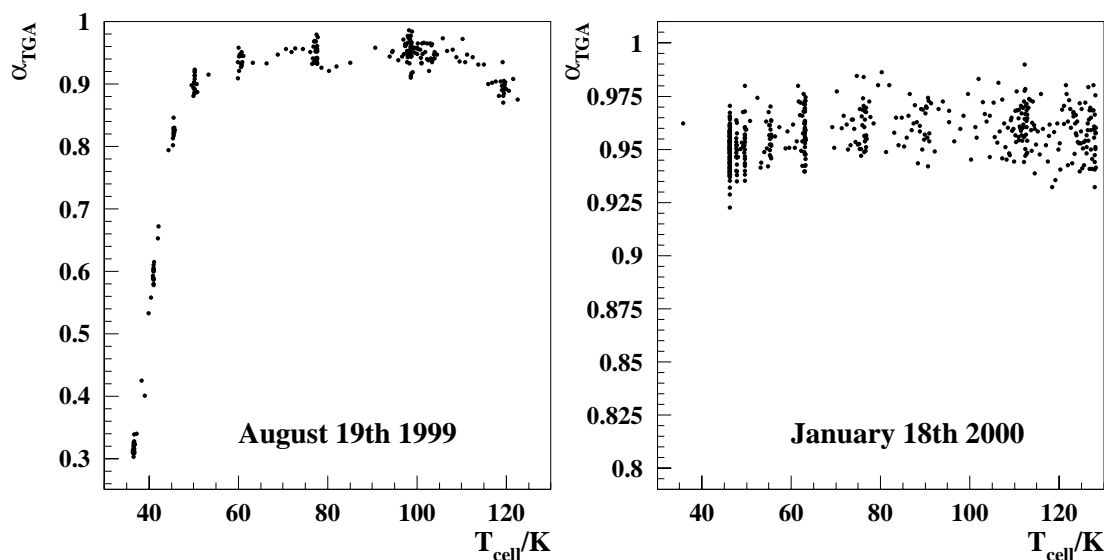


Figure 4.9:

Comparison of a temperature scan performed in the year 1999 (left plot) and one performed in the year 2000 (right plot). Note the different scaling of the y-axis for the two plots.

¹HERA is shutdown for an upgrade of the accelerator ring. The shutdown started September 2000 and the planned end is June 2001.

there was no recombination inside the cell. The deviation of $\alpha^{TGA} = 0.96$ from 1 can be explained by the fraction of molecules injected into the cell by the ABS and residual molecules present in the target chamber.

Regular temperature scans were performed six times in the year 2000 without showing a significant change in α^{TGA} . A comparison of a temperature scan from the year 2000 and from the year 1999 is shown in figure 4.9. From these temperature scans in the year 2000 no value for κ can be extracted. It was not possible to cool the cell down to temperatures around 38 K as in the years before. It is not totally clear what the cause of this is, maybe a higher heat load. Since in the year 2000 the HERA positron beam was never severely lost in the target region of the HERMES experiment, this method for deriving κ can also not be applied.

The only significant change in α^{TGA} was seen after an accidental power-off on one of the first days of the HERA shutdown. The power-off caused the cooling and pumping in the whole target region to stop abruptly, resulting in an increase of the target cell temperature. Since the cell had been warmed up to about 200 K, the adsorbed water layer on the cell surface was probably removed. After the cell was cooled down again, a temperature scan was performed. The cell recovered extremely fast, so that α^{TGA} changed at every temperature step, giving the scan the character of a beam dump (Fig. 4.10). For the analysis of each temperature step as a beam

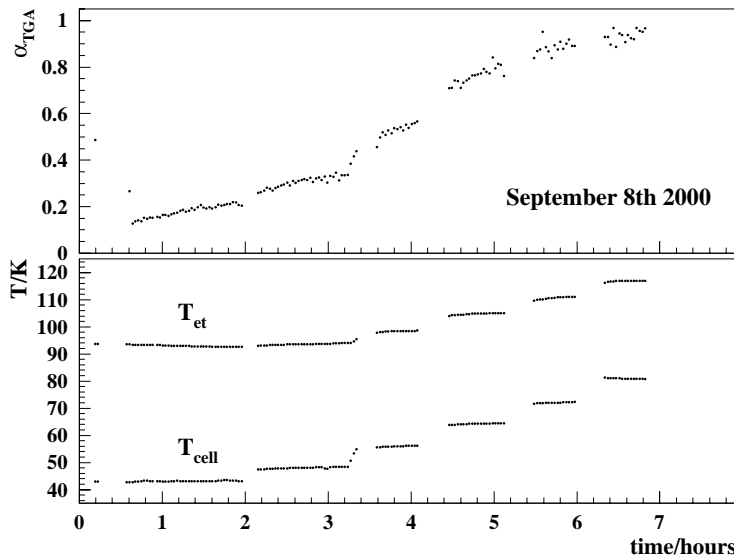


Figure 4.10:

The scan of September 8th, 2000 showing a rise in α^{TGA} at each step with constant cell temperature. This scan is a mixture of a temperature scan and a beam dump.

dump, not enough data is available and the change in α^{TGA} is not significant enough. Therefore this scan was analyzed similar to a temperature scan, but not averaging the data of each temperature step. The temperature correction function was applied for every data point. The slope of a linear function fitted to the data points in the upper plot of figure 4.11 is $m = -0.8629 \pm 0.0033$ resulting in a κ_2 of:

$$\kappa_2 = 0.8194 \pm 0.031 \quad . \quad (4.15)$$

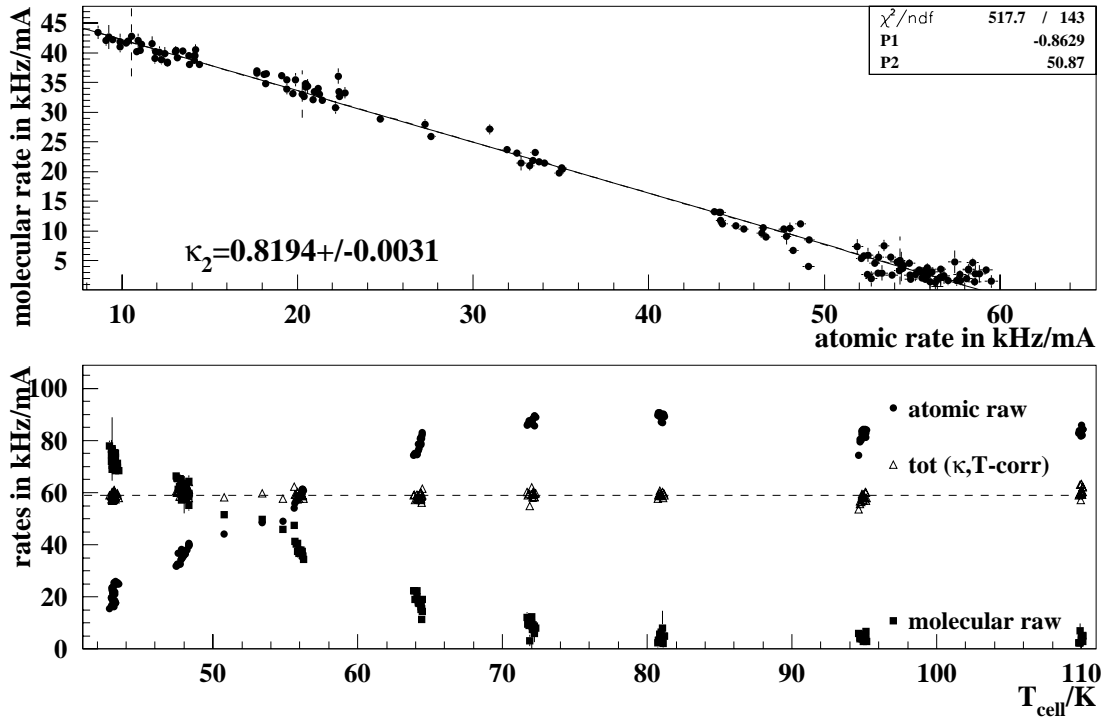


Figure 4.11:

The analysis of the scan on September 8th, 2000. This plot shows the (unaveraged) data similar to figure 4.6. From the linear fit to the data in the upper plot the κ can be calculated. This value is then used to correct the temperature corrected total count rate resulting in a constant (dashed line).

Even though this is not a usual temperature scan, the values obtained for κ_2 from this scan fits to the results from other scans (Fig. 4.12).

4.5 Results

The temperature scans and beam dumps from July 1998 until September 2000 for the deuterium running period have been analyzed. Characteristic plots for these scans can be found in appendix A.1 and appendix A.2 together with the fits for a corresponding κ_i . A list of all the extracted values of κ_i for the different injection modes (i state injection) and the averaged values κ_{avg} are found in a table in appendix A.3.

The injection of a new positron beam causes the temperature of the cell to rise. This can be seen for some of the temperature scans presented in appendix A.1. In those cases only the data points either before or after the injection can be used to extract κ .

For some of the temperature scans a big gap between the temperature of the cell and of the extension tube is seen. In some periods the temperature of the extension tube does not at all follow changes of the cell temperature. Temperature scans in these periods have been excluded from the total averaged value κ_{tot} . A beam dump in September 1999 damaged the cell by burning a hole in the aluminum storage cell wall. It is hard to describe how this affects the conductances in the cell so that this beam dump did not contribute to the mean value κ_{tot} . The scan performed after this damage of the cell was done after the installation of a new cell.

The definition of κ (eq. (4.7)) shows that the relative sensitivity of the TGA to detect atoms or molecules can vary, e.g. for different settings of the TGA ion-optics or if different channeltrons were used. In the time period July 1998 until September 2000 the same channeltron was used and the settings of the TGA ion-optics were quite constant only varying in the period September 3rd, 1999 until October 10th, 1999. In this period κ definitely changed but no reliably scan is available to extract κ . Even in periods where the ion-optics seemed stable it is possible that the relative detection sensitivity changed. For a clean calibration temperature scans would have to be done every few days and explicitly when parameters in the TGA or in the cell are changed. But unfortunately this was not done for the deuterium running period.

The values κ_{avg} (being the average of κ_2 and κ_3 of a certain scan) from the scans that were not excluded are plotted in figure 4.12. The open circles show the averaged

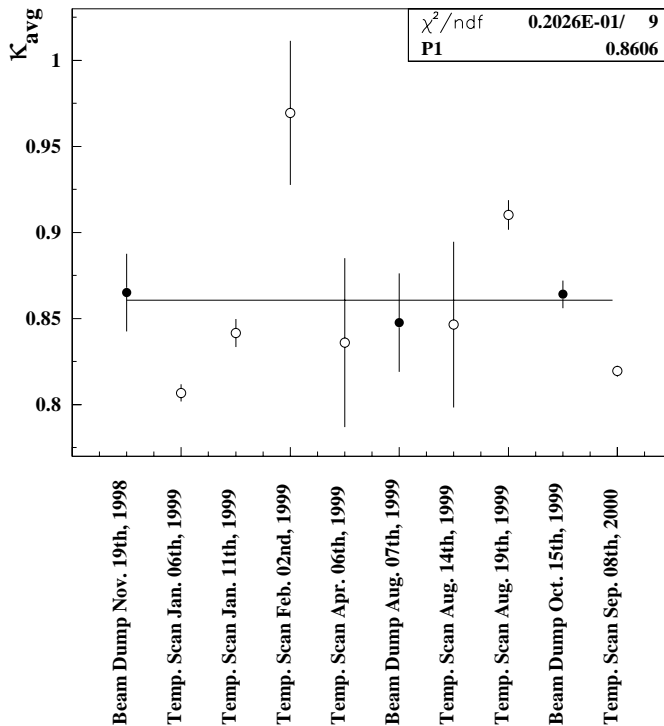


Figure 4.12:

Results for κ_{avg} plotted chronologically, open circles are obtained from temperature scans, filled circles from beam dumps. A constant is fitted to the averaged κ_{avg} values resulting in a mean κ_{tot} of $\kappa_{tot} = 0.8606 \pm 0.0814$

results from the temperature scans, the filled circles show the κ_{avg} extracted from

beam dumps. The values κ_{avg} from the two different calibration methods show good agreement. Since the fluctuation of the extracted κ_{avg} values is small it seems to be favourable to use a mean value κ_{tot} for further analysis in the determination of α_0 and α_r in this period.

The mean κ for the complete deuterium running period is given by:

$$\kappa_{tot} = 0.8606 \pm 0.0814 , \quad (4.16)$$

where κ_{tot} is the arithmetic average and the error given is half of the maximum variation of the κ_{avg} values. The error on the single κ_{avg} values is the error from the measured count rates. This error does not account for possible cross talk of the magnetic fields of the different randomly changed transisions of the Breit-Rabi polarimeter, which are not averaged out in these short measurements.

Chapter 5

Optimization of the BRP Magnet System

The Breit-Rabi polarimeter (BRP) measures the relative occupation numbers of the different hyperfine states of an atomic beam from which the atomic polarization P_a is calculated. With this value and α_0 and α_r derived from measurements with the target gas analyzer the polarization in the storage cell P^T can be evaluated.

As already described in section 3.4, the BRP consists of radio frequency transition (RFT) units, a sextupole magnet system and a detector. This chapter will focus on the magnet system, showing that the former magnet system of the BRP needed optimization.

5.1 Permanent Sextupole Magnets

Permanent magnets for the use in small vacuum chambers have advantages compared to electromagnets: high field strengths can be obtained, the magnets are compact and they are easy to handle since they do not need to be cooled and also do not need electricity.

5.1.1 General Description

The magnets used in the BRP are segmented permanent magnets consisting of 24 segments, magnetized along different directions (figure 5.1). This results in six so-called pole tips of alternating field direction. The magnets are made from rare earth permanent magnetic materials called Vacodym (reg. trademark of Vacuumschmelze, Hanau, Germany), based on neodymium-iron-boron (NdFeB) alloys. Since these

materials have a high resistance against demagnetization, they allow the design of compact, purely permanent magnetic sextupoles with high pole tip fields up to $B_{pt} = 1.6$ T [Va00]. The magnets are encapsulated in vacuum tight stainless steel containment vessels [Sc91].

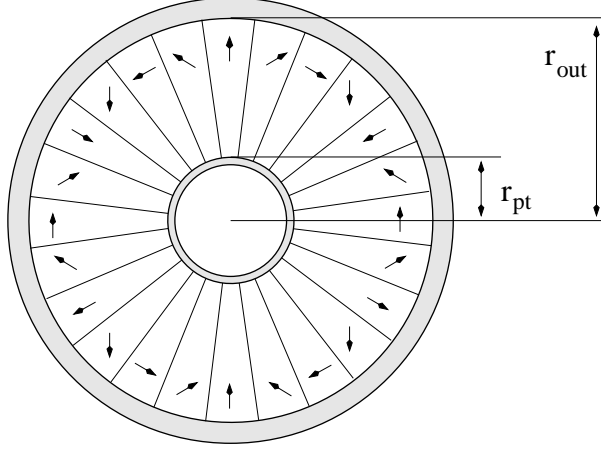


Figure 5.1:

View perpendicular to the axis of a sextupole magnet showing the 24 segments of varying magnetization direction for a magnet with an inner radius r_{pt} and an outer radius r_{out} . The magnet is encapsulated in a stainless steel can for protection having a thickness of only 0.2 mm on the inside of the magnet.

For segmented sextupole magnets the magnetic field strength perpendicular to the axis at radius r smaller or equal to the inner radius of the magnet r_{pt} can be approximated with the formula of Halbach [Hal80]:

$$|B(\vec{r})| = \frac{3}{2} J \frac{r^2}{r_{pt}^2} \left(1 - \frac{r_{pt}^2}{r_{out}^2} \right) \frac{\sin\left(\frac{4\pi\epsilon}{M}\right)}{\frac{4\pi}{M}}, \quad (5.1)$$

where J is the magnetization of the material, M is the number of segments and ϵ is a volume filling factor.

Due to their harmonic focusing fields sextupole magnets are most commonly used for Stern-Gerlach spin separation of atomic hydrogen or deuterium beams. Two sextupole magnets are used in the BRP of the HERMES experiment. They both have an inner radius of $r_{pt} = 12.5$ mm, an outer radius of $r_{out} = 40$ mm and a pole tip field strength of $B_{pt} = 1.45$ T. The magnet installed after the RFT units has a length of $l_1 = 70$ mm, the second magnet has a length of $l_2 = 110$ mm.

5.1.2 Atomic States in Sextupole Magnets

In this section the equations for a sextupole magnet are given in cartesian coordinates since the Monte Carlo simulation used to optimize the BRP magnet system calculates in cartesian coordinates. The z-axis is the axis of the sextupole magnet. A force acts on a atom in the magnet:

$$\vec{F}(x, y) = -\vec{\nabla} E = -\frac{\partial E}{\partial B} \cdot \vec{\nabla} |\vec{B}(x, y)| = -\mu_{eff}(B) 2 \frac{B_{pt}}{r_{pt}^2} \begin{pmatrix} x \\ y \end{pmatrix}. \quad (5.2)$$

The equation of motion for an uncharged atom is then:

$$m \begin{pmatrix} \ddot{x} \\ \ddot{y} \end{pmatrix} = - \mu_{eff}(B) 2 \frac{B_{pt}}{r_{pt}^2} \begin{pmatrix} x \\ y \end{pmatrix}, \quad (5.3)$$

which is decoupled from the motion in the z-direction following:

$$m \cdot \ddot{z} = 0. \quad (5.4)$$

The velocity in z-direction, i.e. along the axis of the sextupole magnet v_z is constant.

The effective magnetic moment μ_{eff} has been calculated for the different hyperfine states for hydrogen (eq. (2.28)) and deuterium (eq. (2.30)) atoms in chapter 2. The μ_{eff} of the mixed hyperfine states is dependent on the magnetic field strength at the radial position

$$r = \sqrt{x^2 + y^2} \quad (5.5)$$

of the atom in the sextupole magnet.

For high magnetic fields ($B \gg B_c$)

$$\mu_{eff} \approx \pm \mu_B \quad (5.6)$$

for all states of hydrogen and deuterium with the sign depending only on the sign of m_S . It can be derived from eq. (5.3) [St94b, St92] that atoms in a hyperfine state with $m_S = +\frac{1}{2}$ oscillate along the radial direction while proceeding along the z-direction with constant velocity v_z with a wavelength of:

$$\lambda = v_z T = 2\pi v_z \frac{1}{\omega} = 2\pi v_z \sqrt{\frac{m r_{pt}^2}{2 \mu_B B_{pt}}}. \quad (5.7)$$

Atoms in a hyperfine state with $m_S = -\frac{1}{2}$ have an increase in their radial position according to a sinh function while proceeding along the z-direction, i.e. they are defocused out of the magnet.

5.1.3 Short Sextupole Magnets and Optical Lenses

In short but strong sextupole magnets atoms with similar entrance velocities are defracted analogous to a beam of light in a thin optical lens.

For sextupole magnets with high pole tip fields the equation (5.6) is a valid approximation. An atom with the projection of the electron spin $m_S = +\frac{1}{2}$ entering such a magnet at a distance r_{init} from the magnet axis and its velocity parallel to the axis is subject to a force according to equation (5.2):

$$\vec{F}(r_{init}) = - \mu_B 2 \frac{B_{pt}}{r_{pt}^2} \cdot r_{init}^2. \quad (5.8)$$

In a short magnet the defraction according to a sinus function can be approximated by a path on a circular arc with the centripetal force:

$$\vec{F}_{cen} = \frac{m v^2}{r_{circ}} = \mu_B 2 \frac{B_{pt}}{r_{pt}^2} \cdot r_{init}^2 \quad (5.9)$$

and a radius of

$$r_{circ} = \frac{m v^2}{\mu_B 2 \cdot r_{init}^2} \frac{r_{pt}^2}{B_{pt}} . \quad (5.10)$$

A scheme of this is drawn in figure 5.2, showing the upper half of a cut along the

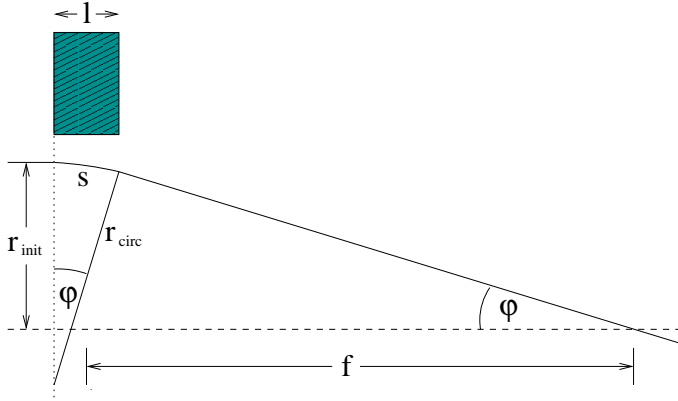


Figure 5.2:

The path of an atom ($m_S = +\frac{1}{2}$) in a strong sextupole magnet can be approximated by a circular arc s . The scheme shows a cut along the axis of the short sextupole magnet. Only the upper half from the magnet axis to the pole tip of the magnet is drawn.

axis of the short sextupole magnet. An atom entering the magnet in a distance r_{init} from the magnet axis is defracted along a circular arc s and continues its path along the tangent to the circle with radius r_{circ} until it crosses the magnet axis at a distance f from the center of the magnet.

The angle of defraction φ can be approximated for short magnets:

$$\varphi = \frac{s}{r_{circ}} \approx \frac{l}{r_{circ}} = \frac{l}{m v^2} \mu_B 2 \frac{B_{pt}}{r_{pt}^2} \cdot r_{init}^2 . \quad (5.11)$$

Since the defraction angle can also be expressed as:

$$\varphi = \frac{r_{init}}{f} , \quad (5.12)$$

resulting in:

$$f = \frac{m v^2 r_{pt}^2}{\mu_B 2 B_{pt} l} . \quad (5.13)$$

The distance where the atom crosses the axis of the magnet does not depend on the entrance distance r_{init} . Therefore f is the focal length of the magnet analogous to a thin optical lens. In a system of two short strong sextupole magnets the first magnet has the property of focusing diverging atoms with similar entrance velocities on parallel paths, the second magnet focuses them to the axis at the distance f . Such a system is installed in the Breit-Rabi polarimeter of the HERMES experiment.

The average velocity of a thermalized hydrogen beam v^H compared to a beam of thermalized deuterium (eq. (4.8)) is:

$$v^H = \sqrt{2} \cdot v^D . \quad (5.14)$$

Since the mass of a deuterium atom m^D is twice the mass of a hydrogen atom m^H :

$$\frac{m^H (v^H)^2}{m^D (v^D)^2} = 1 , \quad (5.15)$$

so that the focal length (eq. (5.13)) is the same for thermalized hydrogen and deuterium atoms. A magnet system of short sextupole magnets with high pole tip fields optimized for hydrogen will then show the same behaviour for deuterium.

5.2 Monte Carlo Simulation

A Monte Carlo simulation has been written by Christian Baumgarten [Ba00] to simulate the transmission of the different hyperfine states of hydrogen or deuterium atoms through the sextupole magnets of the Breit-Rabi polarimeter of the HERMES experiment.

5.2.1 Description

The Monte Carlo simulation is a computer program written in the C-language. It does not use a random start generator but systematically scans through all the possible trajectories from the beginning of the sample tube to the entrance of the first sextupole magnet of the BRP. A scheme of this is given in figure 5.3. After the

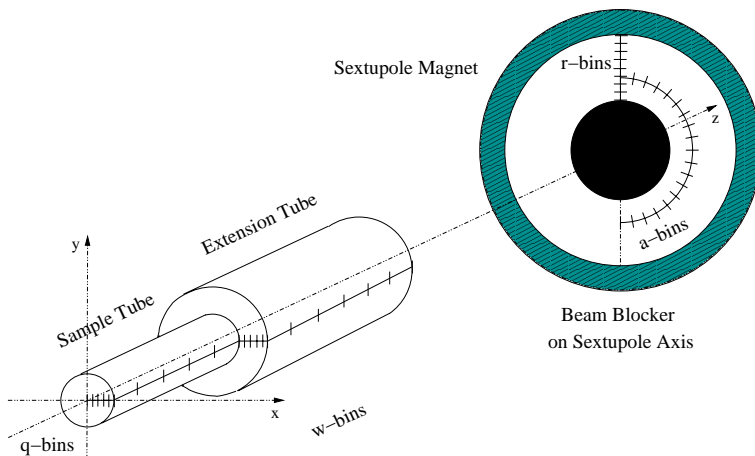


Figure 5.3:

Scheme of the various bins used for the definition of different possible paths of an atom until the beginning of the BRP magnet system. The axes are not drawn to scale, especially the z-axis is crunched.

last wall bounce the atom travels on a straight path to the beginning of the magnet

system where it has to have a radius bigger than the radius of the beam blocker, but smaller than the pole tip radius of the magnet (resulting in a ring). In the Monte Carlo simulation such a path (vector) is defined as an endpoint on the ring minus the point of the last wallbounce. To simplify this bins are introduced reducing the number of possible paths. Therefore the start position of an atom is defined by a number referring to the quadrant of the x-y plane (so-called q-bins) and a number referring to the position on the first quadrant of the x-z plane (so-called w-bins). The w-bins are divided in four different parts of equidistant bins: the atom can have its last wall bounce either in the cell, on the sample tube, on the intersection plane between sample and extension tube or on the extension tube. The position of the atom on the ring is also described by two numbers, one referring to the radial bin (so-called r-bins) the other to the angular bin (so-called a-bins) as shown in figure 5.3. The angular bins only cover half of the ring since scanning over the other half would just result in paths mirrored on the y-z plane.

In the sextupole magnet the atom is defracted off its straight path. The equations of motion are given by the equations (5.3) and (5.4), where the μ_{eff} is given by the equations (2.28) for hydrogen and (2.30) for deuterium. The equation (5.3) is a differential equation of second order and can be split in two differential equations of first order:

$$\begin{pmatrix} \frac{dx}{dt} \\ \frac{dy}{dt} \end{pmatrix} = \begin{pmatrix} v_x \\ v_y \end{pmatrix}, \quad (5.16)$$

$$\begin{pmatrix} \frac{dv_x}{dt} \\ \frac{dv_y}{dt} \end{pmatrix} = - \frac{\mu_i^{H,D}}{m^{H,D}} 2 \frac{B_{pt}}{r_{pt}^2} \begin{pmatrix} x \\ y \end{pmatrix}, \quad (5.17)$$

where H, D refers to hydrogen or deuterium respectively in the hyperfine state $|i\rangle$. In the Monte Carlo simulation the solutions to the equations (5.16) and (5.17) as a function of the time is approximated by taylor expansion for small dz steps with $DT = \frac{dz}{v_z}$:

$$\begin{pmatrix} \frac{dv_x(t_0)}{dt} \\ \frac{dv_y(t_0)}{dt} \end{pmatrix} = - \frac{\mu_i^{H,D}}{m^{H,D}} 2 \frac{B_{pt}}{r_{pt}^2} \begin{pmatrix} x(t_0) \\ y(t_0) \end{pmatrix}, \quad (5.18)$$

$$\begin{pmatrix} x(t_1) \\ y(t_1) \\ z(t_1) \end{pmatrix} = \begin{pmatrix} x(t_0) \\ y(t_0) \\ z(t_0) \end{pmatrix} + \begin{pmatrix} v_x(t_0) DT \\ v_y(t_0) DT \\ dz \end{pmatrix}, \quad (5.19)$$

$$\begin{pmatrix} v_x(t_1) \\ v_y(t_1) \end{pmatrix} = \begin{pmatrix} v_x(t_0) \\ v_y(t_0) \end{pmatrix} + \begin{pmatrix} \frac{dv_x(t_0)}{dt} \\ \frac{dv_y(t_0)}{dt} \end{pmatrix} \cdot DT. \quad (5.20)$$

The Monte Carlo simulation calculates the vectors

$$\begin{pmatrix} x(t_i) \\ y(t_i) \\ z(t_i) \end{pmatrix}, \quad \begin{pmatrix} v_x(t_i) \\ v_y(t_i) \end{pmatrix}, \quad \begin{pmatrix} \frac{dv_x(t_i)}{dt} \\ \frac{dv_y(t_i)}{dt} \end{pmatrix}, \quad (5.21)$$

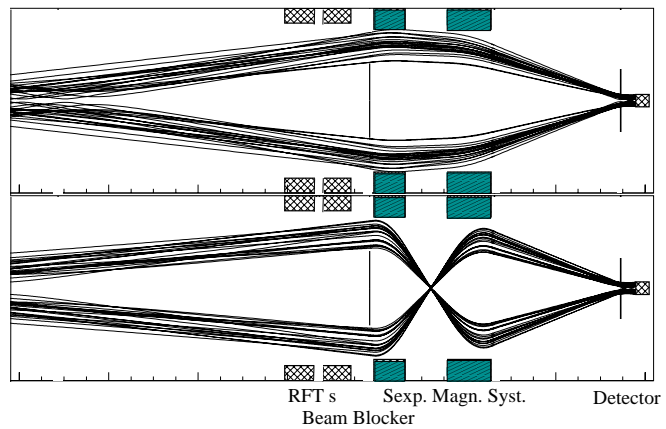
for t_i and then advances one step $DT = \frac{dz}{v_z}$. The simulation loops over the equations (5.18), (5.19) and (5.20) as long as the z-position of the atom is inside the magnet.

Between the two magnets of the BRP no force is assumed to act on the atom, i.e. no stray fields of the magnets, so that the atom continues on a straight path. The defraction in the second magnet is simulated analogous to the first magnet. Then again a straight path is assumed until the entrance of the detector.

The velocity v is then varied for every possible starting trajectory and a v_{min} and v_{max} are then found. This means the atom in the hyperfine state $m_S = +\frac{1}{2}$ has to have a velocity v with $v_{min} \leq v \leq v_{max}$ in order to be detected. For some starting trajectories two different velocity intervalls can be found (Fig. 5.4). The upper plot

Figure 5.4:

Two magnets result in two different kinds of trajectories, meaning atoms from two different velocity intervalls can be transmitted. This picture was produced by a Monte Carlo simulation of C. Großhauser [Gr98].



in figure 5.4 shows the transmission of fast atoms with $m_S = +\frac{1}{2}$, the lower plot shows that slow atoms which are overfocused in the first magnet can still reach the detector.

The output file of the Monte Carlo is then a list of all the bin combinations, i.e. all possible starting trajectories and the velocity intervalls resulting in transmission. The Monte Carlo program then calculates the transmission over the velocity weighting the starting trajectories by $\cos \varphi$ distributions as shown in the left plot of figure 5.5 for two different possible trajectories and also weighting them by the pressure distribution in the sample and extension tube shown qualitatively in the right plot of figure 5.5. This resulting transmission simulated by the Monte Carlo is called the *geometrical transmission*. which is only the probability of transmission of

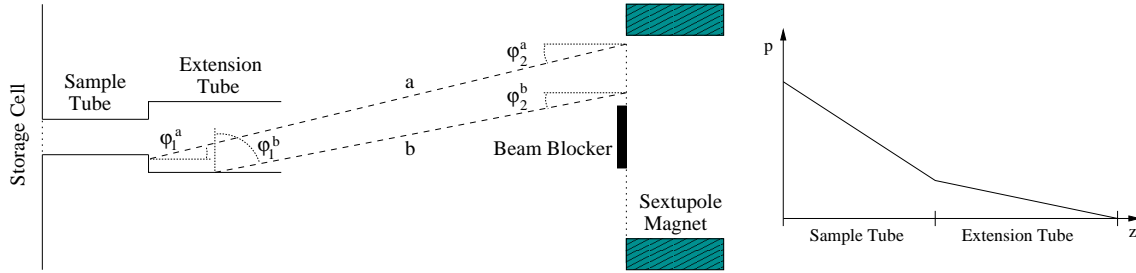


Figure 5.5:

The weighting of two different trajectories is shown in the left plot (not drawn to scale); the right plot shows qualitatively the pressure distribution in the sample and extension tube.

an atom with a certain velocity according to the geometry of the BRP. This has then to be weighted by the actual velocity distribution for a beam of thermalized atoms, i.e. weighting the geometrical transmission by a Maxwell distribution resulting in the transmission of the magnet system expected by the Monte Carlo simulation called the *resulting transmission*.

5.2.2 Result for the Former Magnet System

A Monte Carlo simulation was done for the so-called former magnet system of the BRP. This magnet system was employed in the BRP until the end of the 2000 running period of HERMES in September 2000. The characteristic parameters of this magnet system as given in section 5.1.1 were used in the Monte Carlo program. The simulation showed that the hyperfine states with $m_S = -\frac{1}{2}$ are totally deflected as desired for hydrogen as well as for deuterium. The geometrical transmission of the state $|1\rangle$ for hydrogen is shown in figure 5.6. Two peaks from the two different velocity intervals of transmitted particles can be seen.

As already mentioned in the previous section, the geometrical transmission has to be weighted by the Maxwell distribution for a certain cell temperature. This has been done in figure 5.7 for deuterium.

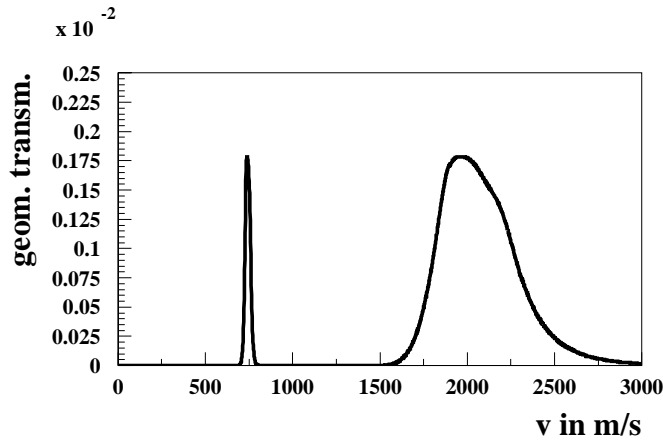


Figure 5.6:
Monte Carlo result for hydrogen atoms for the former magnet system of the BRP.

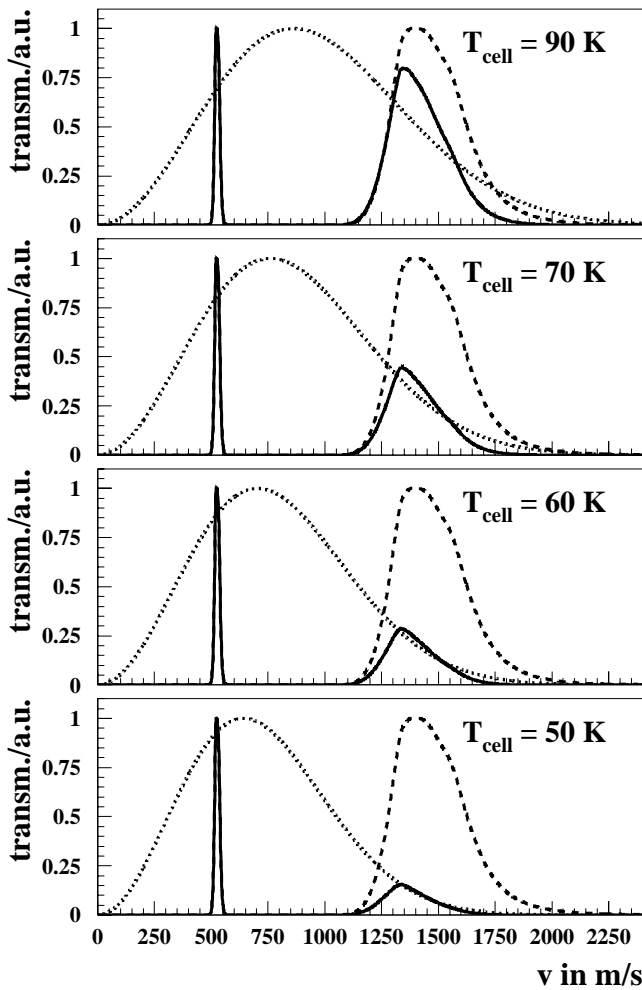


Figure 5.7:
Monte Carlo result for deuterium weighted by the Maxwell distribution for the former magnet system for four different cell temperatures. The dashed line is the geometrical transmission simulated by the Monte Carlo, the dotted curve is the Maxwell distribution and the solid line is then the resulting transmission.

Comparing figure 5.6 with the top plot of figure 5.7 shows that the geometrical transmission for hydrogen and deuterium has the same shape, only having the velocity peaks at different positions. The resulting transmission for low temperatures is not high since the peak of the Maxwell distribution moves down to lower temperatures. The resulting transmission over the temperature of the cell is plotted in figure 5.8. It

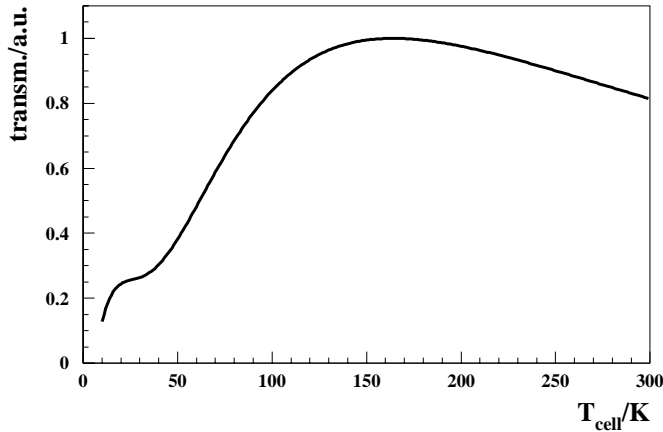


Figure 5.8:

The simulated resulting transmission of the former magnet system as a function of the cell temperature.

can be seen that this magnet system was optimized for temperatures around 150 K. The actual working point for hydrogen was about 95 K, for deuterium 65 K. A new magnet system for lower temperatures was to be found with the help of the Monte Carlo simulation.

5.2.3 Simulations of Various Magnet Systems

As it was seen in figure 5.7 the velocities of the geometrical transmission are too high so that the resulting transmission is too small for low temperatures. The new magnet system of the BRP should therefore transmit particles with smaller velocities. This can be achieved by shortening the magnets or by varying the pole tip fields of the magnets. Enlarging the pole tip radius of the magnets would result in the transmission of slower atoms, but since the radius of the radio frequency transition unit before the first magnet limits the geometrical acceptance. Also a noticeable variation of the distance between the second magnet and the detector (i.e. the focal length of the second magnet) is not realizable in the current setup of the target at the HERMES experiment. Therefore the Monte Carlo simulation has been used for different choices of magnets. Some of the results are plotted in the figures 5.9, 5.10, 5.11 and 5.12 for hydrogen.

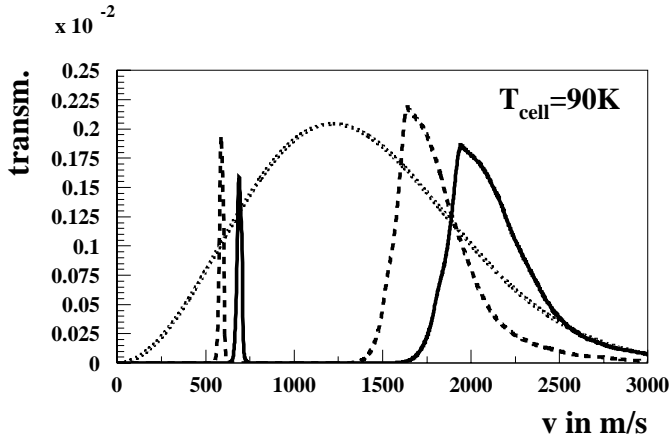


Figure 5.9:

Monte Carlo results for hydrogen for two different systems of magnets with smaller pole tip fields. The peaks of the velocity windows (geometrical transmission) move to lower velocities.

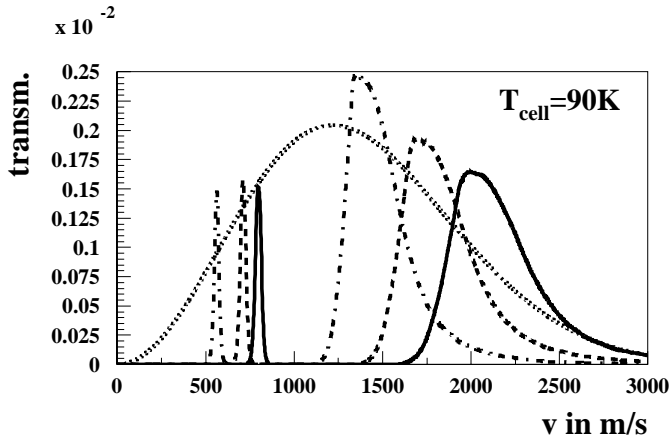


Figure 5.10:

Monte Carlo results for hydrogen for three different systems of magnets where both magnets were shortened. The peaks of the velocity windows (geometrical transmission) move to lower velocities and become more narrow.

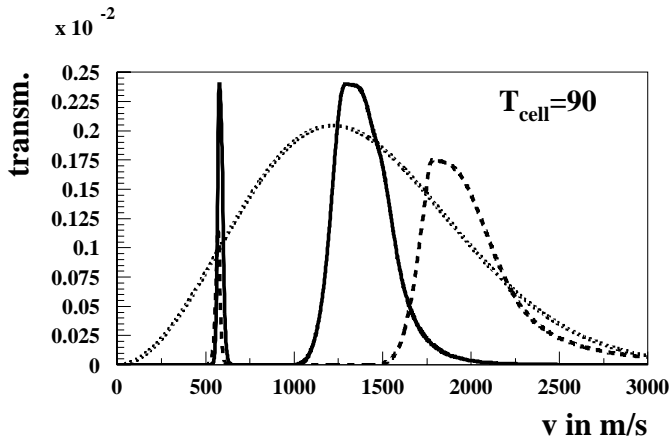


Figure 5.11:

Monte Carlo results for hydrogen for two different systems of magnets. The magnets used are shorter and have smaller pole tip fields. The peaks of the velocity windows (geometrical transmission) move to lower velocities.

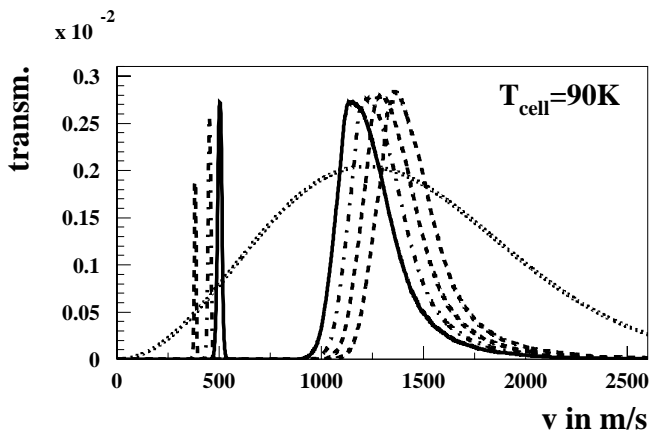


Figure 5.12:

Monte Carlo results for hydrogen for four different spacings of two short sextupole magnets. The first one has a length of 3 cm, the second one of 4 cm. The peaks of the velocity windows (geometrical transmission) move to lower velocities for bigger distances.

The figure 5.12 shows results from simulations done with magnets that are available for the installation in the BRP at HERMES. The magnets used in the simulation have lengths of 3 cm and 4 cm and a pole tip field of 1.45 T. The peak of a Maxwell distribution at 90 K is about at the same position as the peak of the geometrical transmission.

5.2.4 Simulations with the New Magnet System

A system composed of two sextupole magnets with lengths of 3 cm and 4 cm has favourable properties for the BRP and will from now on be the so-called *new* magnet system. The highest transmission is achieved for a maximum possible distance in the BRP of 18.6 cm.

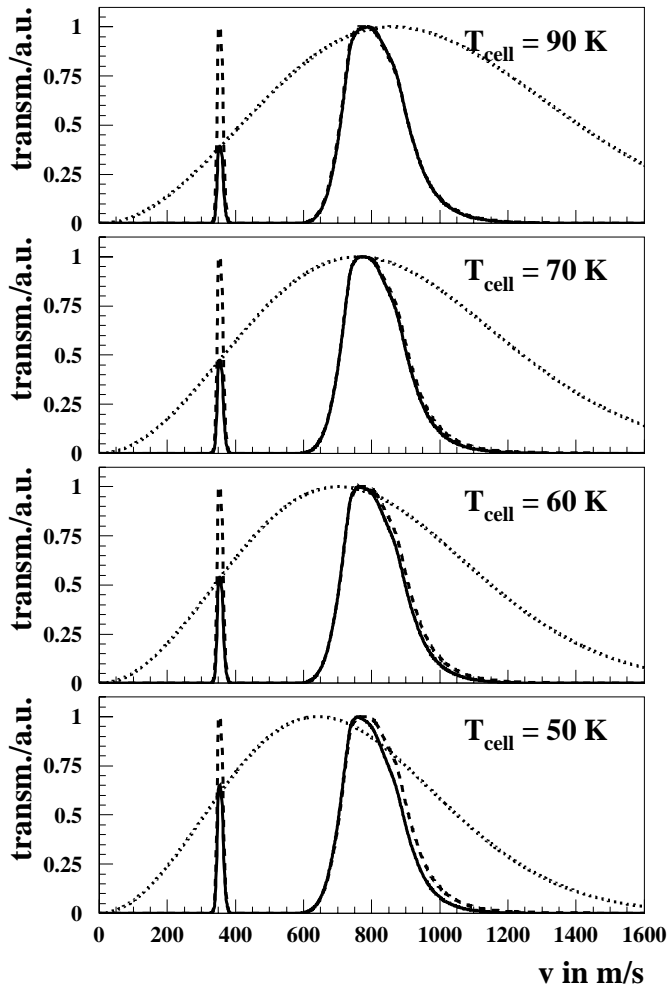


Figure 5.13:

Monte Carlo result for deuterium weighted by the Maxwell distribution for the new magnet system for four different temperatures. The dashed line is the geometrical transmission simulated by the Monte Carlo program, the dotted curve is the Maxwell distribution and the solid line is then the resulting transmission. The resulting transmission stays high even at low temperatures of 50 K.

Even at temperatures of 50 K the system still has a high resulting transmission (Fig. 5.13). A comparison of the resulting transmission over the temperature for

the so-called former magnet system and the so-called new magnet system is shown in figure 5.14. The simulations resulting in the left plot were done for deuterium,

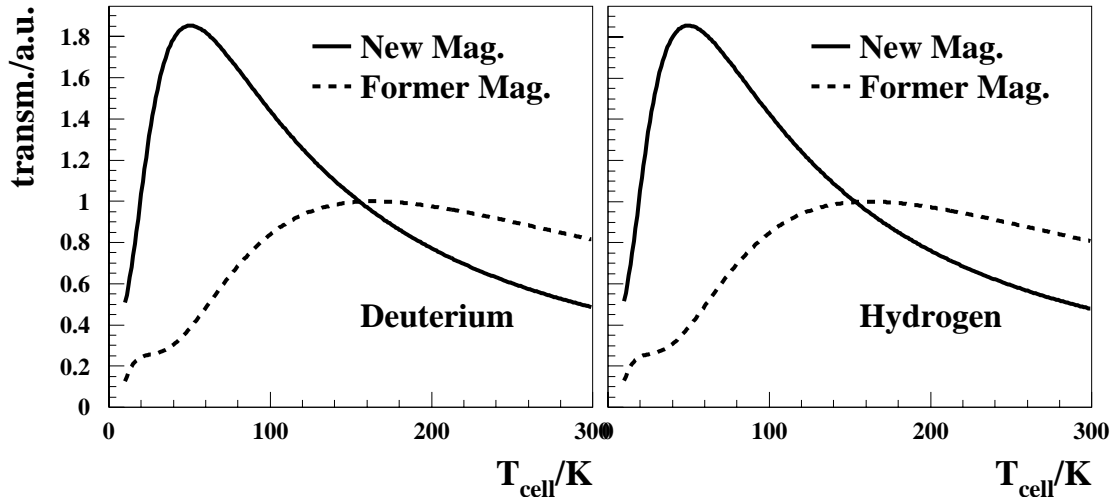


Figure 5.14:

Comparison of the Monte Carlo results for hydrogen (right plot) and deuterium (left plot) plotted over the temperature.

the results for hydrogen are plotted on the right side. As expected very similar behavior for the transmission of hydrogen and deuterium is seen. The transmission with the new magnet system is higher than with the former magnets, especially at low temperatures. The temperature given in the plot is not exactly the temperature of the cell. It is rather the average temperature of the detected atoms. A Monte Carlo simulation from M. Henoeh [Hen98] showed that for a large cell only about 50% of the detected atoms have their last wallbounce in the cell, about 12% in the extension tube, the rest in the sample tube or on the intersection plane between the sample and extension tube. Since the temperature of the extension tube is definitely higher than the temperature of the cell, the actual performance of the magnet systems is shifted to lower temperatures. The improvement factor from the former magnet system to the new system is then lower than it appears in figure 5.14. Due to the unknown thermal contact of the extension tube an exact value of the actual averaged temperature of the atoms cannot be given. But it should be safe to say that the improvement factor around 100 K is about 1.6.

Since the cell is only attached on one side it can undergo thermal extension. The cell has to be alligned with the injection and sample tube for a certain temperature. An extremely large shift of 2 mm of the cell in the downstream direction (y -direction) due to thermal extension has been simulated for the former and the new magnet system (Fig. 5.15). This plot is normalized to the transmission of the former magnet system without misalignment. It can be seen that the new magnet system still has

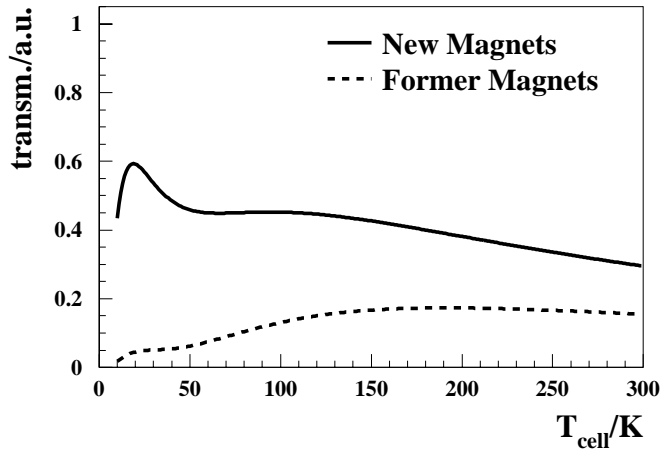


Figure 5.15:

Comparison of the Monte Carlo results for hydrogen for a shift of the cell in y -direction of 2 mm for the former and the new magnet system.

higher transmission.

The new running period of the HERMES experiment will start with a transverse target magnetic holding field. The transverse magnet has a bigger iron yoke so that the ABS as well as the BRP and TGA system have to be moved further away from the HERA beam axis. Therefore the extension tube will be extended by another 4 cm, resulting in a length of 16 cm. This will partly be compensated by shortening the distance between the last magnet and the detector. The effect of this prolongation of the extension tube by 4 cm has been simulated for the former and new magnet system (Fig. 5.16) and again the new system behaves favourably. This sextupole magnet system was installed in the BRP for the upcoming running period (starting July 2001).

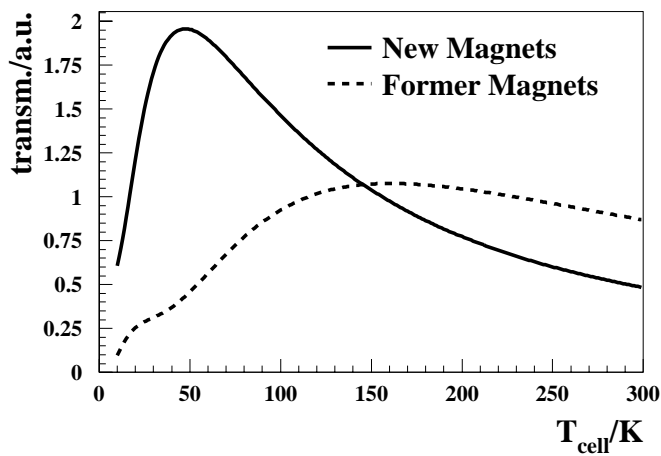


Figure 5.16:

Comparison of the Monte Carlo results for hydrogen for an extended extension tube of 4 cm for the former and the new magnet system.

5.3 Time of Flight Measurements

Measurements of the velocity distribution of atoms detected by the Breit-Rabi polarimeter have been performed for both the former and the new magnet system for deuterium by means of time of flight measurements.

5.3.1 Description

By measuring the time of flight the velocity distribution of atoms can be found, i.e. the time the atoms in one hyperfine state need to pass the magnet system is measured. These measurements were performed for the hyperfine state $| 1 \rangle$ and $| 3 \rangle$.

The ABS was set to inject deuterium atoms in the hyperfine states $| 3 \rangle$ and $| 4 \rangle$ into the storage cell. The chopper of the BRP was stopped in the open position. Then the radio frequency transition unit SFT in the BRP was set to exchange the populations of the hyperfine states $| 3 \rangle$ and $| 5 \rangle$ so that no state is transmitted through the magnet system of the BRP. The radio frequency of the transition unit MFT before the magnet system is then pulsed by a pulser with a frequency of 125 Hz. This results in the transition alternately exchanging the populations of the states $| 3 \rangle$ and $| 4 \rangle$ or not. Therefore when the transition is switched on state $| 3 \rangle$ is present in the beam which is focused by the magnet system into the detector resulting in a transmitted signal of full intensity.

The pulsed transition unit (MFT) is triggered so that the point of switching on is known. From the time difference until the atoms are detected and with the information of the distance from the end of the transition unit until the beginning of the detector the velocity of the atoms can be determined.

5.3.2 Results for the Former Magnet System

Time of flight measurements have been performed for the former magnet system at different cell temperatures with deuterium atoms. A measurement at a cell temperature of 79.2 K for state $| 3 \rangle$ is shown in figure 5.17. The MFT was continuously switched on and off with a frequency of 125 Hz. The detector software was set to collect 100 times data in 2048 bins with a binlength of 0.01 ms and then average. This was then one cycle. Such a cycle was repeated up to 900 times, every time averaging the new data with the data from the cycles before. Since the MFT unit was pulsed with a frequency of 125 Hz the 2048 bins (this is measuring 0.02048 s) correspond to 2.56 times the turning on and off of the transition. The points shown in figure 5.17 are the averaged data points over 314 cycles.

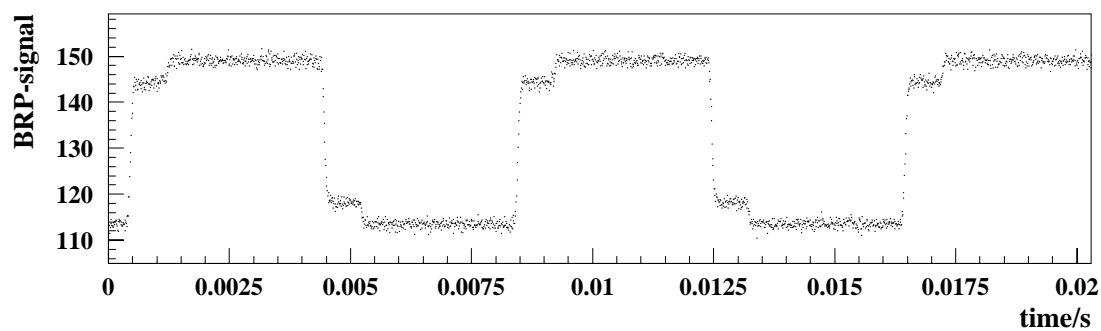


Figure 5.17: A measurement at 79.2 K with the former magnet system.

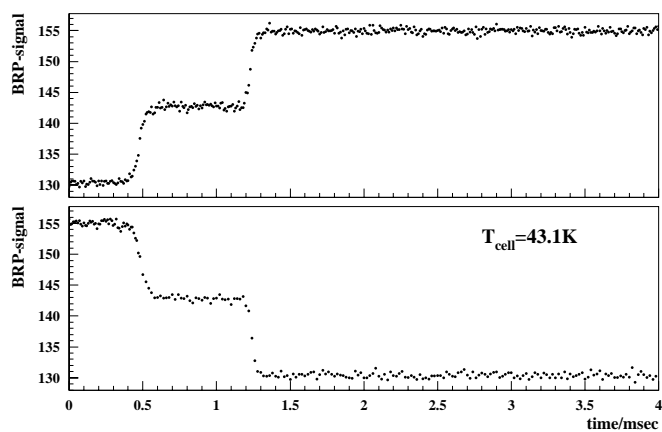


Figure 5.18:

Averaged result for state $| 3 \rangle$ from the measurement at 43.1 K with the former magnet system.

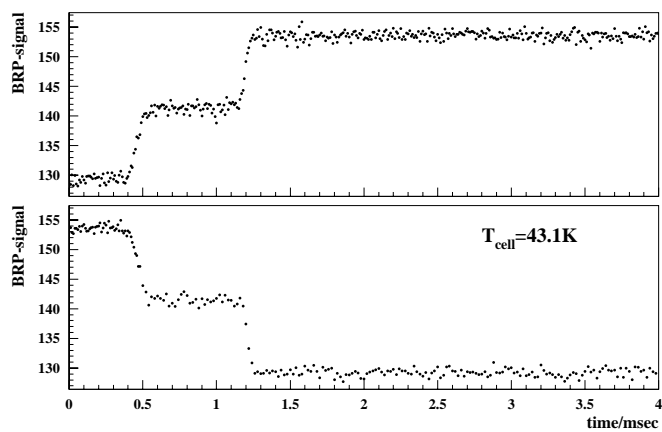


Figure 5.19:

Averaged result for state $| 1 \rangle$ from the measurement at 43.1 K with the former magnet system.

The measurement was then averaged over the three (two) times the transition unit was switched on (off) resulting in figure 5.18, this time from a measurement at 43.1 K but again for state $|3\rangle$. The measurement was cycled 712 times.

The same has been done for the measurement with state $|1\rangle$ at the same cell temperature but with 251 cycles to show that the measured transmission is the same. An agreement for the pure ($|1\rangle$) and mixed state ($|3\rangle$) can be seen. This is expected for high magnetic fields where the approximation in equation (5.6) is valid.

The averaged data points for four different cell temperature are shown in figure 5.20 for state $|3\rangle$. At the time zero the MFT was switched on. It takes some time

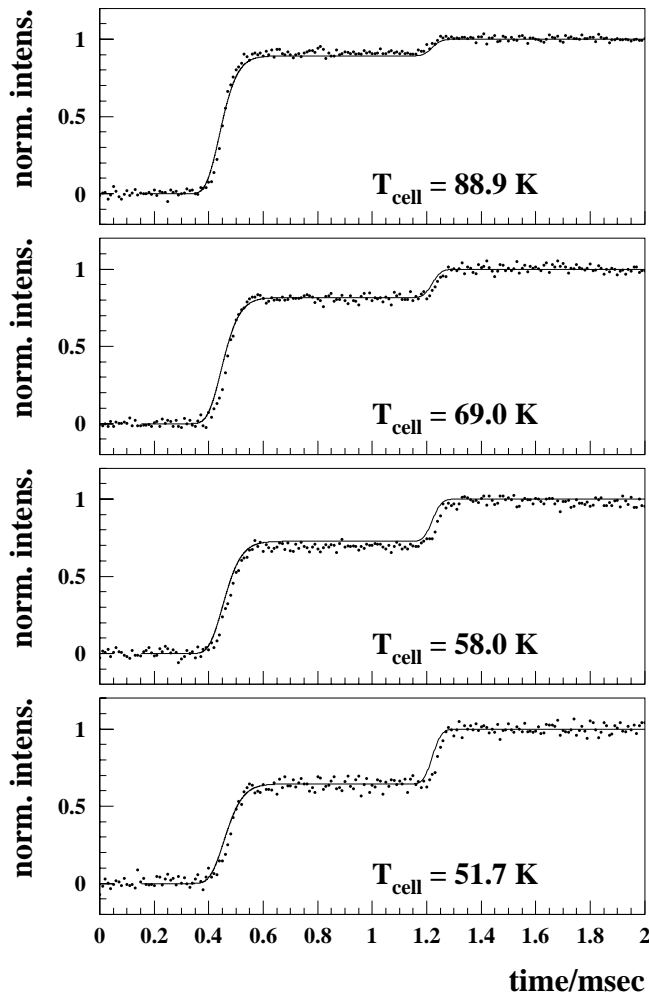


Figure 5.20:

Comparison of the measurements with the model for the former magnet system. The data points from the measurements for four different cell temperatures are shown. The solid line is the distribution over time of the geometrical transmission of a model (Fig. 5.21) weighted by a Maxwell distribution for four different temperatures.

(≈ 0.4 ms) until the first transmitted atoms reach the detector. In the time interval 0.6 ms to 1.2 ms no additional atoms are detected, at the end a second step is seen. The measurements can be interpreted as having atoms from two different velocity windows and the fast atoms are detected first, then the slow ones. For the former

magnet system it can be seen that the contribution of slow atoms increases for low temperatures, while the position of the two velocity windows stays about the same.

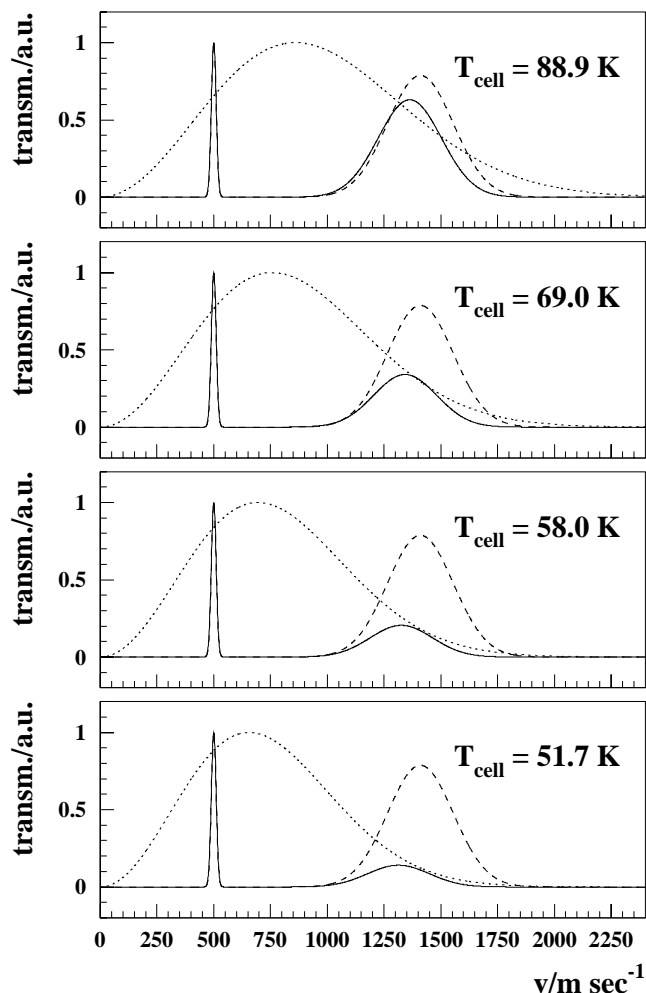


Figure 5.21:

The model used for the fit to the measurements with the former magnet system. Two Gaussians distributed around two different velocities are assumed. This geometrical transmission (dashed line) is weighted by a Maxwell distribution (dotted line) for four different temperatures giving the resulting transmission (solid line). The normalized intensity of this resulting transmission plotted over time for a path of flight of 61 cm is plotted as a solid line in figure 5.20.

A model assuming the geometrical transmission of atoms to be distributed according to a Gaussian distribution around two different velocities is introduced. This geometrical transmission has to be weighted by a Maxwell distribution as it was done for the geometrical transmission simulated by the Monte Carlo simulation. This is done for four different temperatures in figure 5.21 showing the geometrical transmission as the dashed line, the Maxwell distribution as the dotted line and the solid line represents the resulting transmission of this model. Now assuming the detector to be 61 cm away from the MFT transition the time of flight for the resulting transmitted atoms can be calculated. This is plotted as the solid line in figure 5.20 showing good agreement with the measured data points. This model (Fig. 5.21) shows good agreement with the results from the Monte Carlo simulation plotted for similar temperatures in figure 5.7.

5.3.3 Results for the New Magnet System

Time of flight measurements have also been performed after the installation of the new sextupole magnet system in the BRP. The software had the same settings as for the measurements with the former magnet system so that 2048 bins collected in 0.02048 s resulted in 2.56 times of the pulsed transition unit to be turned on and off. A measurement for state $|3\rangle$ at a cell temperature of 80.9 K is shown in figure 5.22. Figure 5.22 can be compared to figure 5.17 showing that for the turning on of the

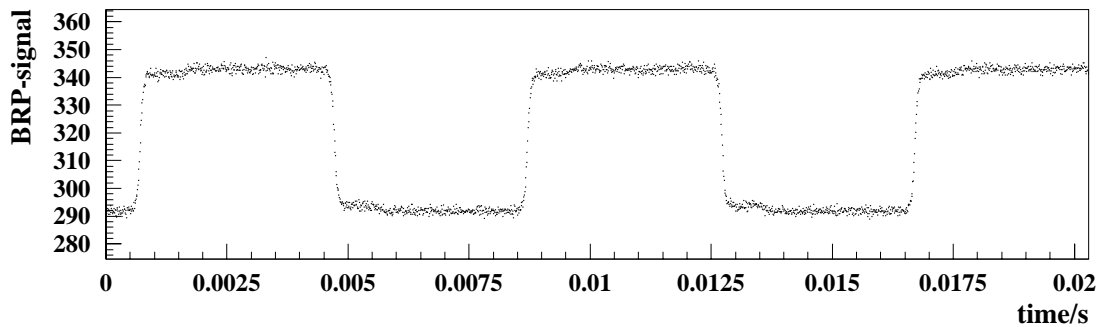


Figure 5.22: A measurement at 80.9 K with the new magnet system.

transition nearly only one step is seen.

The measurement with this magnet system was performed after the HERMES experiment was moved out of the HERA tunnel and back into the so-called parking position for the the long HERA shutdown. HERMES was not connected to the HERA cooling system so that the target had to be cooled using a helium dewar. The averaged data from a measurement at the lowest achievable temperature using

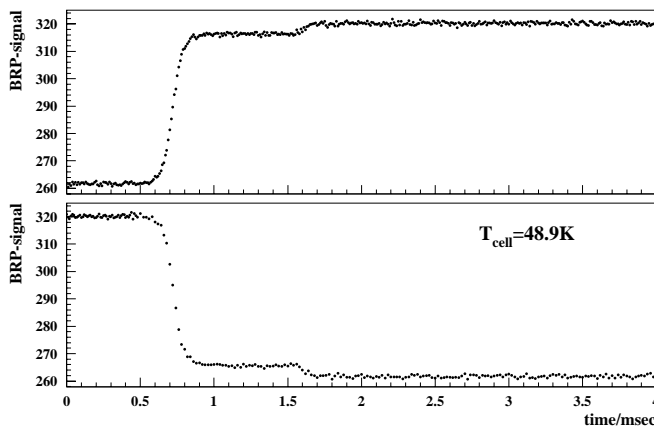


Figure 5.23:
Averaged result from the measurement at 48.9 K with the new magnet system.

the helium dewar is shown in figure 5.23. This plot can be compared to figure 5.18 showing that the new magnet system transmits atoms with lower velocities than the

former magnet system and the new system has even at low temperatures a smaller contribution from the slow velocity peak.

The averaged data points from the measurements with the new magnet system for four different cell temperatures are shown on the left side of figure 5.24 for state $|3\rangle$. As it was done in figure 5.21, it is assumed that the velocity of the atoms geometrically transmitted through the magnet system is distributed according to two Gaussians. This model weighted by a Maxwell distribution for four different temperatures is shown on the right side of figure 5.24. The resulting transmission of the model is plotted over time (the distance MFT to detector is assumed to be 61 cm) in the left side as a solid line and shows good agreement with the data points from the measurement.

Since the model also shows good agreement with the results from the Monte Carlo simulation shown in figure 5.13. Therefore the predictions given by the Monte Carlo simulation seem to be valid.

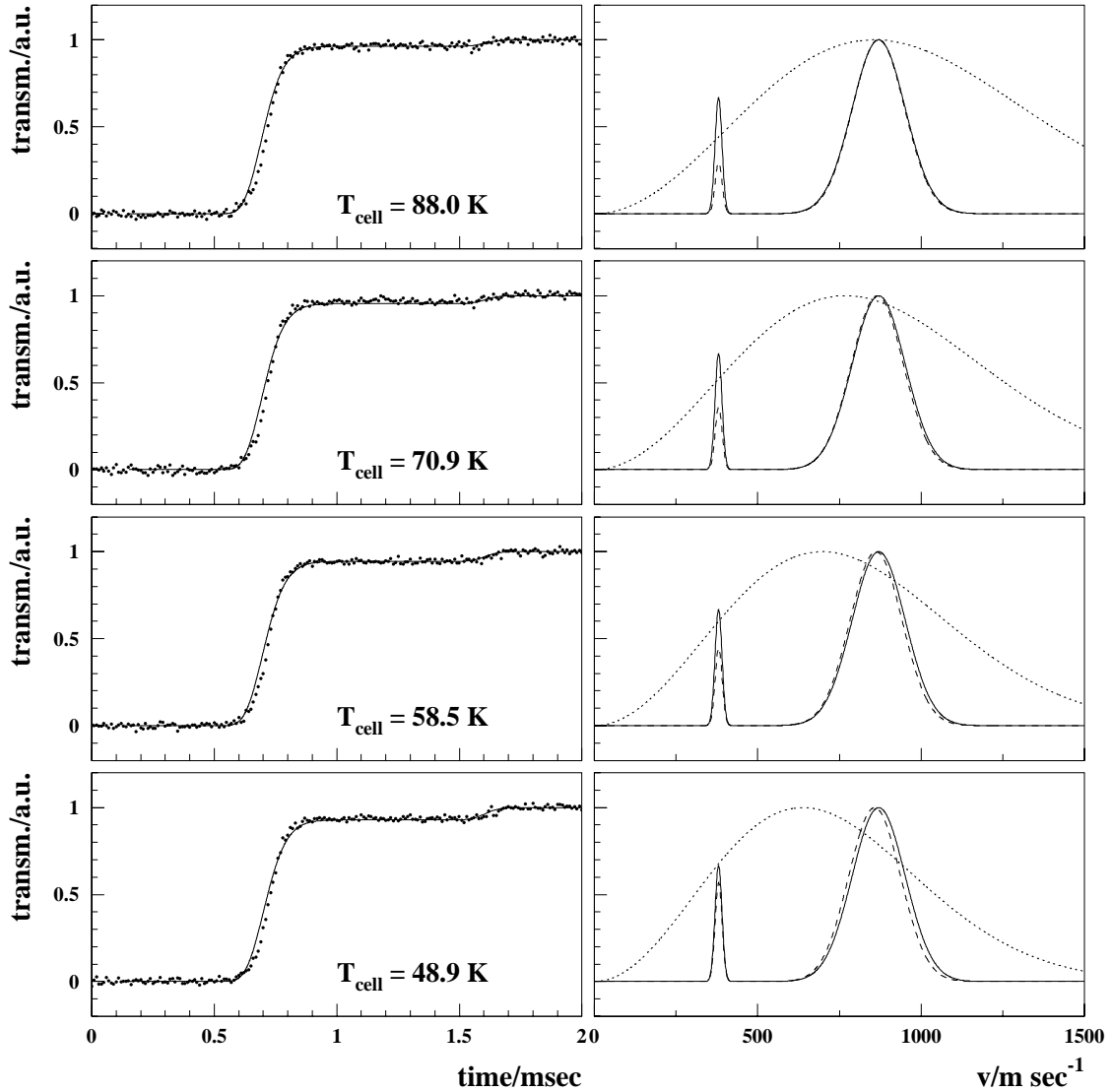


Figure 5.24:

Comparison of the measurements with the model for the new magnet system. The data points from the measurements for four different cell temperatures are shown on the left side. The solid line is the distribution over time of the geometrical transmission of the model shown on the right side weighted by a Maxwell distribution for the four different temperatures. The model assumes two Gaussians distributed around two different velocities. This geometrical transmission (dashed line on right side) is weighted by a Maxwell distribution (dotted line on right side) for four different temperatures giving the resulting transmission (solid line on right side).

5.4 Conclusion

Time of flight measurements are a convenient way to measure the velocity distribution of the atoms detected in the Breit-Rabi polarimeter. The transmissions of the former and the new magnet system simulated with the help of a Monte Carlo simulation showed good agreement with the measurements. The new sextupole magnet system now installed in the BRP shows favourable behaviour at the working points for hydrogen and deuterium (95 K and 65 K). Since the velocity windows found in the measurements agree with the velocity windows simulated with the Monte Carlo program the the intensity of atoms detected in the Breit-Rabi polarimeter should increase by a factor of about 1.6 at a cell temperature of 100 K compared to the former magnet system. This should quicken calibration measurements and improve statistics.

Chapter 6

Discussion and Outlook

The HERMES experiment will run with hydrogen after the HERA shutdown. Before July 1998 hydrogen was used at a cell temperature of about 100 K. This cell temperature was used for the beginning of the deuterium running period until it was seen that the degree of dissociation stays high for temperatures down to 65 K. Maybe the experience made in the year 2000 will make it possible to run at low temperatures with hydrogen as well.

The sextupole magnet system of the Breit-Rabi polarimeter has been optimized for temperatures lower than 100 K. The former magnet system showed a drop in the transmission for temperatures lower than 150 K. The new magnet system has higher transmission especially at low temperatures so that the statistic error of calibration measurements should be reduced. Therefore it should be possible to perform calibration measurements on shorter time scales.

The relative sensitivity of the target gas analyzer to detect atoms compared to molecules was calibrated for the deuterium running period. This value enters the equation of the degree of dissociation α^{TGA} which then has to be separated into α_r^{TGA} and α_0^{TGA} . With this the averaged values α_r and α_0 in the cell can be derived using the sampling correction c_α . Together with the atomic polarization the averaged target polarization P^T can then be calculated. For this analysis it would be preferable to have single κ values for certain time periods because the relative detection sensitivity changes e.g. when the setting of the ion-optics are changed. Since in the deuterium running period only ten reliable scans could be analyzed a mean value κ_{tot} seems to be preferable. It was found to have the value $\kappa_{tot} = 0.8606 \pm 0.0814$.

After the end of the long shutdown HERMES will run with a transverse hydrogen target. This makes room for new physics.

Appendix A

Compilation of κ Calibrations

In this chapter all the κ calibrations performed in the deuterium running period (July 1998 until September 2000) of the HERMES experiment are listed with various characteristic plots and comments.

In section A.1 the temperature scans are chronologically shown, then in section A.2 all the beam dumps. The values for κ extracted for these scans are summarized in a table in section A.3 and an averaged value for the whole deuterium running period (κ_{tot}) is given.

A.1 Temperature Scans

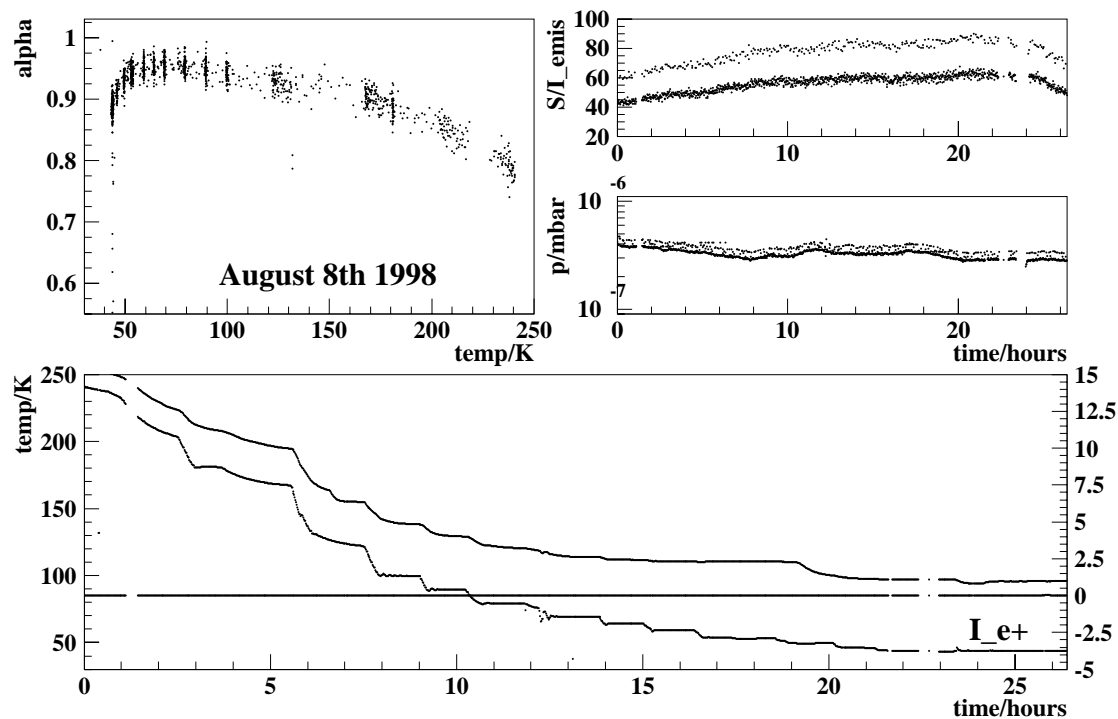
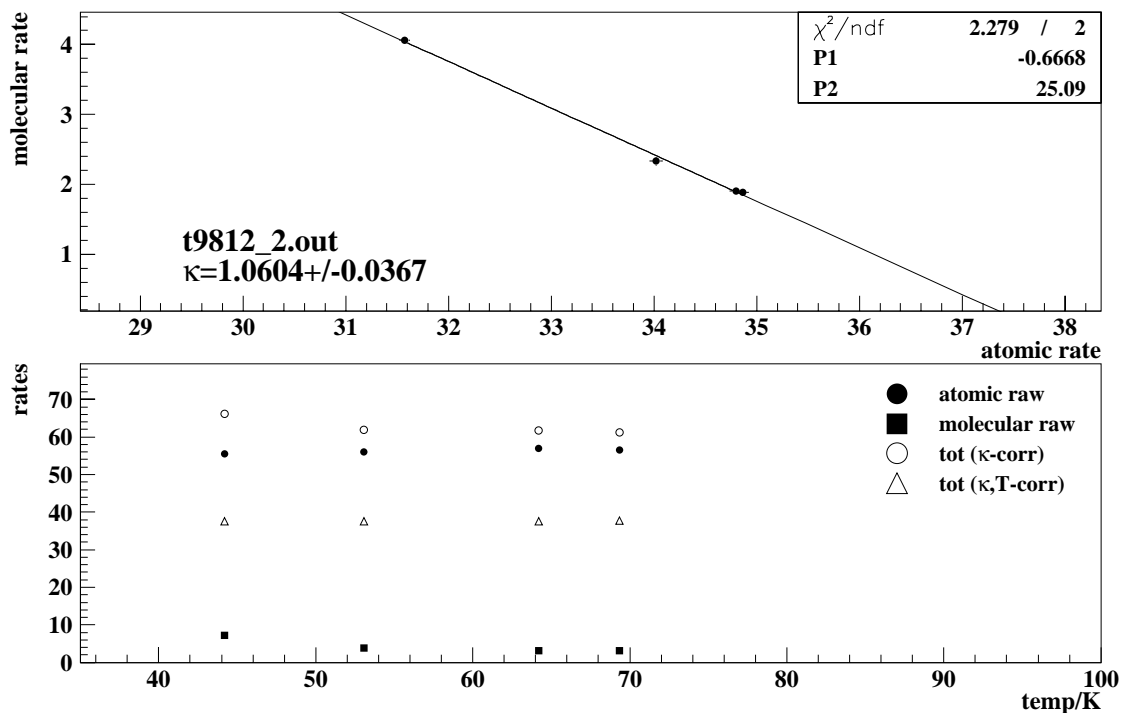


Figure A.1: Plot of the temperature scan on August 8th, 1998. The α^{TGA} does not show strong variation for low temperatures. The temperature of the extensiontube is high compared to the temperature of the cell and does not follow the variation of T_{cell} . This scan is excluded from the mean κ .



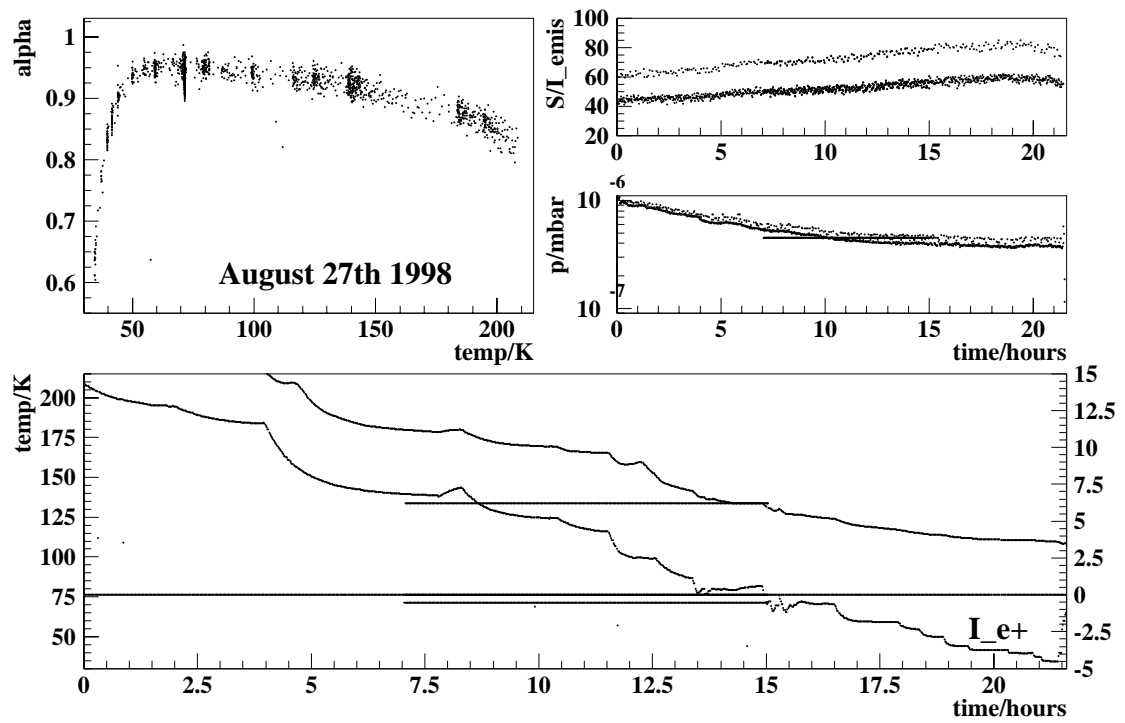
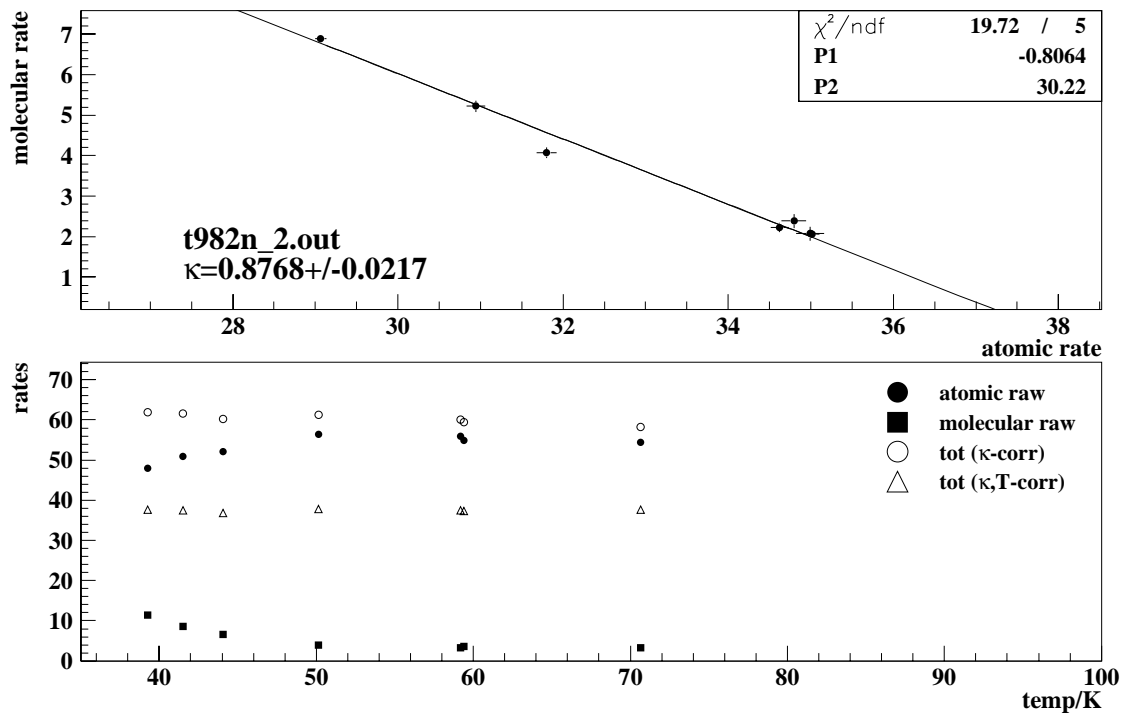


Figure A.2: Plot of the temperature scan on August 27th 1998. As in the temperature scan shown in figure A.1 the temperature of the extensiontube is extremely high compared to the temperature of the cell. For the period where the α^{TGA} varies the temperature of the extension tube is constant. This scan has not been taken into account for the mean κ .



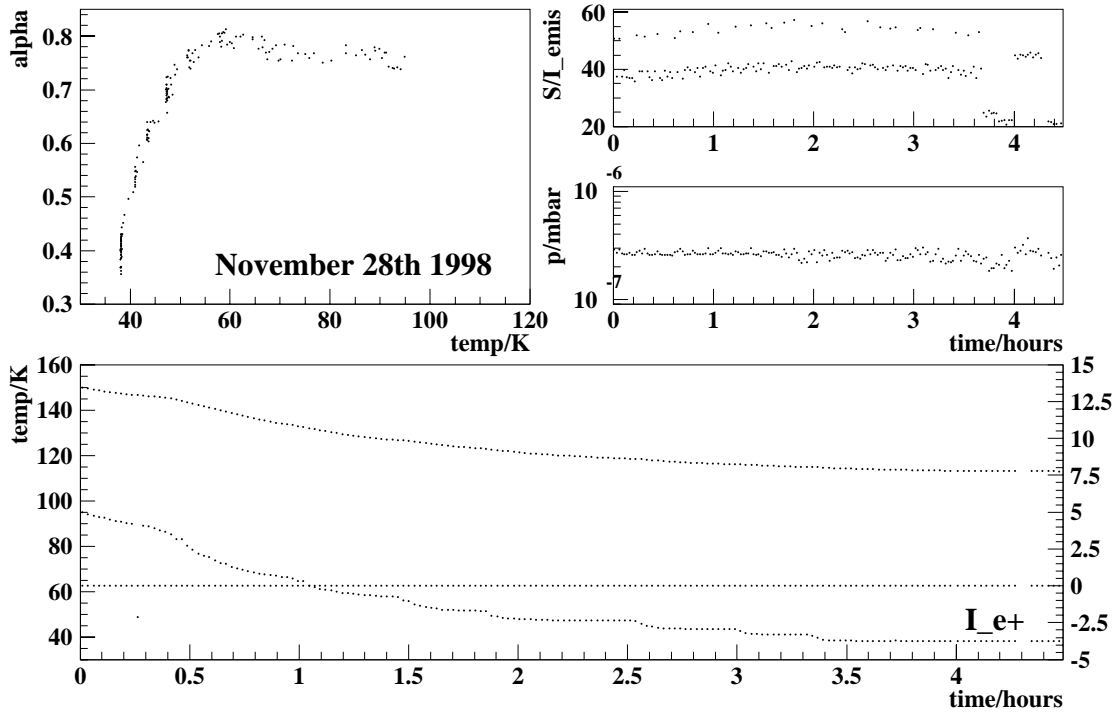
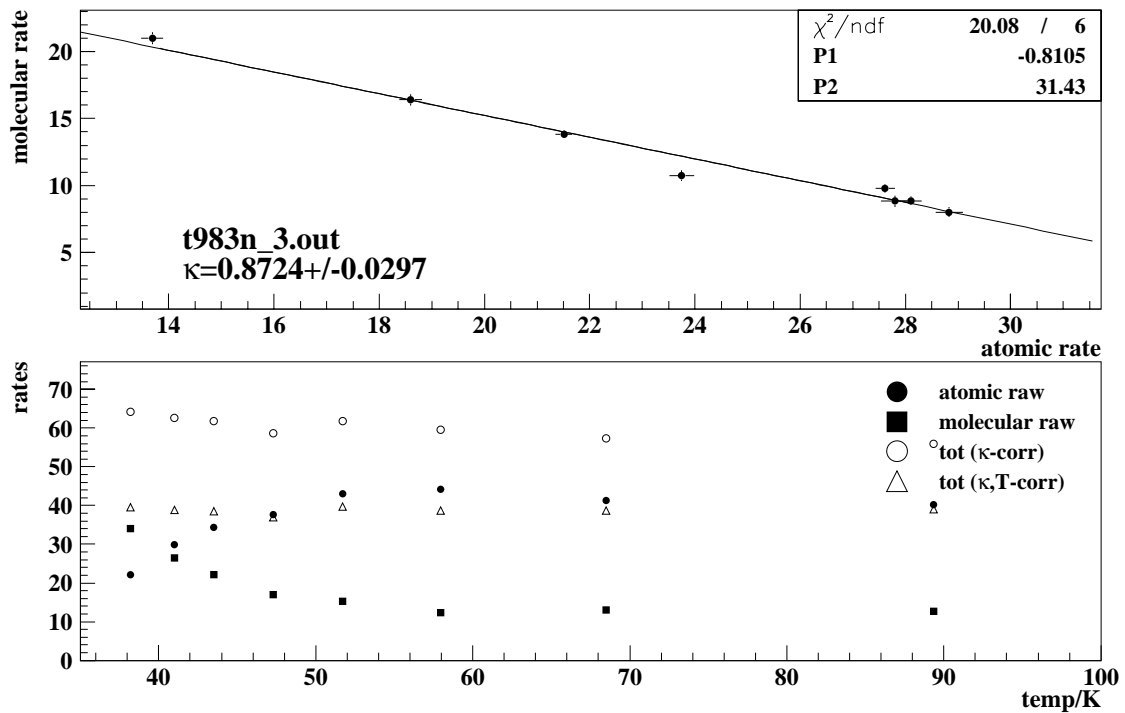


Figure A.3: Plot of the temperature scan on November 28th, 1998. As in the temperature scan shown in figure A.1 the temperature of the extensiontube is high compared to the temperature of the cell. This was an extremely short scan for which the temperature of the extensiontube was nearly constant. This scan has not been taken into account for the mean κ .



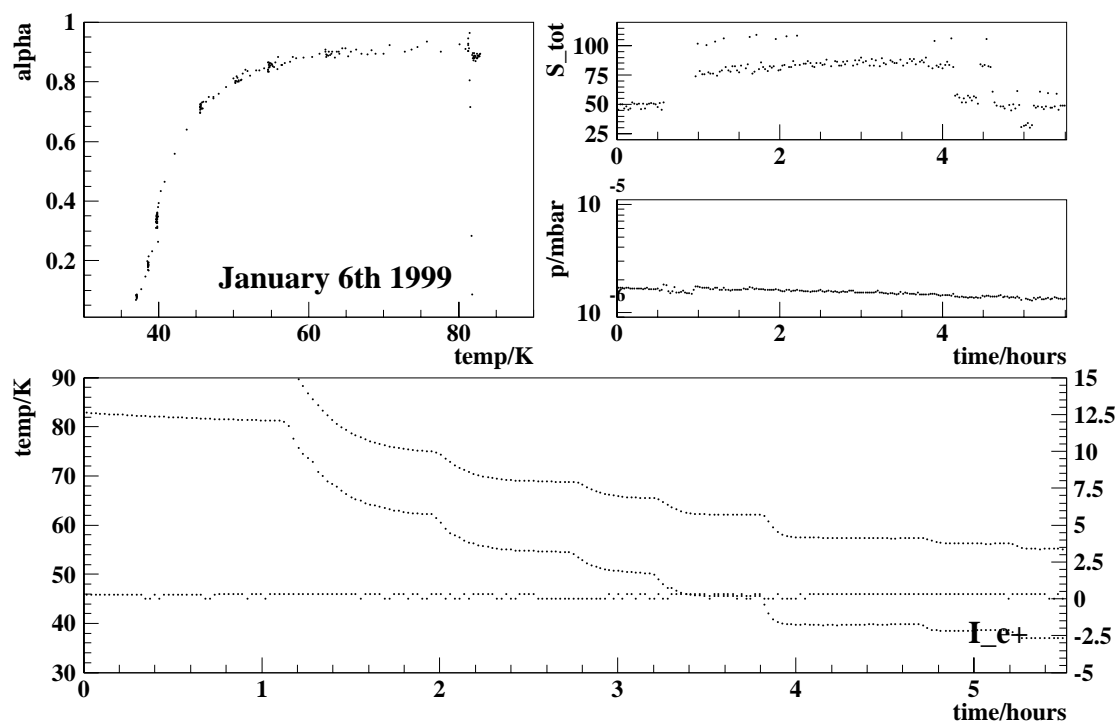
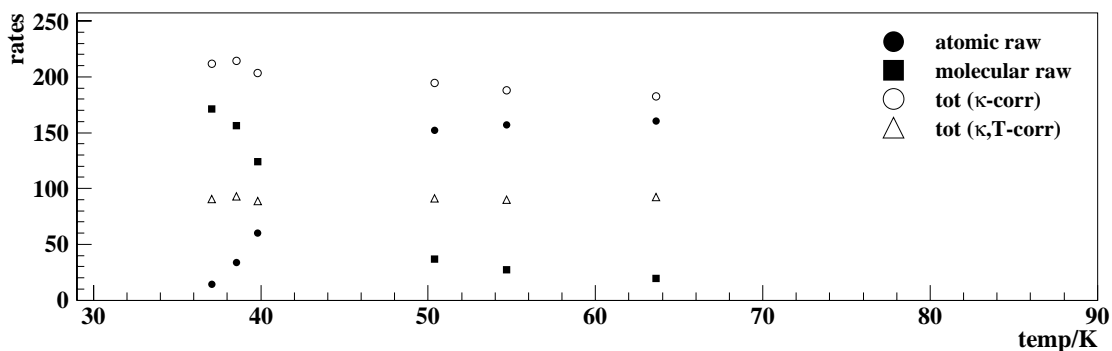
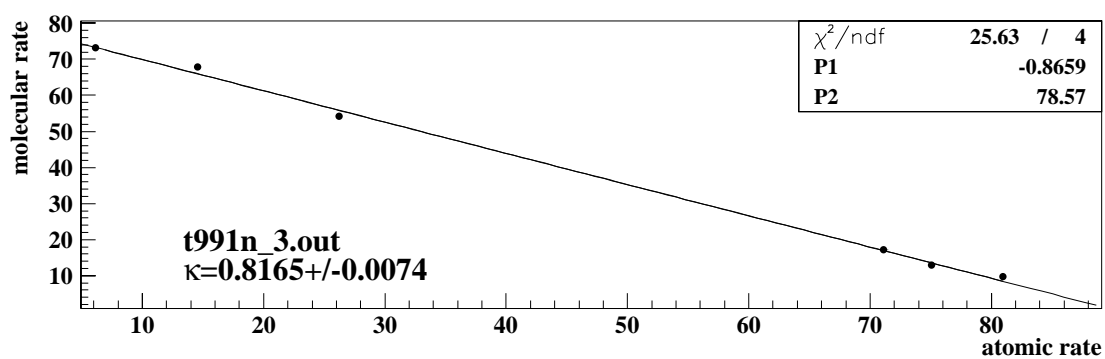


Figure A.4: Plot of the temperature scan on January 6th, 1999. This scan was done with the small storage cell installed. It is a short scan but α^{TGA} shows a strong variation at low cell temperatures and the temperature of the extension tube instantly follows the variation of T_{cell} . The corrected molecular rate over the corrected atomic rate shows little deviation from the fitted line, shown in the plot below.



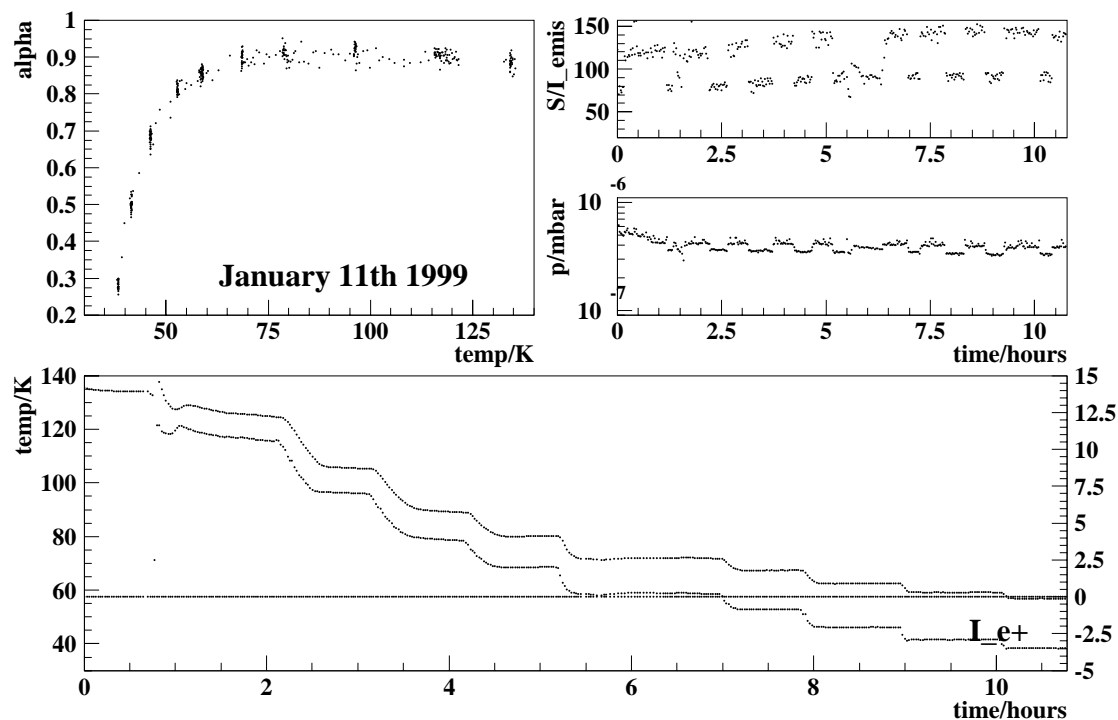
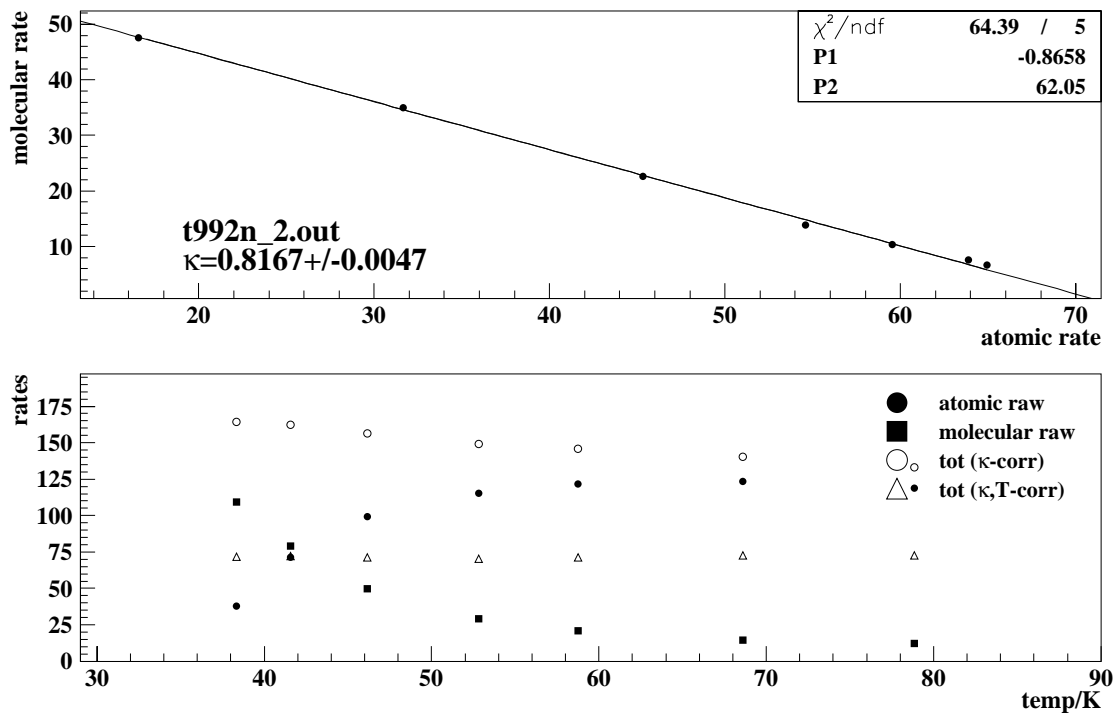


Figure A.5: Plot of the temperature scan on January 11th, 1999. This scan was also done with the small storage cell installed (Fig. A.4) and the temperature of the extension tube follows the temperature of the cell. The corrected molecular rate over the corrected atomic rate shows little deviation from the fitted line (plot below).



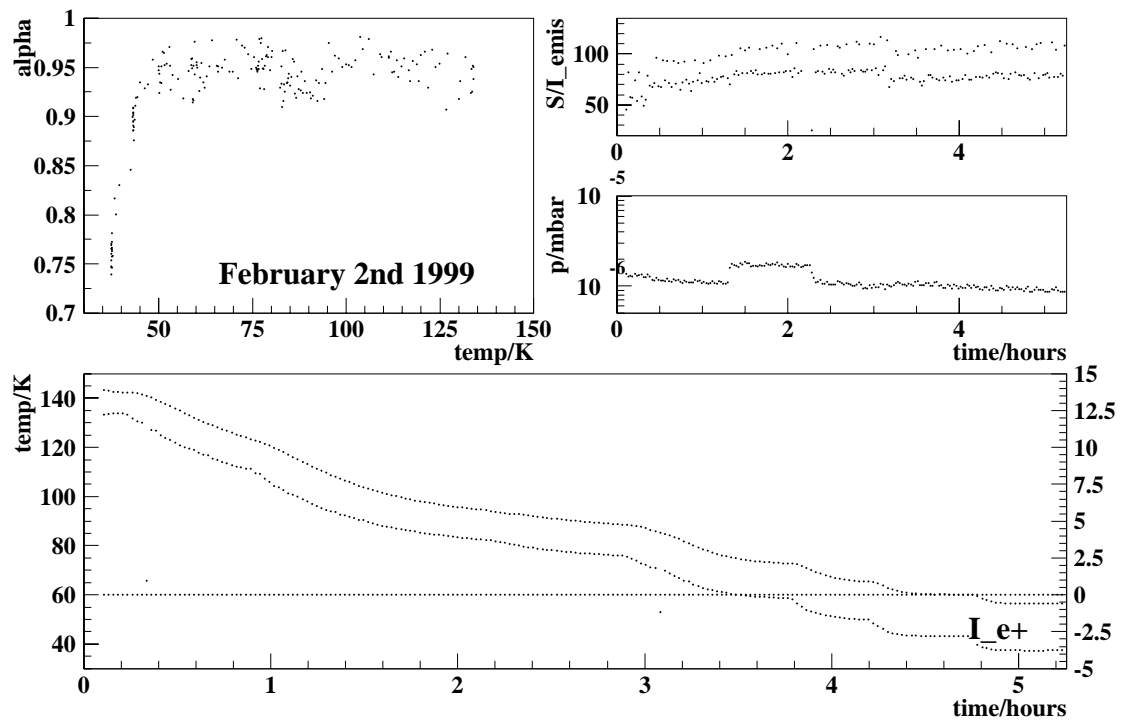
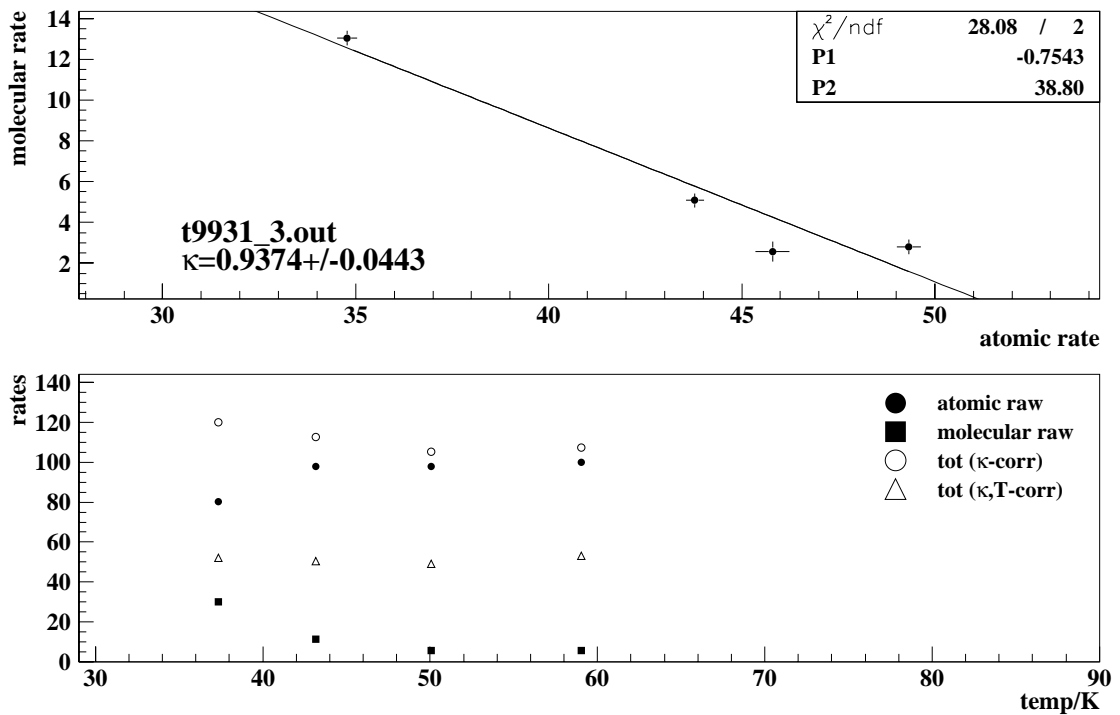


Figure A.6: Plot of the temperature scan on February 2nd, 1999. This scan shows a jump in the total rate plotted in the upper right corner of the upper plot. Therefore only the data after this jump ($t > 3.2$ hours) can be used to extract κ . But in this scan α^{TGA} shows only little variation which makes it hard to extract κ .



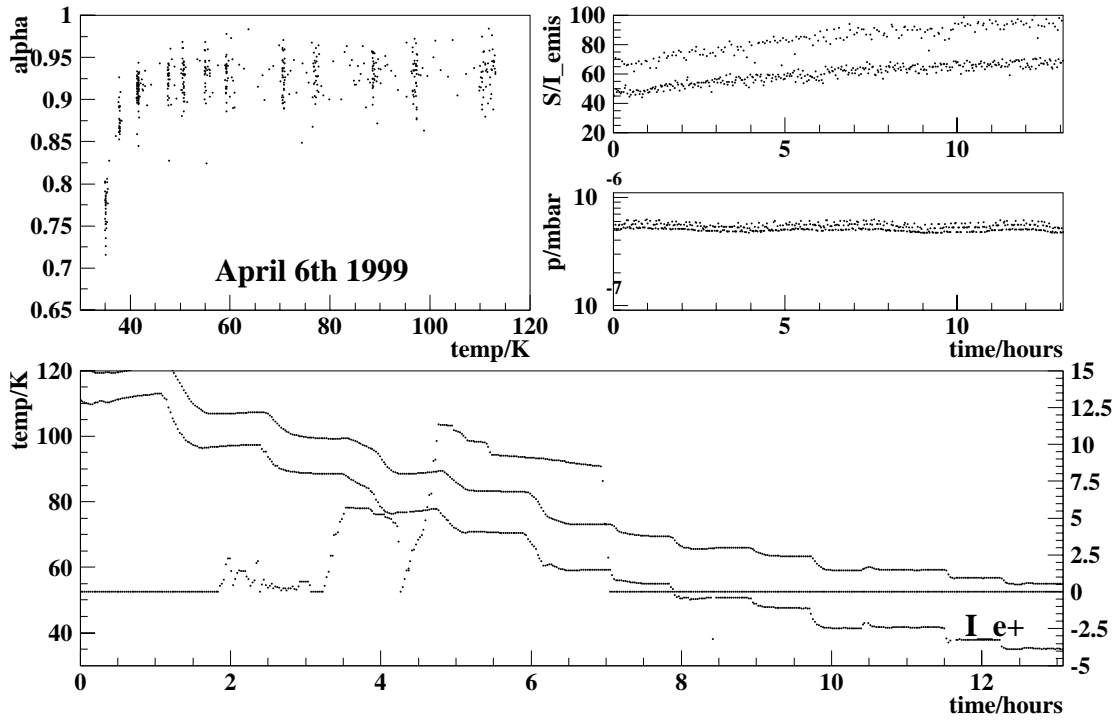
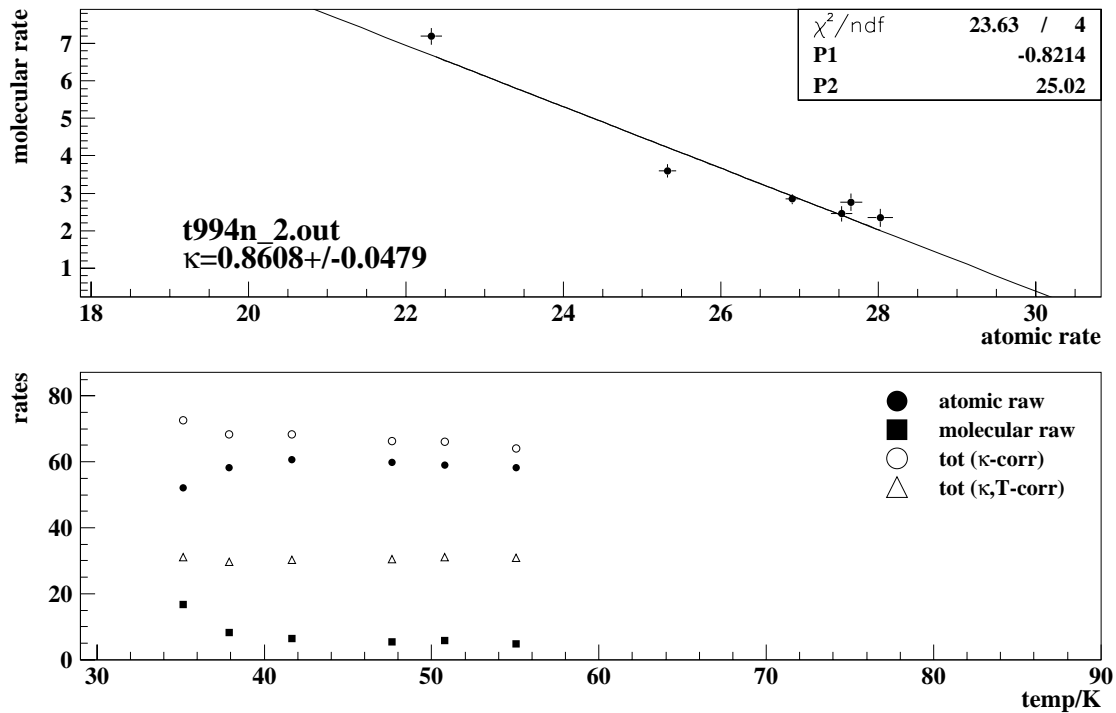


Figure A.7: Plot of the temperature scan on April 6th, 1999. A new positron beam was injected during the scan. For the extraction of a value for κ only the temperature steps after the dump of the positron beam ($t > 7$ hours) have been taken into account. It has to be noticed that the α^{TGA} shows only little variation.



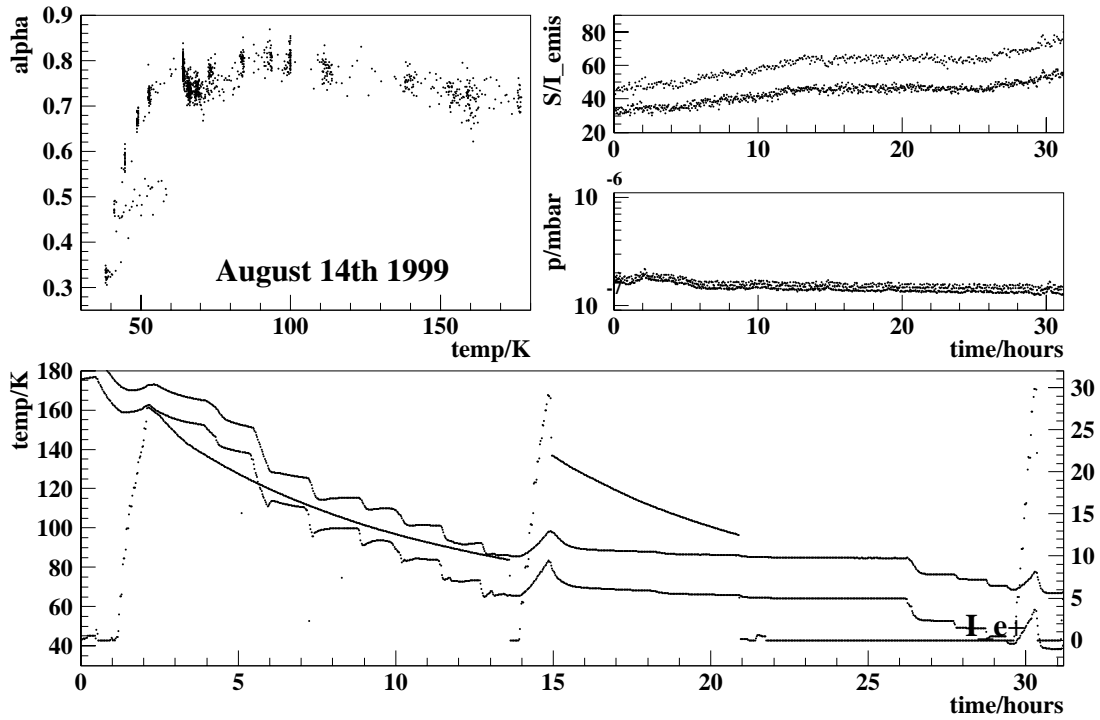
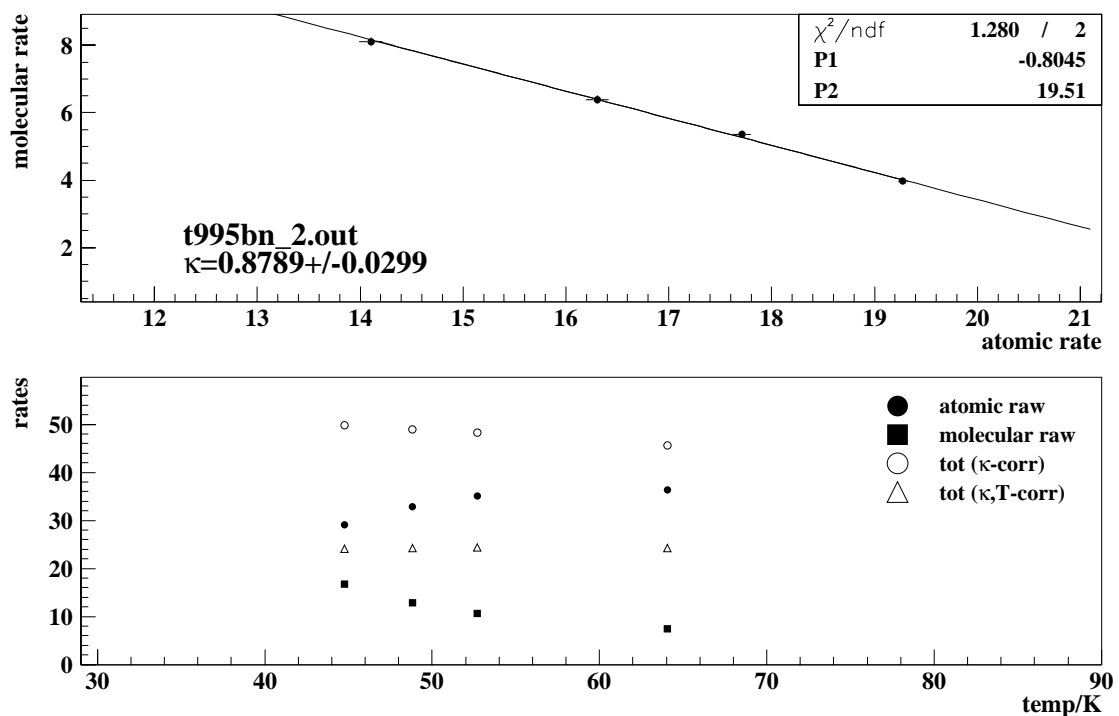


Figure A.8: Plot of the temperature scan on August 14th, 1999. Unfortunately new positron beams were successfully injected twice while this scan was done. A jump in α^{TGA} can especially be seen for the period $T_{cell} \approx 70$ K. This scan was divided into two parts for the extraction of kappa: the three last steps before the injection of the second positron beam ($10 \text{ hours} < t < 14 \text{ hours}$) and after the dump of the second positron beam ($21 \text{ hours} < t < 29.5 \text{ hours}$) has been used to extract κ . The average value κ_{avg} for this scan is the average of all four κ_i .



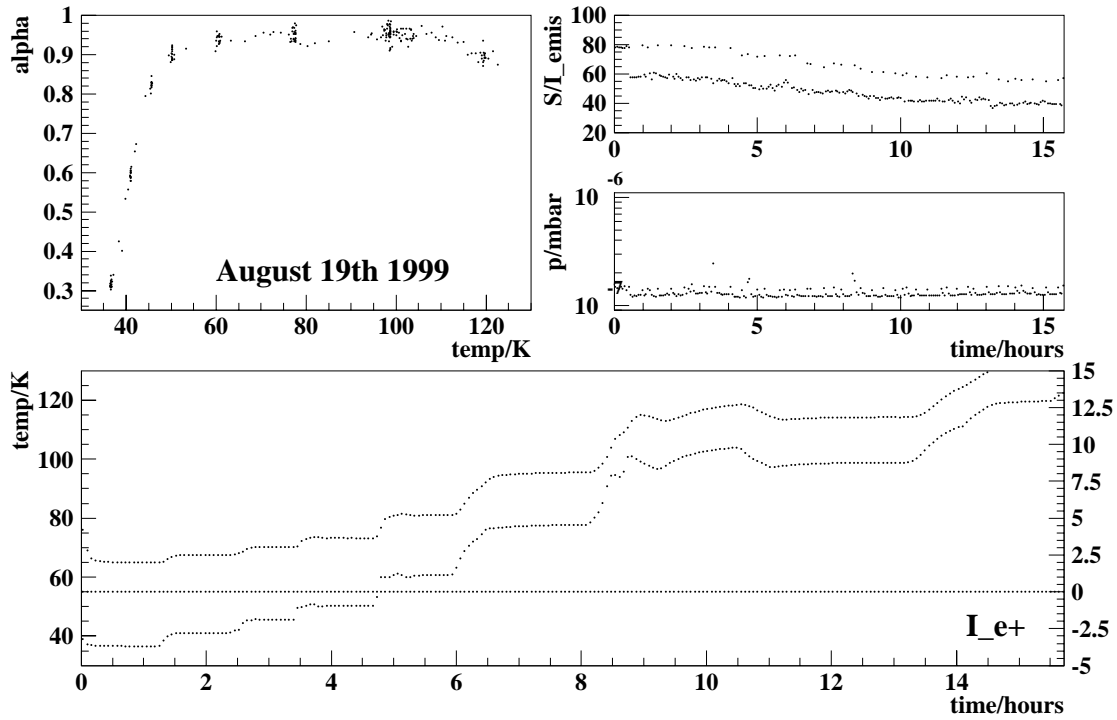
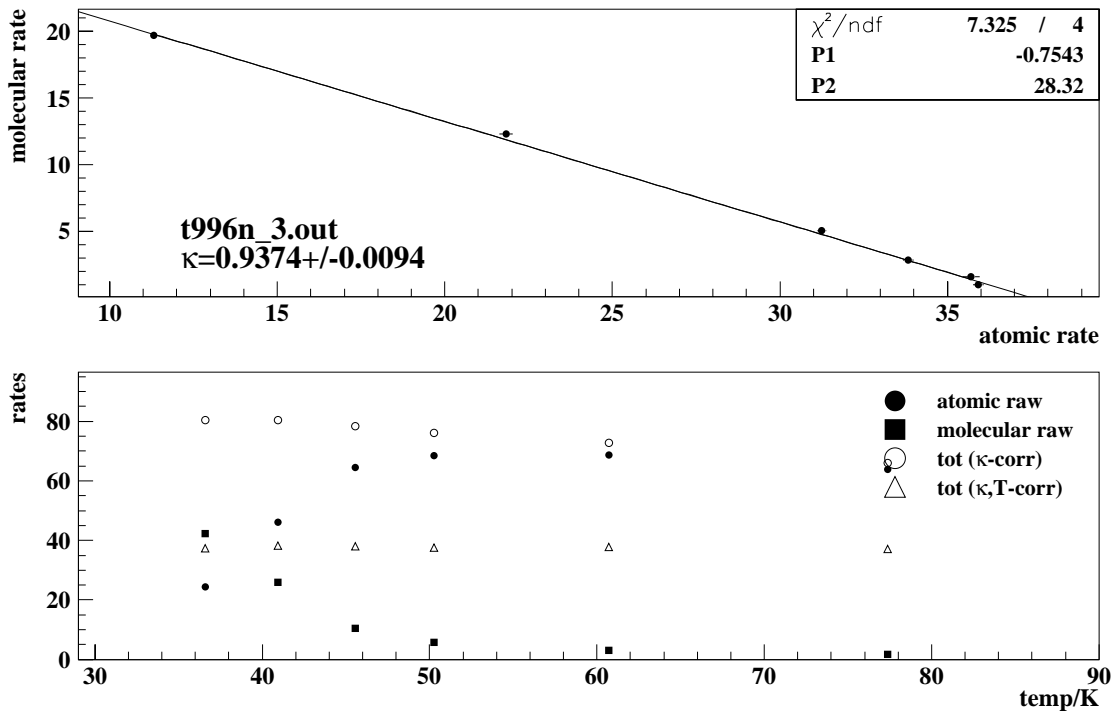


Figure A.9: Plot of the temperature scan on August 19th, 1999. The α^{TGA} shows a strong variation over the cell temperature. The difference of the temperatures of the cell and the extension tube is small even at low cell temperatures. A huge difference of the κ_i values extracted from two and three state injection (see appendix A.3) is seen. The upper right plot in the figure above shows that three state injection for this scan does not have good statistics.



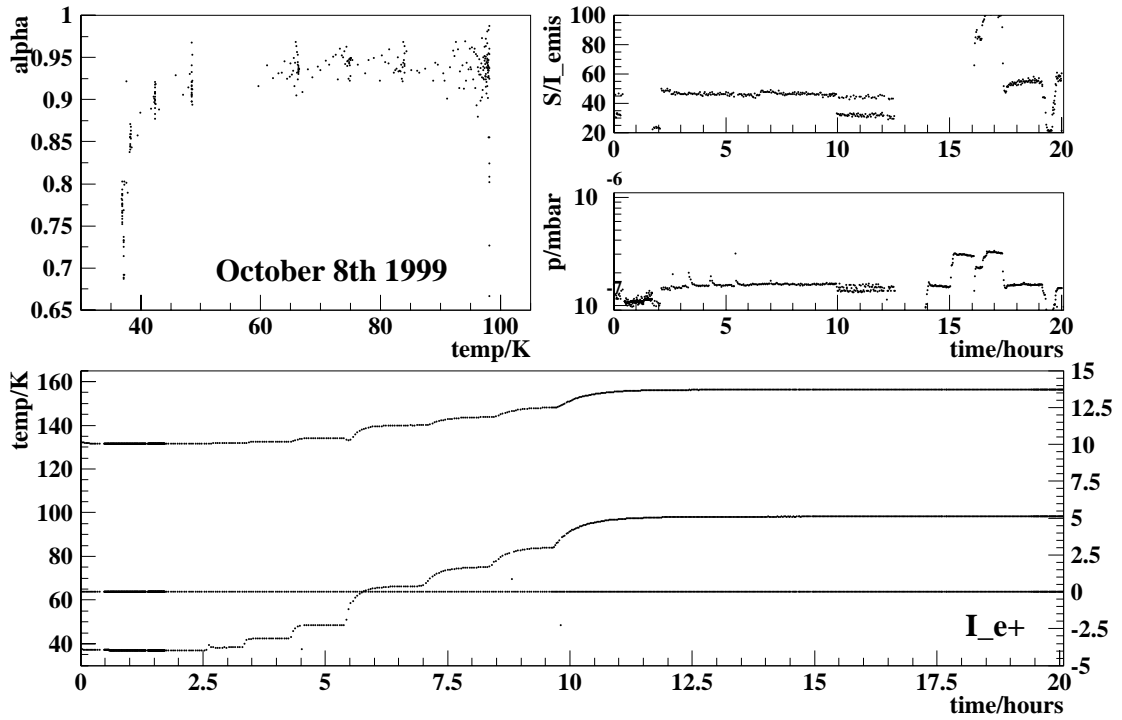
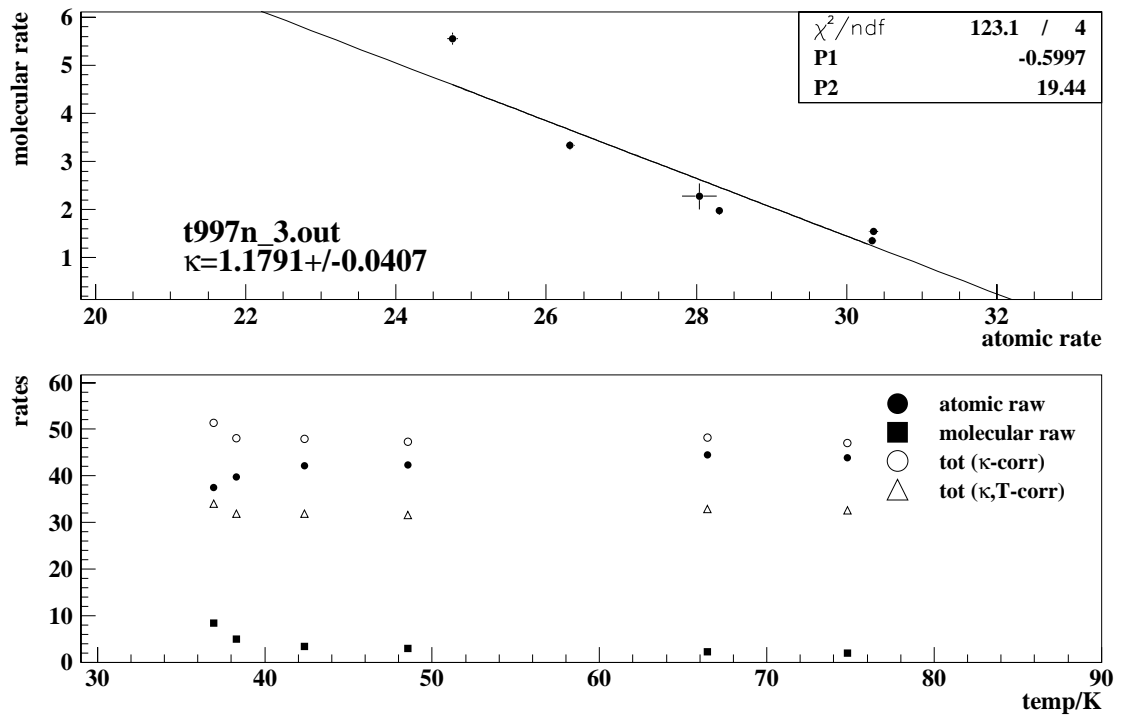


Figure A.10: Plot of the temperature scan on October 8th, 1999. The temperature of the extension tube does not at all follow the variation of the cell temperature and they show a huge gap as seen in the scans from 1998 (Fig. A.1, A.2 and A.3). The extension tube probably had a very low thermal contact to the sample tube. The κ from this scan did not contribute to the mean κ .



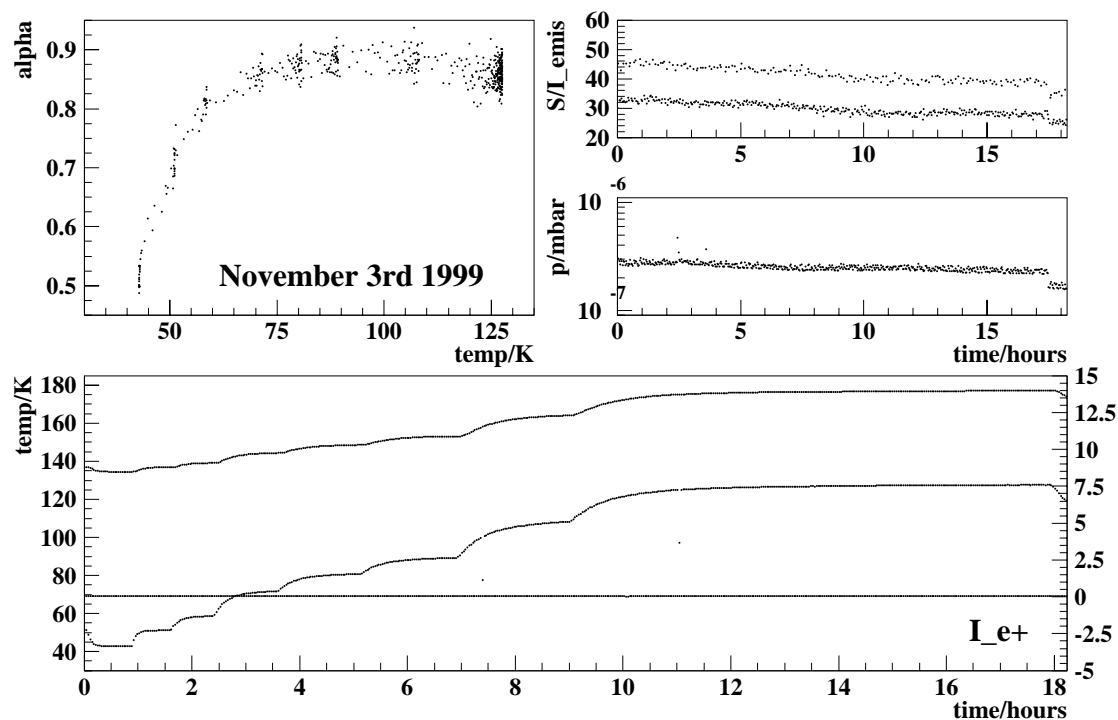
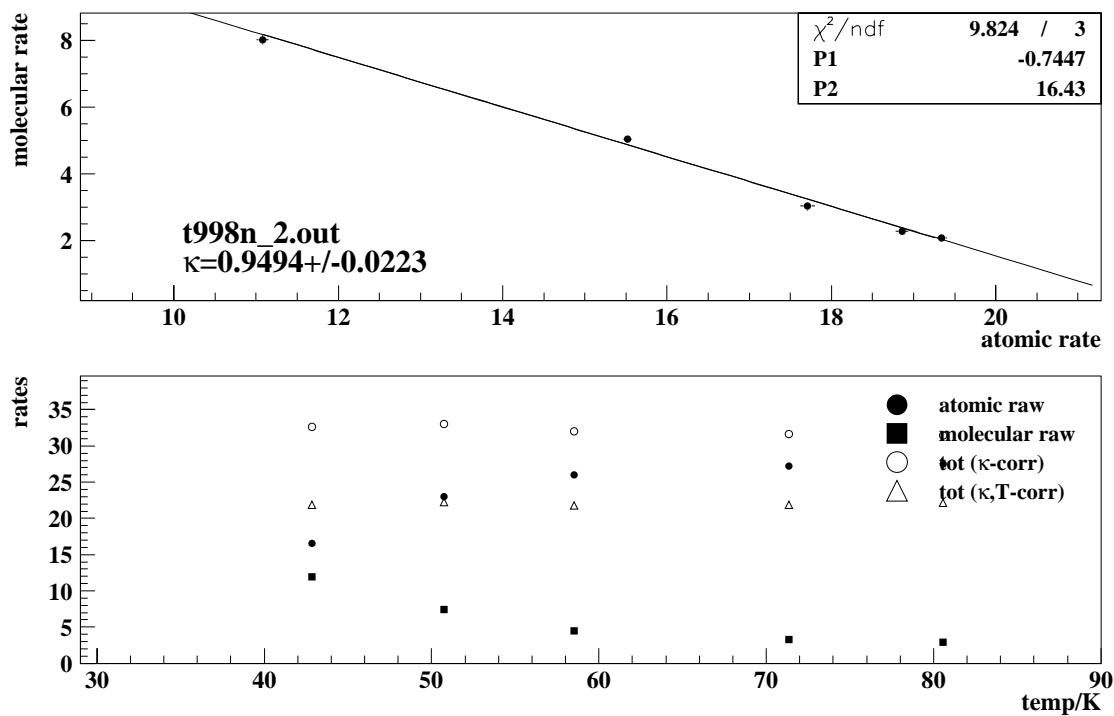


Figure A.11: Plot of the temperature scan on November 3rd, 1999. The cell was not changed since the beginning of October. The mounting of the extension tube seems to result in a low thermal contact since the temperature of the extension tube does not at all follow the variation of the cell temperature. The κ from this scan did not contribute to the mean κ .



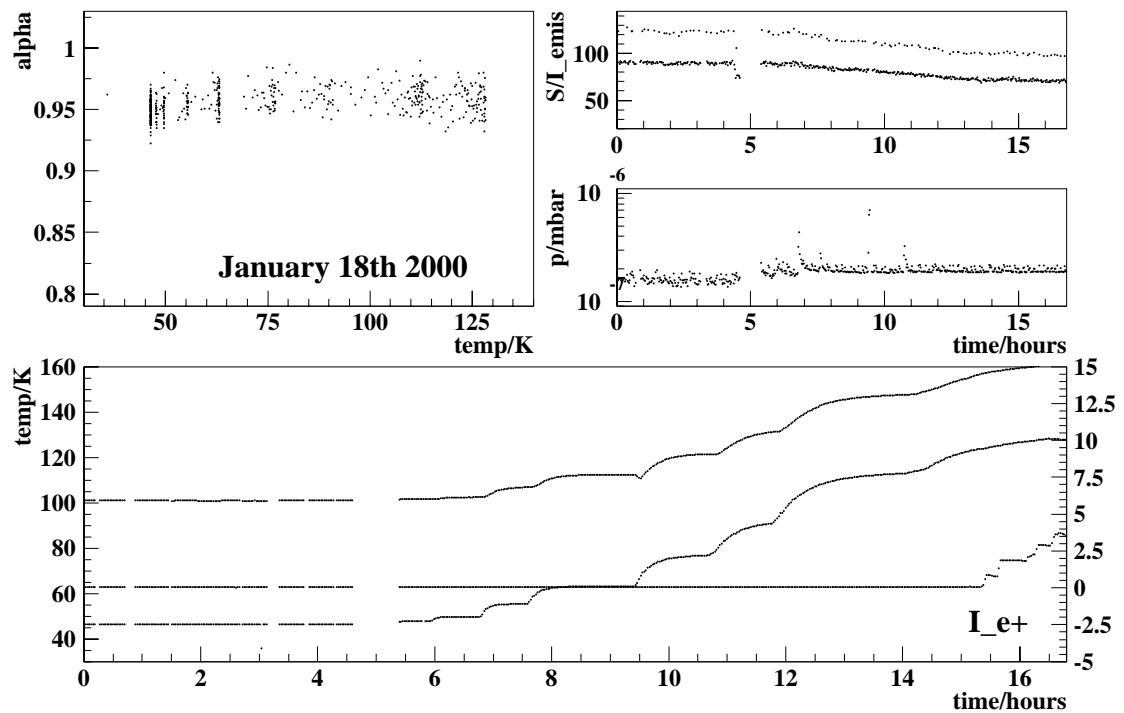
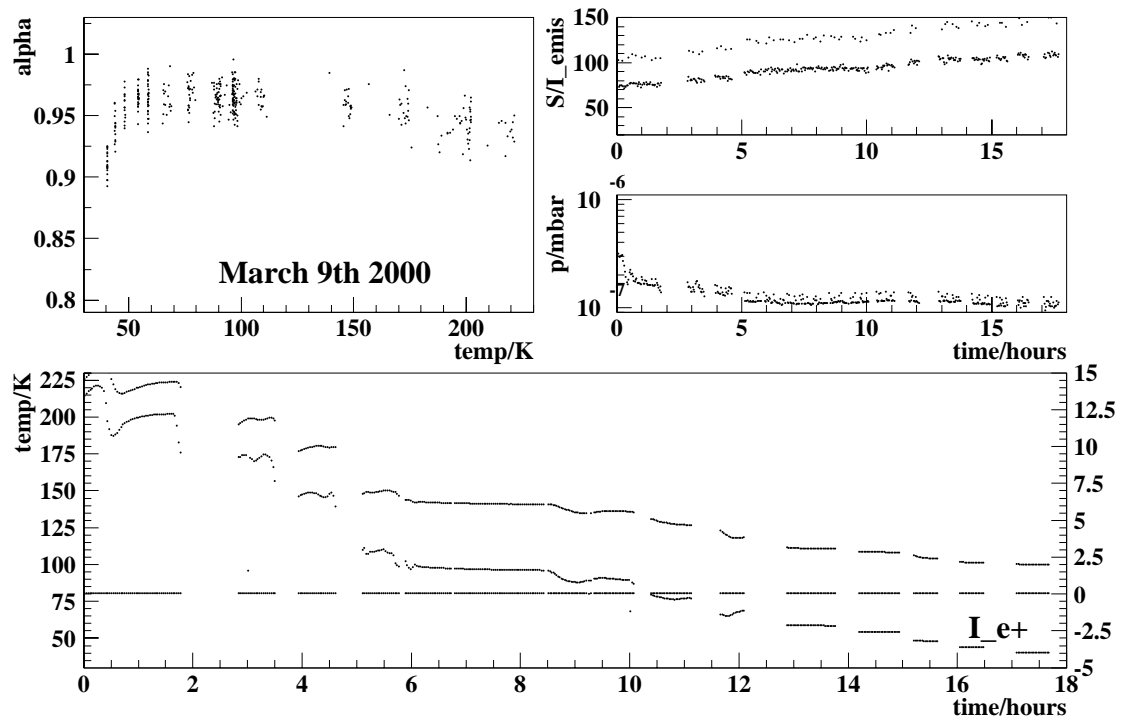


Figure A.12:

Top: Plot of the temperature scan on January 18th, 2000. A big gap between T_{et} and T_{cell} is seen. The α^{TGA} does not show any variation. Therefore no κ can be extracted from this scan.

Bottom: Plot of the temperature scan on March 9th, 2000. A big gap between T_{et} and T_{cell} is seen. The α^{TGA} does not show any variation. Therefore no κ can be extracted from this scan.



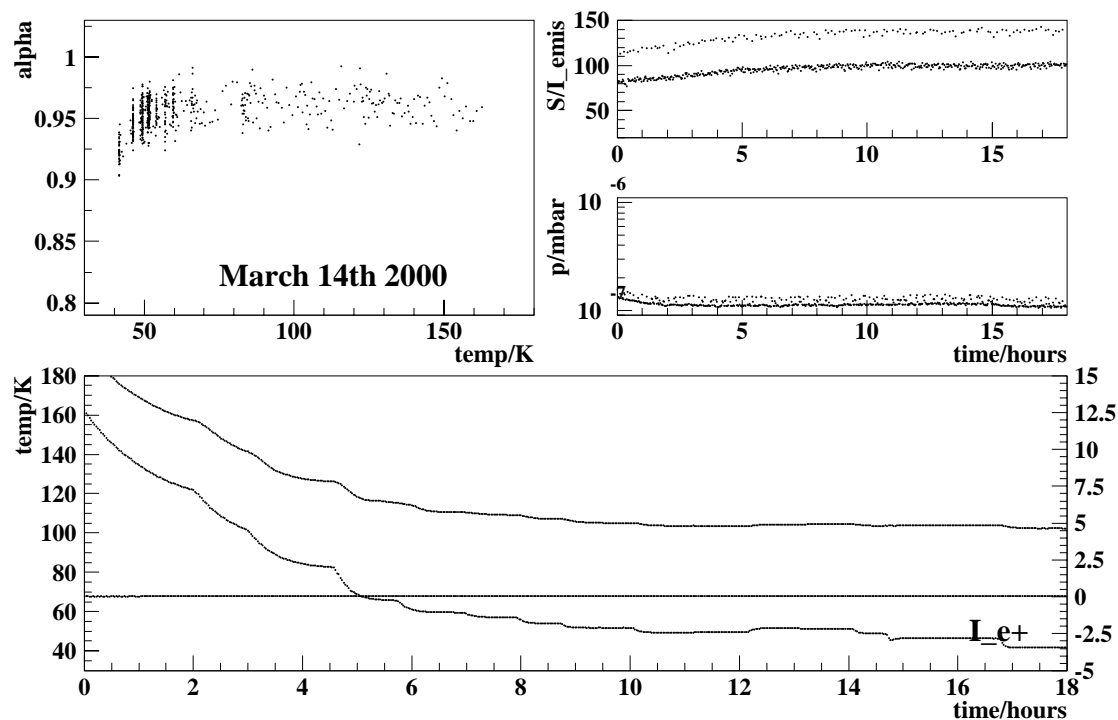
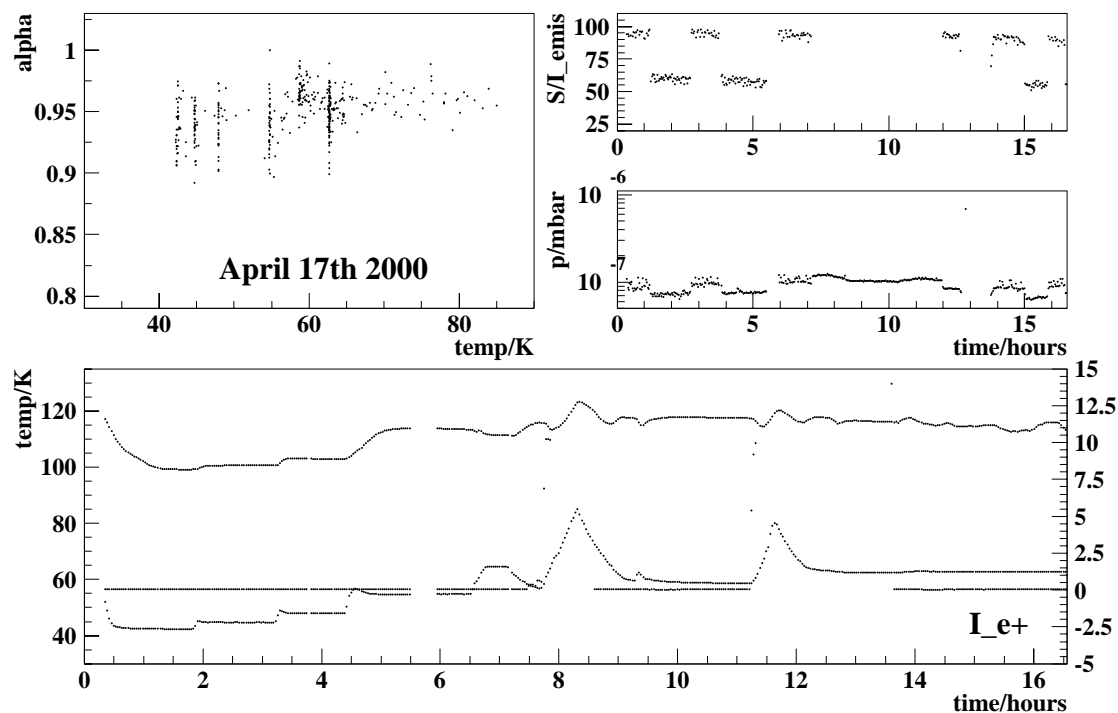


Figure A.13:

Top: Plot of the temperature scan on March 14th, 2000. A big gap between T_{et} and T_{cell} is seen. The α^{TGA} does not show any variation. Therefore no κ can be extracted from this scan.

Bottom: Plot of the temperature scan on April 17th, 2000. A big gap between T_{et} and T_{cell} is seen. The α^{TGA} does not show any variation. Therefore no κ can be extracted from this scan.



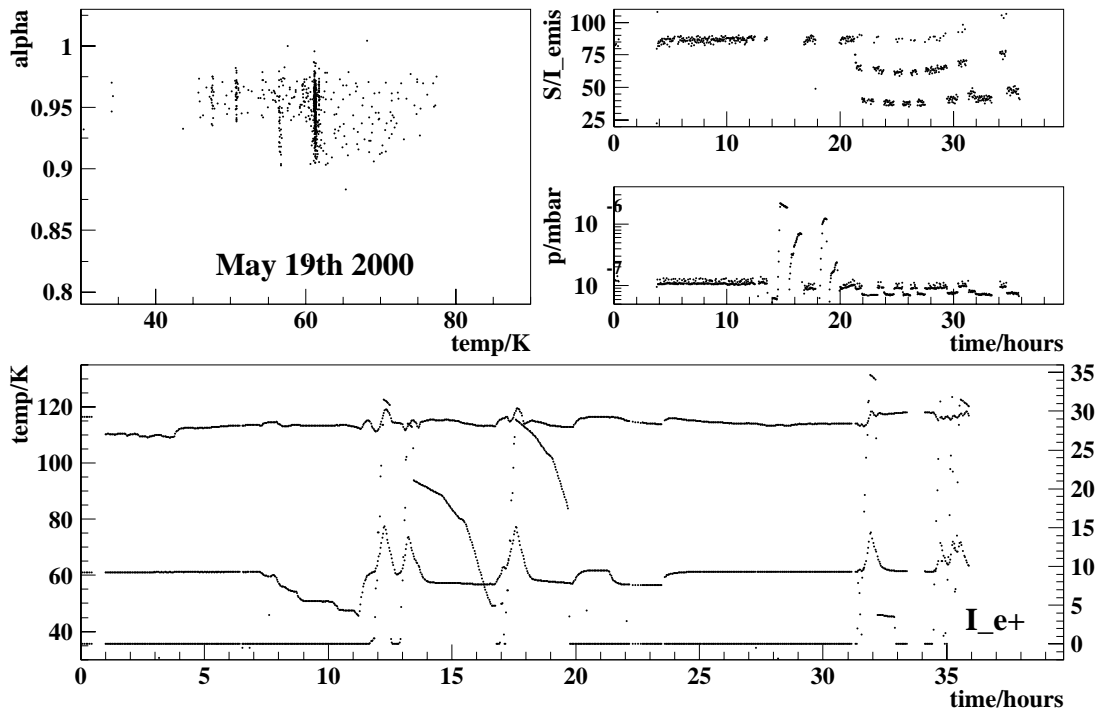
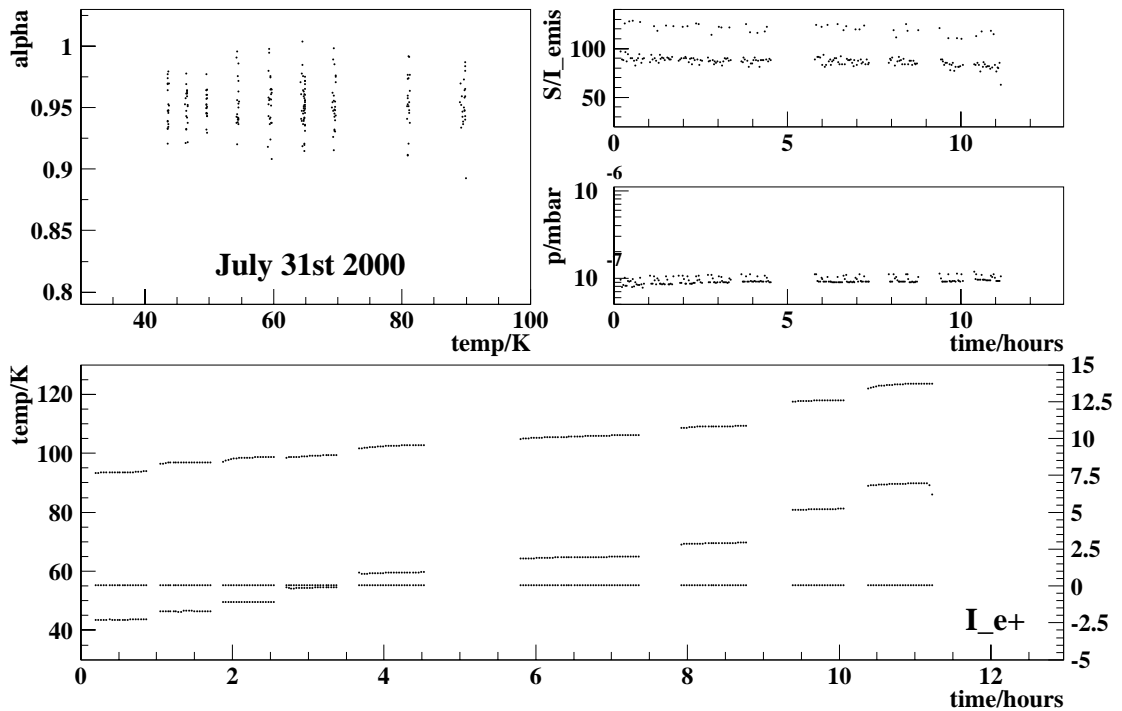


Figure A.14:

Top: Plot of the temperature scan on May 19th, 2000. A big gap between T_{et} and T_{cell} is seen. The α^{TGA} does not show any variation. Therefore no κ can be extracted from this scan.

Bottom: Plot of the temperature scan on July 31st, 2000. A big gap between T_{et} and T_{cell} is seen. The α^{TGA} does not show any variation. Therefore no κ can be extracted from this scan.



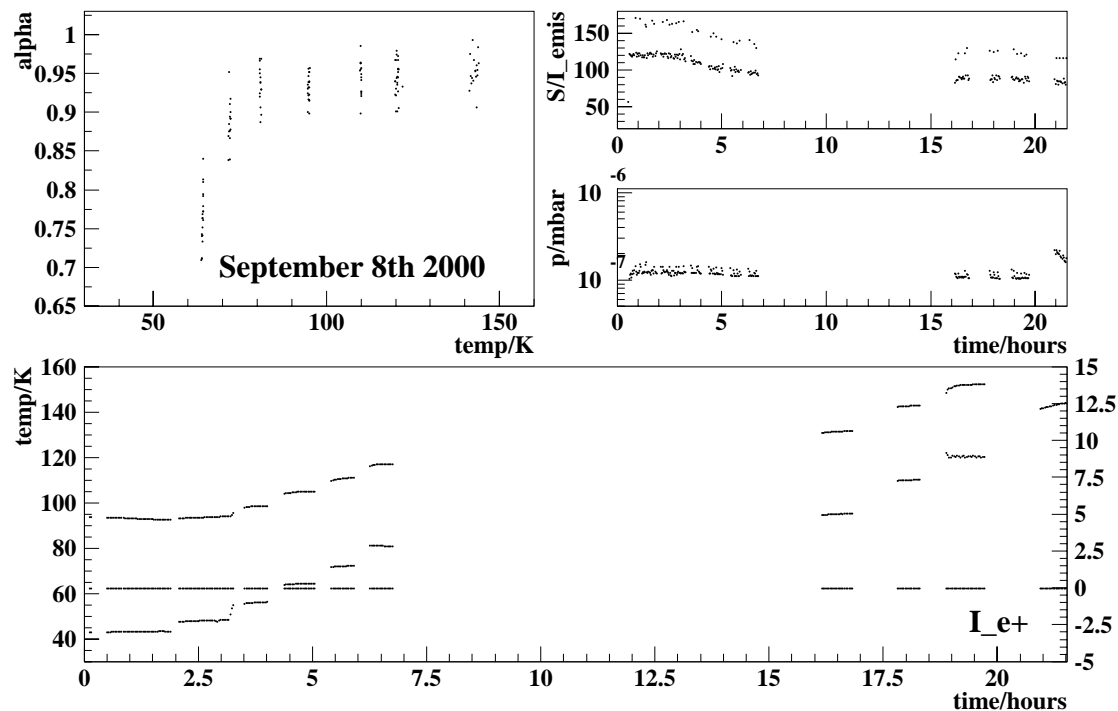
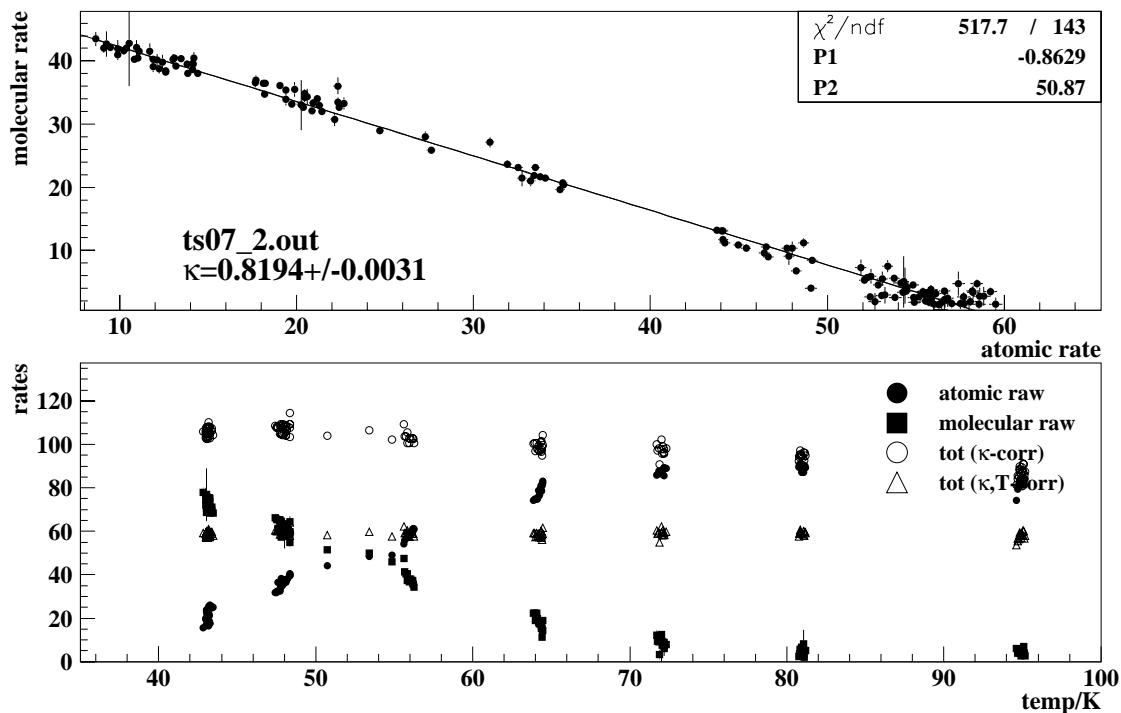


Figure A.15: Plot of the temperature scan on September 8th, 2000. This is a mixture of beam dump and temperature scan since the α^{TGA} changes at a certain constant temperature niveau as seen in figure 4.10. But considering ever single point of the data to be at a constant temperature itself, it can be used as a temperature scan.



A.2 Beam Dumps

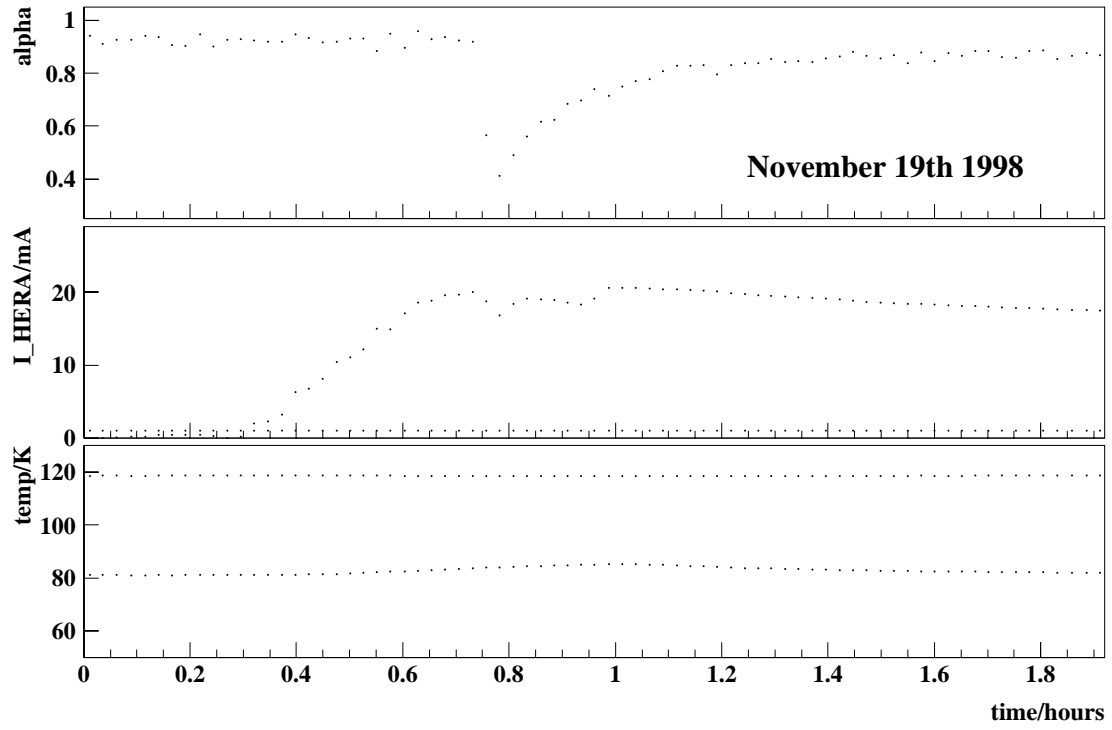
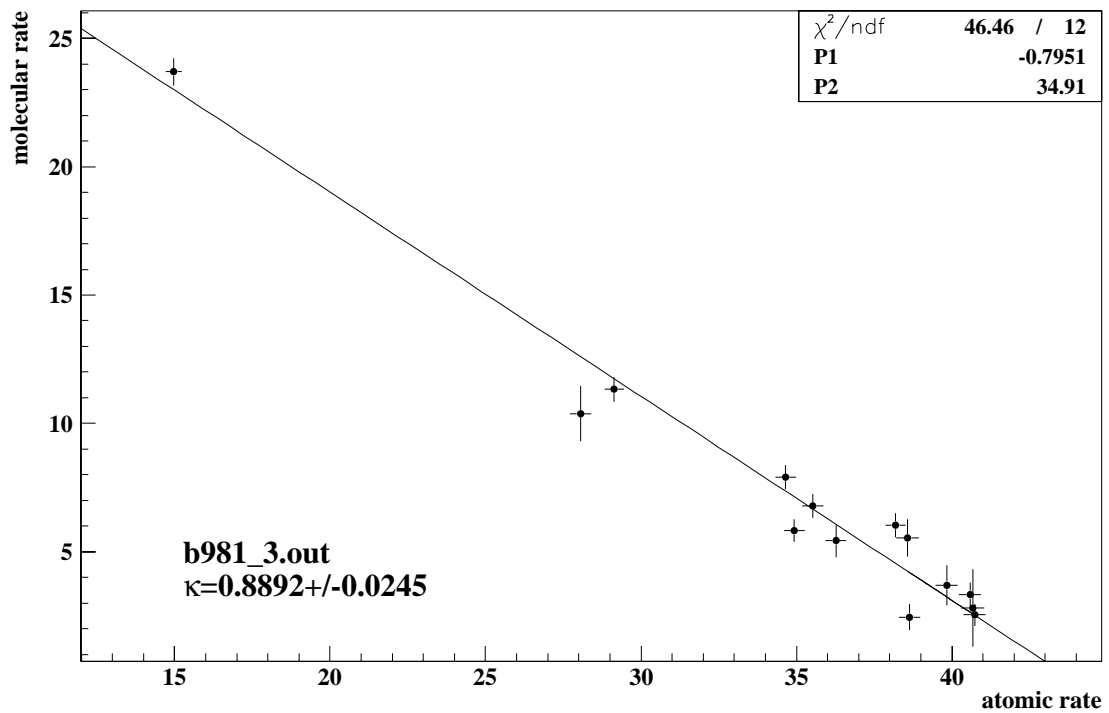


Figure A.16: Plot of the beam dump on November 19th, 1998. This was not an actual beamdump, HERA was changing the position of the positron beam. Since there is a sudden drop in the α^{TGA} and a recovery at constant cell temperature κ can be extracted from this data.



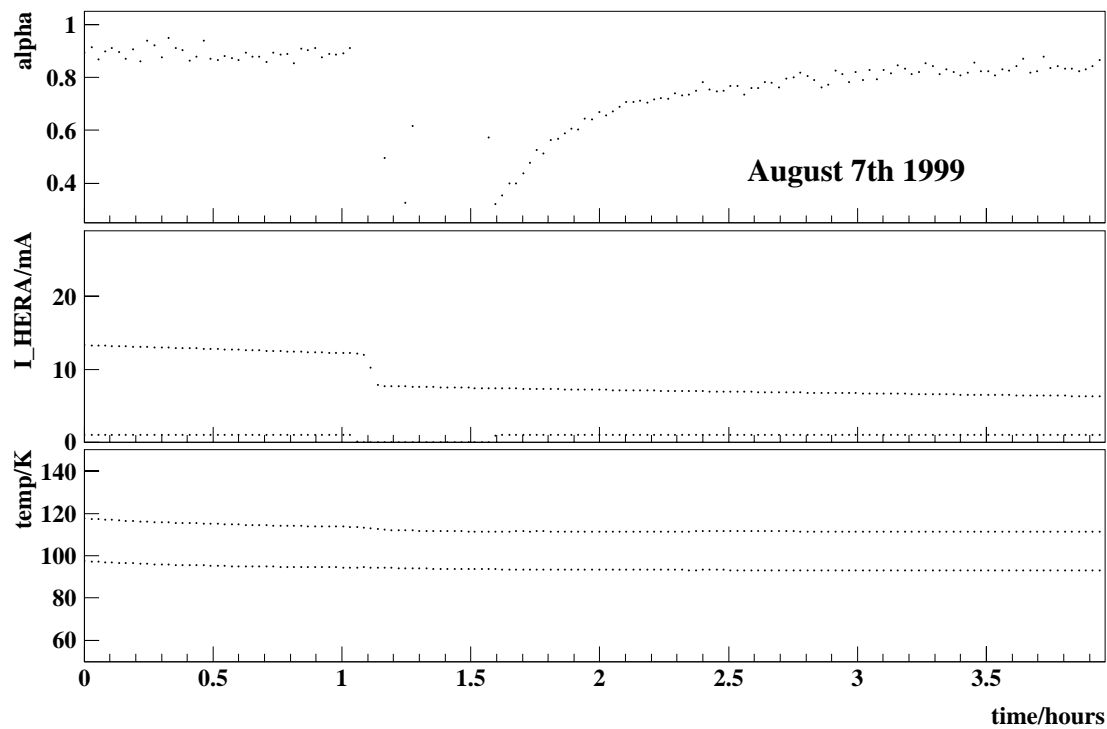
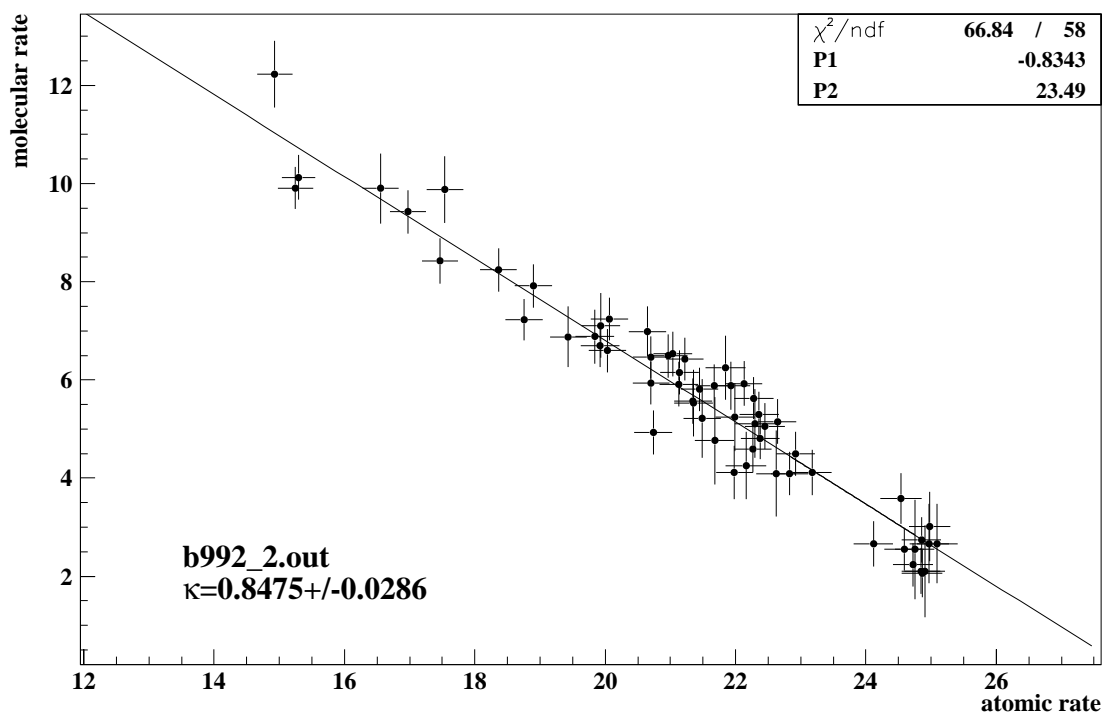


Figure A.17: Plot of the beam dump on August 7th, 1999. The sudden drop in the α^{TGA} is caused by a loss of a part of the HERA positron beam. For the recovery of α^{TGA} the cell temperature is constant so that κ can be extracted from this data.



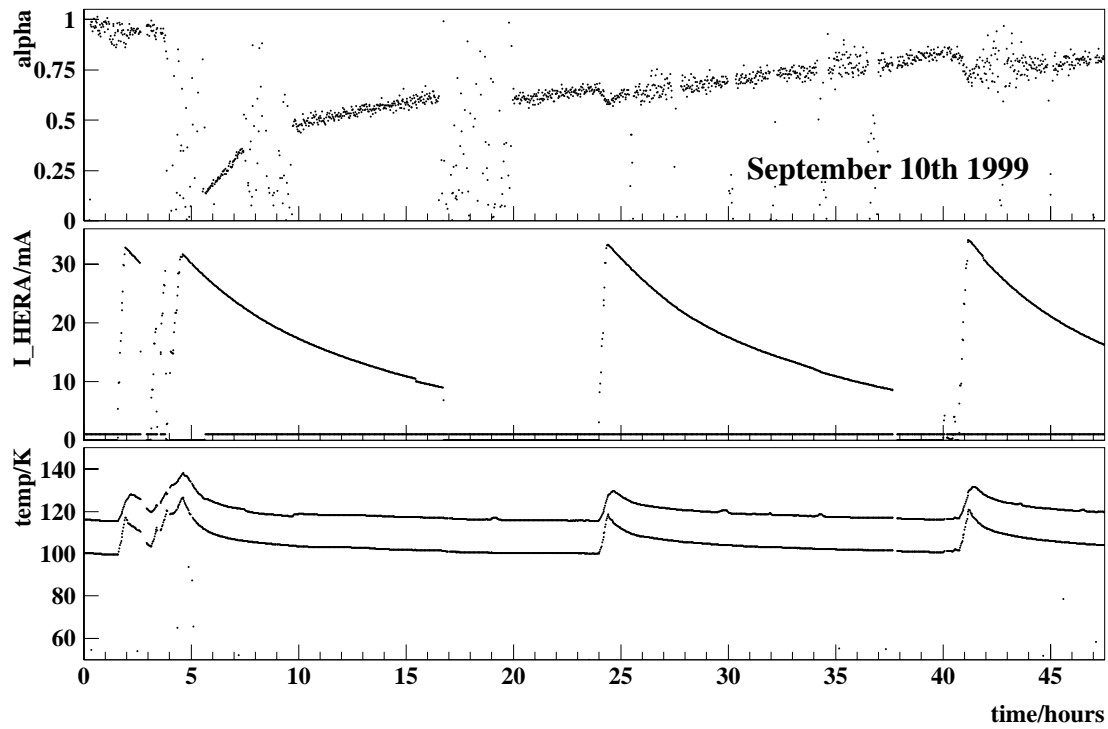
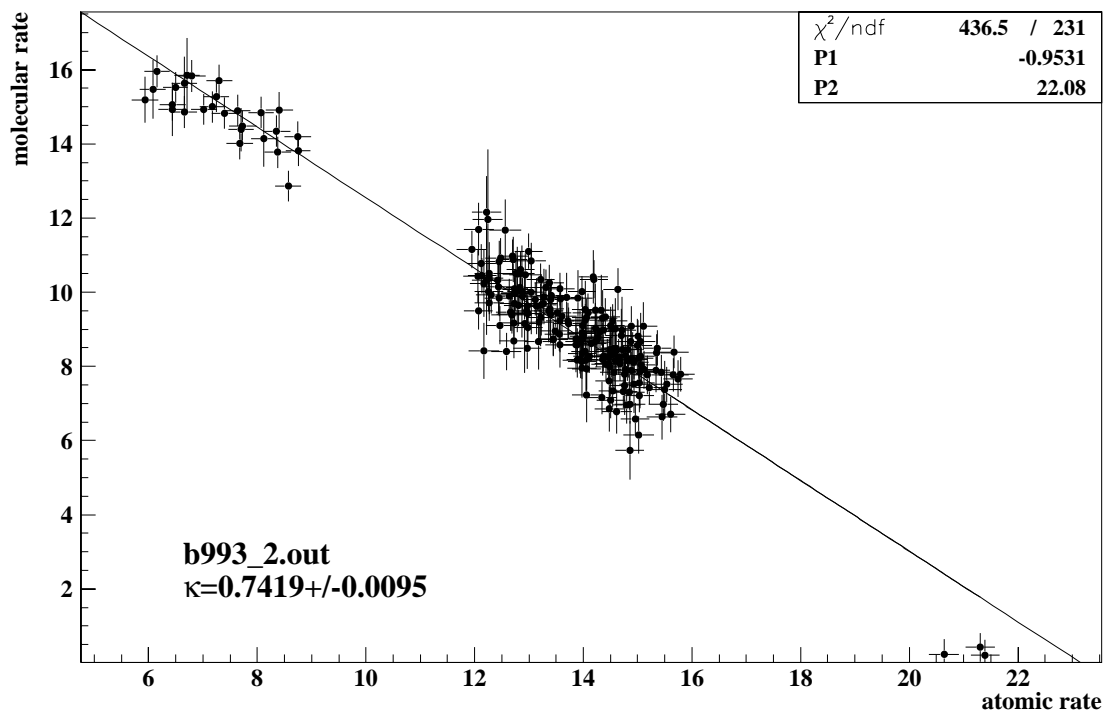


Figure A.18: Plot of the beam dump on September 10th, 1999. For the extraction of κ only the data points before the second successful injection of a new HERA positron beam ($t < 25$ hours) have been used. The spikes in the temperature result from the new injections. This beam dump burned a hole in the storage cell, changing the properties of the target. Since the cell never recovered from the damage this scan did not contribute to the mean κ .



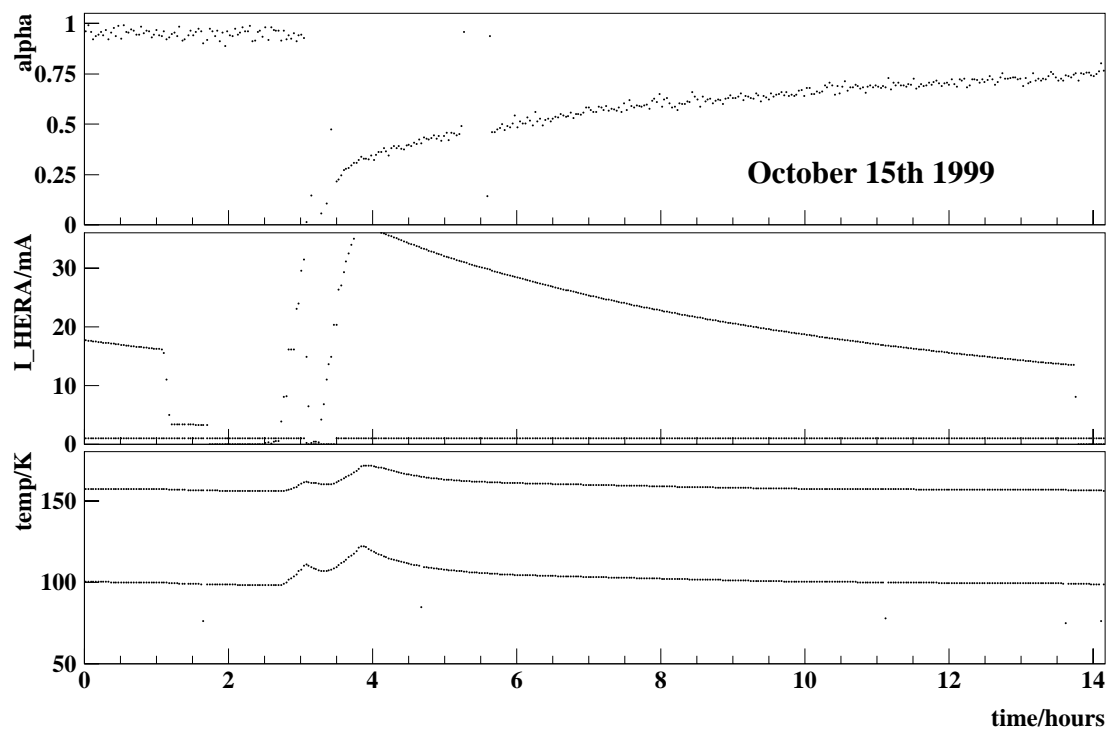
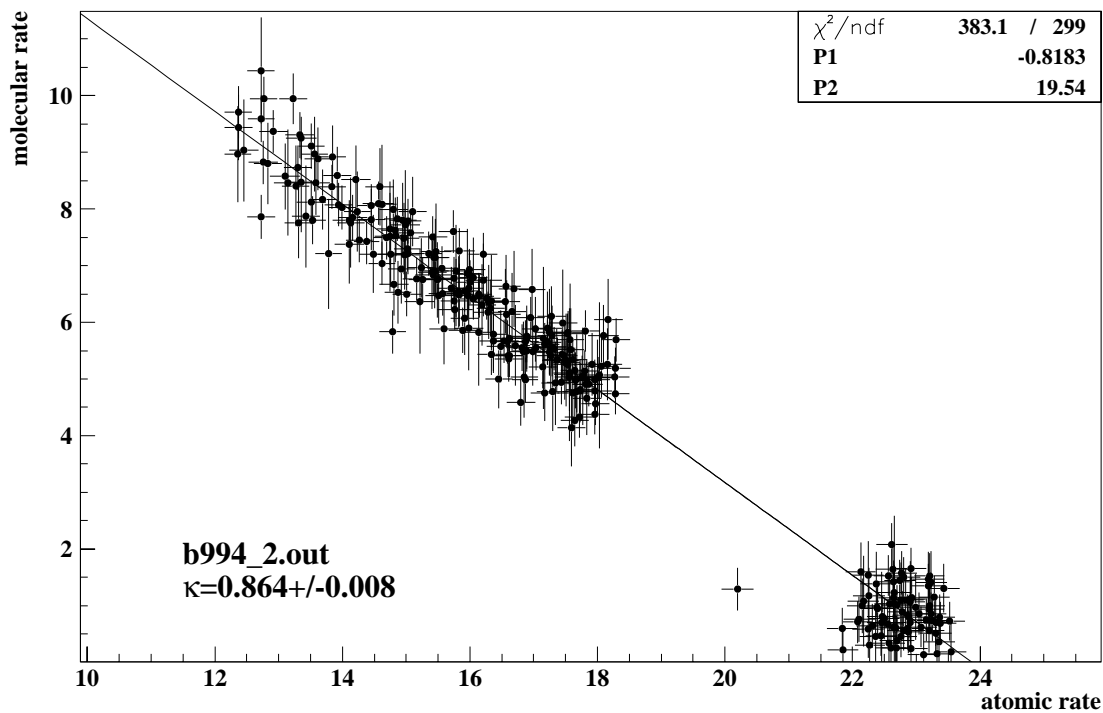


Figure A.19: Plot of the beam dump on October 15th, 1999. After the drop in α^{TGA} a new positron beam was injected causing the temperature of the cell to rise. For the extraction of kappa a few data points before the beam loss and then data from the recovery of α^{TGA} at constant cell temperature have been taken into account.



A.3 Compilation of κ Calibration Results

In this section all the results for κ extracted in the deuterium running period are summarized chronologically in the following table.

For most of the scans two different values for κ are given since the injection of two (κ_2) or three states (κ_3) has to be regarded separately. In those cases an averaged κ_{avg} is given that represents the κ value found for that particular calibration. If the field for the averaged κ_{avg} in the following table is empty for a particular scan then this scan did not contribute to the mean κ_{tot} .

The mean κ_{tot} for the deuterium running period (July 1998 until September 2000) is found to be:

$$\kappa_{tot} = 0.8606 \pm 0.0814 . \quad (\text{A.1})$$

This value is the averaged value of the various κ_{avg} with the error being half the maximum deviation of the κ_{avg} values taken into account.

The values χ^2/ndf are large since the error on the count rates is only the statistic error and does not take systematics into account, e.g. the cross talk of the magnetic fields of the Breit-Rabi polarimeter transitions with the ion-optics of the target gas analyzer. For the calibration measurements this might have an effect on the count rates of the TGA which is not averaged out since these measurements are done on short time scales.

| CALIBRATION | | VALUE | | |
|----------------|-------------------------|---------------------|---------------------|---------------------|
| typ+date | injection, notes | $\kappa_{2,3}$ | χ^2/ndf | κ_{avg} |
| TS 08. Aug '98 | 2 states, T_{ex} high | 1.0604 ± 0.0367 | 2.279/2 | |
| TS 08. Aug '98 | 3 states, T_{ex} high | 1.0445 ± 0.0238 | 3.793/2 | |
| TS 27. Aug '98 | 2 states, T_{ex} high | 0.8768 ± 0.0217 | 19.72/5 | |
| TS 27. Aug '98 | 3 states, T_{ex} high | 0.9757 ± 0.0330 | 20.37/5 | |
| BD 19. Nov '98 | 2 states | 0.8409 ± 0.0207 | 1790/59 | |
| BD 19. Nov '98 | 3 states | 0.8892 ± 0.0245 | 46.46/12 | 0.8651 ± 0.0226 |
| TS 28. Nov '98 | 2 states, T_{ex} high | 0.7841 ± 0.0178 | 28/6 | |
| TS 28. Nov '98 | 3 states, T_{ex} high | 0.8724 ± 0.0297 | 20.08/6 | |
| TS 06. Jan '99 | 2 states | 0.7988 ± 0.0037 | 445.1/4 | |
| TS 06. Jan '99 | 3 states | 0.8146 ± 0.0062 | 25.63/4 | 0.8067 ± 0.0050 |
| TS 11. Jan '99 | 2 states | 0.8167 ± 0.0074 | 64.39/5 | |
| TS 11. Jan '99 | 3 states | 0.8664 ± 0.0088 | 130.6/5 | 0.8416 ± 0.0081 |
| TS 02. Feb '99 | 2 states | 1.0014 ± 0.0395 | 43.58/2 | |
| TS 02. Feb '99 | 3 states | 0.9374 ± 0.0443 | 28.08/2 | 0.9694 ± 0.0419 |
| TS 06. Apr '99 | 2 states | 0.8608 ± 0.0479 | 23.63/4 | |
| TS 06. Apr '99 | 3 states | 0.8111 ± 0.0503 | 26.73/4 | 0.8360 ± 0.0491 |
| BD 07. Aug '99 | 2 states | 0.8475 ± 0.0286 | 66.84/58 | 0.8475 ± 0.0286 |
| TS 14. Aug '99 | 2 states, 1.part | 0.8454 ± 0.0619 | 7.473/1 | |
| TS 14. Aug '99 | 3 states, 1.part | 0.8127 ± 0.0669 | 3.623/1 | |
| TS 14. Aug '99 | 2 states, 2.part | 0.8789 ± 0.0299 | 1.28/2 | |
| TS 14. Aug '99 | 3 states, 2.part | 0.8486 ± 0.0341 | 5.562/2 | 0.8464 ± 0.0482 |
| TS 19. Aug '99 | 2 states | 0.8828 ± 0.0078 | 70.43/4 | |
| TS 19. Aug '99 | 3 states | 0.9374 ± 0.0094 | 7.325/4 | 0.9101 ± 0.0086 |
| BD 10. Sep '99 | 2 states, cell hole | 0.7419 ± 0.0095 | 436.5/231 | |
| TS 08. Oct '99 | 3 states, T_{ex} high | 1.1791 ± 0.0407 | 123.1/4 | |
| BD 15. Oct '99 | 2 states | 0.8640 ± 0.0080 | 383.1/299 | 0.8640 ± 0.0080 |
| TS 03. Nov '99 | 2 states, T_{ex} high | 0.9494 ± 0.0223 | 9.824/4 | |
| TS 03. Nov '99 | 3 states, T_{ex} high | 0.9517 ± 0.0211 | 12.96/3 | |
| TS 08. Sep '00 | 2 states, cont. | 0.8194 ± 0.0031 | 517.7/143 | 0.8194 ± 0.0031 |

Appendix B

The BRP Magnet System

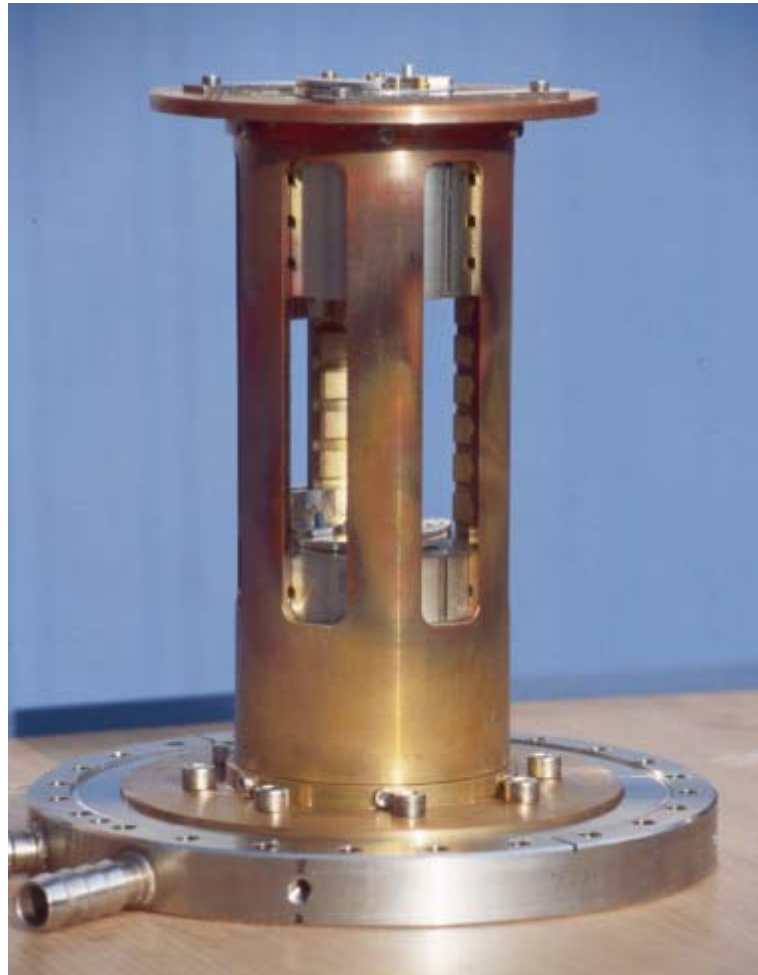


Figure B.1:
The sextupole magnet system of the Breit-Rabi polarimeter in the holding frame.

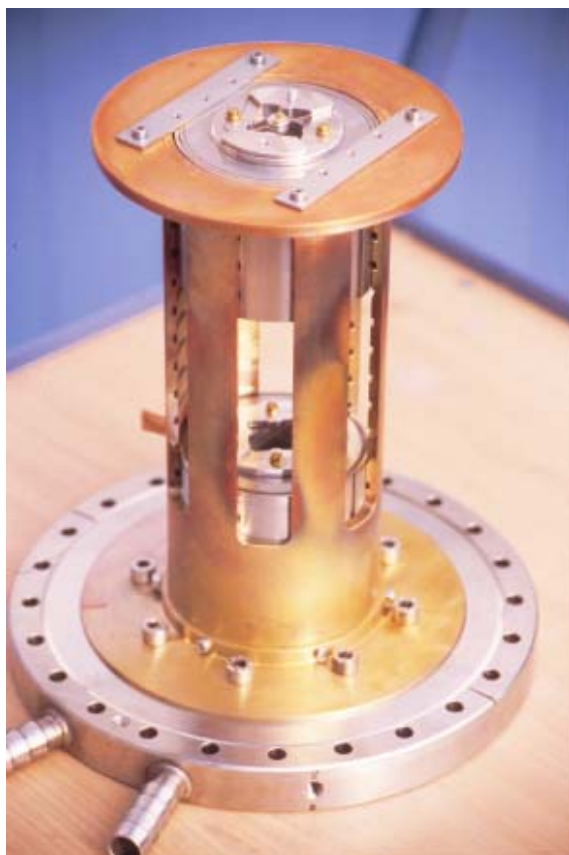


Figure B.2:

The sextupole magnets of the Breit-Rabi polarimeter in a copper holding frame. The first sextupole magnet is in the top of the holding frame, the second sextupole magnet is in the bottom part where the holding frame is connected to the flange. In the experiment this flange is screwed to the sextupole vacuum chamber of the BRP.

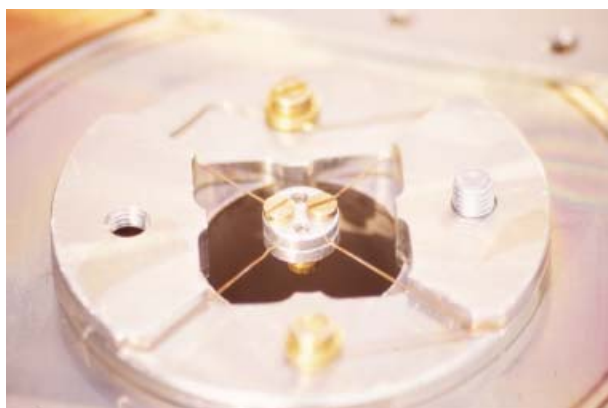


Figure B.3:

The beam blocker is a round piece of metal centered by wire in a metal holding ring which is magnetically held to the first sextupole magnet in the BRP.



Figure B.4:

The alignment cross of the BRP is a wire cross in a metal ring magnetically held to the second sextupole magnet of the BRP.

List of Figures

| | | |
|------|-----------------------------------------------------------------------------|----|
| 1 | Picture of the HERMES Target System | IV |
| 1.1 | The HERA Ring | 3 |
| 2.1 | Breit-Rabi Diagram for the Hydrogen Atom | 9 |
| 2.2 | Breit-Rabi Diagram for the Deuterium Atom | 11 |
| 3.1 | Simplified Overview of the Target System | 17 |
| 3.2 | The Atomic Beam Source Setup | 18 |
| 3.3 | The Storage Cell in the Target System | 20 |
| 3.4 | The HERMES Storage Cell in Details | 20 |
| 3.5 | The Dimensions of the Various Tubes | 22 |
| 3.6 | The Target Gas Analyzer Setup | 23 |
| 3.7 | The Quadrupole Mass Spectrometer of the Target Gas Analyzer | 24 |
| 3.8 | The Breit-Rabi Polarimeter Setup | 25 |
| 3.9 | The Breit-Rabi Polarimeter Vacuum System | 26 |
| 3.10 | Detailed Overview of the Target System | 27 |
| 4.1 | Molecular Count Rate Versus Atomic Count Rate | 31 |
| 4.2 | Nuclear Count Rates Versus Cell Temperature | 32 |
| 4.3 | Molecular Count Rate Versus Cell Temperature | 33 |
| 4.4 | Temperature Corrected Nuclear Count Rates Versus Cell Temperature | 34 |
| 4.5 | Temperature Scan on August 19th, 1999 | 35 |
| 4.6 | κ Calibration Using a Temperature Scan | 35 |
| 4.7 | Beam Dump on August 7th, 1999 | 37 |
| 4.8 | Kappa from a Beam Dump | 37 |
| 4.9 | Comparison of Two Temperature Scans | 38 |
| 4.10 | The Scan of September 8th, 2000 | 39 |
| 4.11 | κ Calibration in 2000 | 40 |
| 4.12 | Results for κ_{avg} | 41 |
| 5.1 | View Perpendicular to the Axis of a Sextupole Magnet | 44 |
| 5.2 | Sextupole Magnets as Optical Lenses | 46 |
| 5.3 | Scheme of the Various Bins Used in the Monte Carlo Simulation | 47 |

| | | |
|------|-----------------------------------------------------------------------------------------|----|
| 5.4 | Various Trajectories Through a System of Two Sextupole Magnets . . . | 49 |
| 5.5 | The Weighting of Different Trajectories | 50 |
| 5.6 | Monte Carlo Result for the Former Magnet System of the BRP | 51 |
| 5.7 | Weighted Monte Carlo Result for the Former Magnet System | 51 |
| 5.8 | Monte Carlo Result Over the Cell Temperature | 52 |
| 5.9 | Monte Carlo Results for Magnets with Smaller Pole Tip Fields | 53 |
| 5.10 | Monte Carlo Results for Shorter Magnets | 53 |
| 5.11 | Monte Carlo Results for Existing Magnets | 53 |
| 5.12 | Monte Carlo Results for Four Different Spacings of Short Magnets . . . | 53 |
| 5.13 | Weighted Monte Carlo Result for the New Magnet System | 54 |
| 5.14 | Comparison of Monte Carlo Results for Hydrogen and Deuterium . . . | 55 |
| 5.15 | Comparison of Monte Carlo Results for a Shift of 2 mm | 56 |
| 5.16 | Comparison of Monte Carlo Results for an Extended Extension Tube | 56 |
| 5.17 | Measurement at 79.2 K with the Former Magnet System | 58 |
| 5.18 | Measurement for State $ 3\rangle$ with the Former Magnet System | 58 |
| 5.19 | Measurement for State $ 1\rangle$ with the Former Magnet System | 58 |
| 5.20 | Comparison of the Measurements with the Model for the Former Magnet System | 59 |
| 5.21 | The Model for the Former Magnet System | 60 |
| 5.22 | Measurement at 80.9 K with the New Magnet System | 61 |
| 5.23 | Measurement at 48.9 K with the New Magnet System | 61 |
| 5.24 | Comparison of the Measurements with the Model for the New Magnet System | 63 |
| A.1 | Temperature Scan on August 8th, 1998 | 68 |
| A.2 | Temperature Scan on August 27th, 1998 | 69 |
| A.3 | Temperature Scan on November 28th, 1998 | 70 |
| A.4 | Temperature Scan on January 6th, 1999 | 71 |
| A.5 | Temperature Scan on January 11th, 1999 | 72 |
| A.6 | Temperature Scan on February 2nd, 1999 | 73 |
| A.7 | Temperature Scan on April 6th, 1999 | 74 |
| A.8 | Temperature Scan on August 14th, 1999 | 75 |
| A.9 | Temperature Scan on August 19th, 1999 | 76 |
| A.10 | Temperature Scan on October 8th, 1999 | 77 |
| A.11 | Temperature Scan on November 3rd, 1999 | 78 |
| A.12 | Temperature Scan on January 18th, 2000 and March 9th, 2000 | 79 |
| A.13 | Temperature Scan on March 14th, 2000 and April 17th, 2000 | 80 |
| A.14 | Temperature Scan on May 19th, 2000 and July 31st, 2000 | 81 |
| A.15 | Temperature Scan on September 8th, 2000 | 82 |
| A.16 | Beam Dump on November 19th, 1998 | 83 |
| A.17 | Beam Dump on August 7th, 1999 | 84 |

LIST OF FIGURES

95

| | |
|-----------------------------------------------------------------|----|
| A.18 Beam Dump on September 10th, 1999 | 85 |
| A.19 Beam Dump on October 15th, 1999 | 86 |
| B.1 Picture of the Sextupole Magnet System of the BRP | 89 |
| B.2 Picture of the Sextupole Magnet System | 91 |
| B.3 Picture of the Beam Blocker | 91 |
| B.4 Picture of the Alignment Cross | 91 |

Bibliography

- [Ab58] A. Abragam and J.M. Winter; Phys. Rev. Lett. **1** (1958) 374.
- [Ab78] A. Abragam; “Principles of Nuclear Magnetism”, University Press, Oxford (1978).
- [Ba96] C. Baumgarten; Diploma Thesis, Universität Hamburg (1996).
- [Ba00] C. Baumgarten; Ph.D. Thesis, LM Universität München (2000).
- [Br95] B. Braun; Ph.D. Thesis, LM Universität München (1995).
- [Br97] B. Braun; AIP Conf. Proc. **421**, R. Holt, M. Miller (eds.), Urbana-Champaign (1997) 156.
- [Bre31] G. Breit, I.I. Rabi; Phys. Rev. **38** (1931) 2082.
- [Co99] C. Cohen-Tannoudji, B. Diu, F. Laloë; “Quantum Mechanics, Vol.I”, 2nd edition, Walter de Gruyter, Berlin (1999).
- [Du95] M. Düren; Habil. Thesis, HERMES internal report **95-02** (1995).
- [Dy92] A. Dymanus; “Atomic and Molecular Beam Methods”, Vol. II, G. Scoles, D. Laine, U. Valbusa (eds.), Oxford University Press (1992).
- [E88] J. Ashman et al.; Phys. Lett. **B 206** (1988) 364.
- [Ga91] H. G. Gaul; Ph.D. Thesis, Universität Heidelberg (1991).
- [Ga92] H. G. Gaul und E. Steffens; Nucl. Instr. Meth. **A 316** (1992) 297.
- [Gab95] E.-M. Gabriel; Diploma Thesis, Universität Heidelberg (1995).
- [Gr98] C. Großhauser; Ph.D. Thesis, FA Universität Erlangen-Nürnberg (1998).
- [Hal80] K. Halbach; Nucl. Instr. Meth. **169** (1980) 1.
- [Hae67] W. Haeberli; Ann. Rev. Nucl. Sci. **17** (1967) 373.

- [Hae99] W. Haeberli; Proc. Pol. Sources and Targets **PST 99**, A. Gute, S. Lorez, E. Steffens (eds.), Erlangen (1999) 4.
- [He90] HERMES Collaboration; HERMES Proposal **PRC-90/91** (1990).
- [He93] HERMES Collaboration; HERMES Technical Design Report **PRC 93/06** (1993).
- [He98a] HERMES Collaboration; Phys. Lett. **B 442** (1998) 484.
- [He98b] HERMES Collaboration; Nucl. Instr. Meth. **A 417** (1998) 230.
- [He99a] HERMES Collaboration; Phys. Rev. Lett. **82** (1999) 1164.
- [He99b] HERMES Collaboration; Phys. Lett. **B 464** (1999) 123.
- [Hen98] M. Henoch; Diploma Thesis, Universität Münster (1998).
- [Hen00] M. Henoch; AIP Conf. Proc. **549** (2000) 666.
- [Kol95] H. Kolster et al.; Proc. Pol. Beams and Pol. Gas Targets, H. Paetz, L. Sydov (eds.), Cologne (1995) 265.
- [Kol98] H. Kolster; Ph.D. Thesis, LM Universität München, (1998).
- [Koc99a] N. Koch, E. Steffens; Rev. Scient. Instr., **70(3)**, 1631 (2000).
- [Koc99b] N. Koch et al.; Proc. Pol. Sources and Targets **PST 99**, A. Gute, S. Lorez, E. Steffens (eds.), Erlangen (1999) 164.
- [Koc99c] N. Koch; Ph.D. Thesis, FA Universität Erlangen-Nürnberg (1999).
- [Le01] P. Lenisa et al.; Draft of HERMES internal report (2001).
- [Li93] M.-T. Lin; Diploma Thesis, Universität Heidelberg (1993).
- [Lo99] S. Lorenz; Diploma Thesis, FA Universität Erlangen-Nürnberg (1999).
- [Ma92] T. Mayer-Kuckuk; "Kernphysik", 5. überarbeitete u. ergänzte Auflage, Teubner, Stuttgart (1992).
- [Ma94] T. Mayer-Kuckuk; "Atomphysik", 4. durchgesehene u. erweiterte Auflage, Teubner, Stuttgart (1994).
- [Pr93] J.S. Price, W. Haeberli; Nucl. Instr. Meth. **A 326** (1993) 416.
- [Re94] K. Reinmüller; Diploma Thesis, LM Universität München (1994).

- [Sc91] P. Schiemenz, A. Ross and G. Graw; Nucl. Instr. Meth. **A 305** (1991) 15.
- [Si94] I. Simiantonakis; Diploma Thesis, Universität Heidelberg (1994).
- [SG21] W. Gerlach und O. Stern; Z. Physik **8** (1921) 110.
- [SL93] P. L. Anthony et al.; Phys. Rev. Lett. **71** (1993) 959.
- [SL95] K. Abe et al.; Phys. Rev. Lett. **74** (1995) 346.
- [SL97] K. Abe et al.; Phys. Rev. Lett. **79** (1997) 26.
- [SM94] B. Adeva et al.; Phys. Lett. **B 320** (1994) 400.
- [SM97] D. Adams et al.; Phys. Lett. **B 396** (1997) 338.
- [So64] A. A. Sokolov und I. M. Ternov; Sov. Phys. Dokl. **8** (1964) 1203.
- [St92] F. Stock; Diploma Thesis, Universität Heidelberg (1992).
- [St94a] F. Stock; Ph.D. Thesis, Universität Heidelberg (1994).
- [St94b] F. Stock; Nucl. Instr. Meth. **A 342** (1994) 334.
- [St95] F. Stock et al.; Proc. Pol. Beams and Pol. Gas Targets, H. Paetz, L. Sydov (eds.), Cologne (1995) 260.
- [Ste00] E. Steffens; *Talk at HERMES Collab. Meeting in Gent* (2000).
- [Stn95] J. Stenger, K. Rith; Nucl. Instr. Meth. **A 361** (1995) 60.
- [Stw95a] J. Stewart et al.; Proc. Pol. Beams and Pol. Gas Targets, H. Paetz, L. Sydov (eds.), Cologne (1995) 408.
- [Stw95b] J. Stewart et al.; HERMES internal report **95-002** (1995).
- [Tr96] S. Trieb; Thesis, Universität Heidelberg (1996).
- [Va00] A. Vassiliev et al.; Rev. Scient. Instr., **71**, 3331 (2000).
- [Wa98] A. Wachter, H. Hoerber; "Repetitorium Theoretische Physik", Springer, Berlin (1994).

Acknowledgements

Mein besonderer Dank gilt Herrn Prof. Dr. E. Steffens für die Ermöglichung und Betreuung dieser Arbeit am DESY in Hamburg.

Allen Mitgliedern des HERMES Experiments danke ich für die freundliche Aufnahme in der HERMES Kollaboration und den gemeinsamen Spaß nicht nur beim Mittagstisch. M. Raithel danke ich für das nette Zusammenwohnen und seine Hilfe bei diversen Problemen. Außerdem danke ich der gesamten Offsite-Gruppe, insbesondere M.-A. Funk, P. Oelwein und F. Meissner, für die kontinuierliche, abendliche Erkundung der Großstadt Hamburg.

Bedanken möchte ich mich auch bei M. Henoch, N. Koch und C. Baumgarten für die Betreuung und Unterstützung beim Schreiben dieser Arbeit, sowie bei H. Kolster für die außergewöhnlich angenehme Zusammenarbeit. Weiterhin danke ich C. Simani, H. Kolster und C. Baumgarten für die Unterstützung bei der Kalibration des TGAs, sowie C. Baumgarten für die Monte-Carlo Simulation. An dieser Stelle möchte ich allen Mitgliedern der Targetgruppe des HERMES Experiments für die vielen Anregungen und Diskussionen, sowie für das ausgezeichnete Arbeitsklima danken.

Außerdem danke ich der Gruppe PI2 der Universität Erlangen-Nürnberg für die Unterstützung und Betreuung in den letzten Wochen vor der Abgabe dieser Arbeit.

H. Seitz, H. Gumbert, A. Lese und T. Puttke danke ich stellvertretend für viele weitere für die Unterstützung und Freundschaft während des Studiums. Besonders möchte ich mich bei meinen Eltern bedanken, welche mir dieses Physikstudium überhaupt ermöglicht haben.

Und vor allem danke ich Thomas für seine Unterstützung, sein Verständnis und seine Gabe mich zu erheitern und zu motivieren.

Hiermit erkläre ich, daß ich diese Arbeit selbstständig verfaßt und keine anderen als die angegebenen Quellen als Hilfsmittel benutzt habe.

Erlangen, den 02. April 2001

Ines Brunn